Microscopic studies of interlayer magnetic coupling across nonmagnetic and antiferromagnetic spacer layers

Dissertation

zur Erlangung des akademischen Grades

doctor rerum naturalium (Dr. rer. nat.)

vorgelegt der

Mathematisch-Naturwissenschaftlich-Technischen Fakultät
(mathematisch-naturwissenschaftlicher Bereich)
der Martin-Luther-Universität Halle-Wittenberg

von Herrn **Liviu Ionut Chelaru**

geb. am: 15. Mai 1974 in Iasi, Rümanien

Gutachterin/Gutachter:

1. Prof. Dr. J. Kirschner

2. Prof. Dr. W. Hergert

3. Prof. Dr. A. Schreyer

Halle/Saale, 16.12.2003

Contents

Introduction

The discovery made in single-crystalline Fe/Cr/Fe(001) trilayers of an antiparallel alignment of the magnetization of the Fe layers, in zero field, for a certain thickness of the Cr layer brought to the forefront the study of magnetic coupling phenomena [1, 2, 3]. Extensive research on the magnetic coupling across nonmagnetic and antiferromagnetic layers revealed an oscillatory behavior (a periodic change of the relative orientation of the magnetization direction of the ferromagnetic layers) as a function of spacer thickness [4].

The discovery of GMR (Giant Magneto-Resistance) in metal multilayers opened the way for multiple technological applications of magnetic structures [5, 6]. The resistance of such multilayers depends upon the magnetic arrangement of the ferromagnetic layers and was observed to be higher when the moments are aligned antiparallel to each other. The much larger response measured in the layered structures than that of the intrinsic magnetoresistance of the ferromagnetic layers themselves is the reason why the new effect was dubbed giant magnetoresistance (GMR). Driven by technological applications, the study of magnetic interlayer coupling become more than academic and fundamental research. Today GMR multilayered structures have already found their wide variety of applications in the family of disk drive products.

The magnetic interlayer coupling in Fe/Cr/Fe trilayers was shown to be strongly dependent on the interface roughness [7, 8]. For room temperature growth, with rougher interfaces, the interlayer coupling oscillates with a period of several monolayers Cr thickness. Growth at elevated temperature lead to smooth and very flat terraces. In this case the direction of magnetization of the top ferromagnetic layer changes with each additional Cr monolayer. The absence of the short period coupling in samples with a higher roughness has been understood within the averaging effect of coupling. Presence of the steps at the interfaces leads to magnetic frustration [9, 10]. One consequence of such frustration is a non-collinear coupling as has been observed in different epitaxial systems [11, 12]. The explanation has been given in a model where the coupling angle (angle between magnetization directions) is highly sensitive to the interface properties [13, 14]. However, the dependence of the short period coupling on the interface roughness has never been examined separately. Does the phase and strength of short period coupling depend on the interface roughness? Can we trigger these parameters by tuning the interface roughness?

The use of epitaxial single crystalline layers provides the opportunity to study this coupling at well-defined interfaces. Because of the low lattice mismatch, antiferromagnetic $Fe_{50}Mn_{50}$ films grown in an epitaxial layer-by-layer growth mode on a Cu(001) single crystal are ideal candidates for such investigations.

Strong efforts are currently being made to study antiferromagnetic films (AFM) adjacent to ferromagnetic (FM) ones [15, 16]. This arrangement gives rise to a wide variety of complex magnetic structures, e.g., spin density waves, frustrated spin-structures, which determine the magnetic structure at the surfaces of thin films [17, 18, 19]. An AFM layer in contact with an FM was shown to acquire an induced magnetic moment at the interface [20].

Besides the oscillatory magnetic interlayer coupling also micromagnetic mechanisms can lead to a coupling between magnetic layers across nonmagnetic spacer layers in thin film multilayered structures. They are related to the microscopic properties, such as structure or morphology, but also to the purely magnetic microstructure, i.e., the magnetic domain structure. When the lateral dimensions of the systems are sufficiently small, magnetostatic coupling can arise due to the fringing fields at the edge of the sample [21]. Rather than oscillatory, an increase of the ferromagnetic interlayer coupling across nonmagnetic spacer layer, with a decrease of spacer thickness has been observed. This additional ferromagnetic coupling has been shown to be magnetostatic in origin, caused by free poles at the magnetic layers due to the correlated interface roughness [22]. Only recently it has been considered that also the magnetostatic stray fields from domain walls of each magnetic layer could mediate the coupling across a nonmagnetic spacer layer in multilayered structures [23, 24].

Photoelectron emission microscopy (PEEM) combined with X-ray magnetic circular dichroism (XMCD) is an ideally suited technique for these studies. It relies on the fact that the X-ray absorption at an elemental absorption maxima depends on the relative orientation of the helicity vector of the circularly polarized incoming X-rays and the magnetization direction of the sample. In PEEM the secondary emitted electrons at the sample surface are used to create the magnified image of the sample, which are proportional to the local absorption and thus to the projection of the local magnetization direction onto the light incidence. This allows a microscopic imaging of the domain configuration of each layer.

The organization of the thesis is as follows. An overview of the background of conventional models describing magnetic interlayer coupling with some insight into the underlying physics is given in the Chapter 1. In Chapter 2 the experimental characterization techniques used in this work are outlined together with some aspects of the sample preparation. In Chapter 3 are grouped the experimental results on the interlayer magnetic coupling across $Fe_{50}Mn_{50}$ as an AFM spacer layer. Knowledge of the sample interfaces is gained from the epitaxial growth and surface morphology study of $Fe_{50}Mn_{50}$ on Cu(001). The magnetic coupling phenomena were studied for $Fe_{50}Mn_{50}$ layers sandwiched between two ferromagnetic layers with an in-plane or an out-of-plane magnetization direction. In the last two sections of Chapter 3, attention is

being paid to the modifications of the coupling across $Fe_{50}Mn_{50}$, when deposited on layers with different magnetization direction. Chapter 4 focuses on the magnetostatic coupling mediated by stray fields of domain walls. The main results of the work presented in this thesis are discussed in Chapter 5. Finally, a summary and conclusions of the findings presented in this thesis will be given.

Chapter 1

Magnetic interlayer coupling

The basic mechanisms of interlayer exchange coupling between two ferromagnetic layers separated either by a non–magnetic or antiferromagnetic spacer layer are addressed in this introductory chapter.

The oscillatory coupling was observed as a general property of almost all transition-metal magnetic multilayered systems in which the nonferromagnetic layer comprises of one of the $3d$, $4d$, or $5d$ transition metals or one of the noble metals. In addition to measurements of the coupling [1, 4, 25], there had been measurements of magnetic multilayers using photoemission [27, 28]. Strong peaks in intensity were identified as arising from quantum well states (QWS) (discrete electronic states form when electrons are confined in space by a potential). The periodicity in thickness at which these states crossed the Fermi level established the connection between the QWS and the interlayer exchange coupling. With the QWS picture, as outlined in Sec. 1.1, the dependence of the interlayer coupling on the spacer layer thickness can then be understood as a result of a quantum interference effect. The critical spanning vectors of the Fermi surface of the spacer material determine the oscillation periods of the interlayer coupling.

Magnetic multilayers containing an antiferromagnet as a mediating spacer layer have to be distinguished from other, paramagnetic or nonmagnetic, spacer layers. The interlayer coupling of such systems cannot be understood without taking the magnetic state of the antiferromagnetic spacer layer and the proximity effects at the interfaces into account. The proximity magnetism model and frustration of magnetic coupling across antiferromagnetic spacer layers induced by thickness fluctuations are the subjects of Sec. 1.2.

As the size of the system is reduced, the "magnetic poles" generated at the surfaces influence the interactions within the layer and between the two ferromagnetic layers. The stray field associated with it increases rather rapidly with decreasing spacer layer thickness, so that for very thin films, other types of domain walls occur. The transition regions where the magnetization changes direction from one domain to the other are called domain walls. For two ferromagnetic layers separated by a thin nonmagnetic layer, the stray-field of a domain wall in one layer will

exert a local force in the region above the domain wall in the second layer giving rise to another local type of coupling. Such local magnetostatic interactions are reviewed in the last section, Sec. 1.3, of this chapter.

1.1   Quantum well states as a mediator of magnetic coupling

The discovery of oscillatory interlayer exchange coupling between two ferromagnetic layers depending on thickness of the nonmagnetic spacer layer has promted a wealth of investigations in this field [2, 3]. Long range magnetic exchange coupling between transition metals has been observed for the first time in Fe/Cr/Fe(001), which exhibited an antiferromagnetic coupling of the Fe films across the Cr spacer layers, for a certain Cr thickness [1]. Subsequent studies have revealed the oscillatory behavior of the exchange coupling in this system and its general occurrence in a wide variety of systems [4, 25]. Later on, it has been found that other magnetic properties such as giant magnetoresistance [5], magneto-optical response [6], and magnetic anisotropy [26] also exhibit oscillatory behavior as a function of spacer layer thickness. Apart from morphology–induced oscillations, the occurrence of quantum size effects in the layered system is believed to be the origin of the oscillations. The resulting quantum well states are electronic states confined within ultrathin films by the potential barriers at the surface or at the interface to the adjacent layers, giving rise to sharp structures in the electronic density of states. Experimentally, these QWS states have indeed been observed in various systems [27, 28].

Phenomenologically, the interlayer coupling energy per unit area can be expressed as:

$$E = -J_1 cos\theta - J_2 cos^2\theta \tag{1.1}$$

where θ is the angle between the magnetizations of the two magnetic layers and the parameters J_1 and J_2 determine the strength and the type of the coupling [29]. If the term with J_1 dominates, then it follows from minimization of equation 1.1 that the coupling is ferromagnetic (FM) (antiferromagnetic (AFM)) for positive (negative) J_1, respectively. An FM coupling favors a parallel alignment while an AFM coupling favors antiparallel alignment of the magnetization directions of the ferromagnetic layers. In the same way if the term with J_2 dominates and is negative, we obtain 90°-coupling, corresponding to perpendicular orientation of the two magnetizations of the ferromagnetic layers. The first coupling type corresponding to the first term on the right hand side of equation 1.1 is called "bilinear" coupling and the second "biquadratic" coupling. The basic mechanism of bilinear coupling, across metallic, diamagnetic and paramagnetic interlayers is now thought to be an indirect interaction of the magnetic moments mediated by the itinerant electrons of the interlayer.

The various interactions giving rise to an interlayer magnetic coupling are: the dipolar magnetostatic interaction, and the indirect exchange interaction of the Rudermann–Kittel–Kasuya–Yosida (RKKY) type. For a homogeneously magnetized layer of infinite extension, there

is no dipolar stray field, so that dipolar interlayer coupling can arise only as a result of departures from this idealized situation. The indirect exchange interaction is mediated by itinerant electrons which are scattered successively by the magnetic layers [31].

Independently, an apparently different mechanism was proposed by Edwards [30] and by other authors [32, 33]. In this approach the coupling is ascribed to the change of density of states resulting from the spin-dependent confinement of the electrons (or holes) in the quantum well provided by the spacer layer. This approach yielded exactly the same oscillatory behavior and decay as the RKKY interaction.

Bruno [34, 35] has shown that the different approaches indeed correspond to different approximations of the same mechanism. The amplitude and phase of the oscillatory coupling are expressed in terms of the amplitude and phase of reflection coefficients for the electrons at the interfaces between the spacer and the magnetic layers. The basic assumption within the quantum well states (QWS) approach, in order to explain oscillatory coupling, is spin dependent confinement of electrons in the interlayer, when the magnetic films are aligned parallel.

(a)   (b)
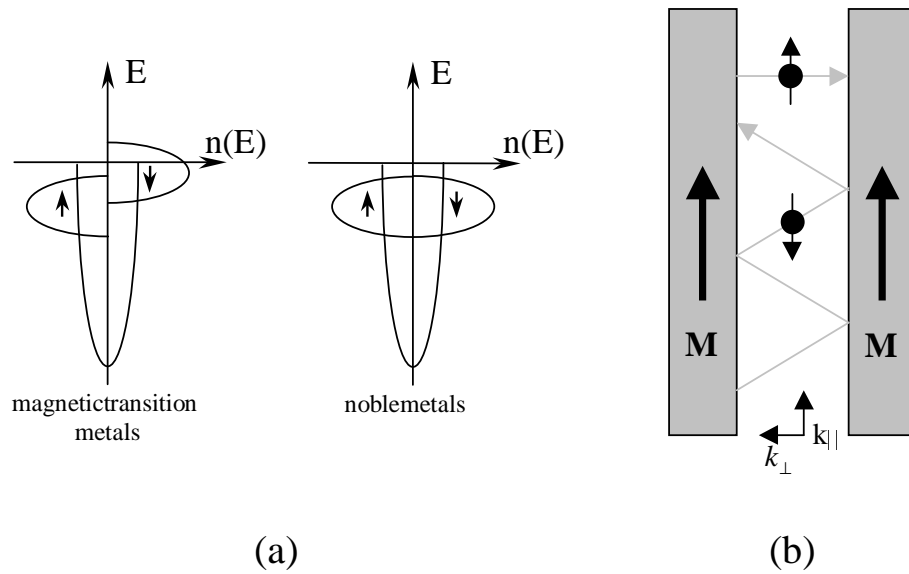
Figure 1.1: (a) Schematic density of states of magnetic $3d$ metals and of noble metals; (b) spin down electron ($\downarrow$) reflected back and forth between the interfaces, spin up electron ($\uparrow$) can penetrates the whole stack with little reflection at the interfaces.

The origin of such a behavior is shown in Fig. 1.1 (a) where schematic band structures for the magnetic $3d$ transition metals and noble metals are drawn as examples. Spin up ($\uparrow$) electrons can penetrate the whole stack with little reflection at the interfaces. For spin down ($\downarrow$) electrons, due to the splitting of the bands in the magnetic films, the transmission of electrons is reduced leading to stronger confinement. With respect to the motion of the electrons perpendicular to

the interfaces a spectrum of discrete energy levels is obtained corresponding to the formation of standing electron waves. The situation is illustrated in Fig. 1.1 (b). Electrons in the interlayer with their spins opposite to the magnetization $\overrightarrow{M}$ are strongly reflected at the interfaces which leads to their confinement. Such a standing wave is the result of the superposition of the two propagating waves with wave vector components $\pm k_\parallel$ and $\pm k_\perp$ as shown in Fig. 1.1 (b). For a standing wave to form we must have $2K_\perp = \frac{n2\pi}{D}$ (n is a integer number and D interlayer thickness). When the interlayer thickness is increased, the discrete levels shift downwards and new levels come in and are populated upon crossing the Fermi energy E_F. The result is an increase of the electronic energy when such a level just crosses E_F. To low its energy the system changes the magnetization direction from parallel to antiparallel alignment. For discrete levels far below E_F, with low energy, a parallel alignment of magnetization directions will be more favorable. Therefore, upon increasing the spacer thickness, an oscillatory magnetic coupling is expected. The stronger the confinement and the higher the changes in the density of states, the larger will be the associated coupling amplitudes. A decrease of the electronic energy stabilizes the parallel alignment and an increase when a QWS crosses the Fermi level, leads to its destabilization and therefore to antiparallel alignment of magnetization. Hence, the interlayer coupling oscillates as a function of the interlayer thickness D. For an antiferromagnetic alignment of the magnetic films, both spins up and down are less confined and no standing waves are formed.

Taking into account the real band structure of all three layers, the exchange coupling between ferromagnetic layers separated by nonmagnetic spacer layers is a product of the electronic and geometrical properties of the Fermi surface of the spacer layer material and the reflection amplitudes from the interfaces [36]. Assuming two contributions to the oscillatory coupling, since the Fermi surface has two different stationary spanning vectors, J_1 can be written:

$$J_1(n) = J_s(n) + J_L(n) = \frac{1}{D^2}A_s sin(\frac{2\pi nd}{\Lambda_s} + \Phi_s) + \frac{1}{D^2}A_L sin(\frac{2\pi nd}{\Lambda_L} + \Phi_L) \qquad (1.2)$$

where Λ_s and Λ_L are the short and long periods of oscillation, D is the thickness of the nonmagnetic interlayer, Φ_s and Φ_L are the phases and the amplitudes A_s and A_L include all the Fermi surface geometry and interface reflection probabilities. According to eq. 1.2 the amplitudes of oscillatory coupling are expected to decay proportional to D^{-1}. Bruno and Chappert [37] have shown that the attenuation changes from a D^{-2} behavior in the absence of nesting to a $D^{-3/2}$ dependence in the case of partial and to a D^{-1} dependence for complete nesting.

The quantum well states model only applies to paramagnetic or diamagnetic interlayers. In the case of antiferromagnetic spacer layer QWS can no longer be used to describe the two layer short period coupling, because in this case the antiferromagnetic order of the spacer layer dominates the coupling. This will be discussed in the next section.

1.2   Coupling across antiferromagnetic layers and the role of interface roughness

The magnetic coupling across paramagnetic and diamagnetic metal spacer layers is well described by the quantum well model which the coupling is determined by the Fermi surface properties of the spacer layer and by the reflection amplitudes for electrons scattering at the interfaces between the spacer layer and the ferromagnetic layer. In contrast, if the spacer layer is an antiferromagnetically ordered material such as Cr or Mn, it can no longer be considered a "passive" medium transmitting the indirect exchange coupling as in the quantum well picture. In such cases, the exchange coupling of the antiferromagnet to the ferromagnet at the interfaces, as well as the internal exchange coupling within the antiferromagnet, must be considered. The crucial difference between an antiferromagnet and a noble metal as a spacer layer is that for an antiferromagnetic material each atom has a magnetic moment which is exchange coupled to other AFM atoms and across the interface to the ferromagnet. The difficulty in understanding the FM/AFM systems comes from the fact that competition between the intralayer magnetic interaction and the FM/AFM interfacial interaction could lead to magnetic frustration, where not all the nearest-neighbor spins can be in their local minimum energy configuration.

Let us first focus on the exchange coupling in FM/AFM bilayer systems. The spin configuration in the FM and AFM layers is affected by the interface roughness. This is schematically explained in Fig. 1.2 for the example of a simple layerwise AFM spin structure. For perfect interfaces, there are spin configurations, as in Fig. 1.2 (a), in which all pairs of spins have their preferred alignment. That means, the spins in the AFM layer change direction with each additional layer while the spins in the FM layer are pointing along the same direction. In the presence of thickness fluctuations, there is a competition between the exchange coupling through regions that are an odd or even number of ML thick. In Fig. 1.2 (b) the FM–AFM interactions are frustrated in the AFM film at the position of the steps at the interface. In Fig. 1.2 (c–d) the frustration of the AFM–FM interaction is taken up in the FM layer. The energy minimization that determines where the frustration occurs will depend on the relative sizes of several length scales, as the thickness of the FM and AFM layers and the vertical and lateral extent of the interfacial defects. It will also depend on the strength of the interactions and on the temperature since the interactions are temperature dependent. Typically the bulk Néel temperature of an AFM is much lower than the FM Curie temperature. Roughly speaking, this suggests that the exchange interaction in the FM is much stronger than in the AFM. Hence, in general it will cost less energy for the interface frustration region of Fig. 1.2 (b) to be in the AFM than in the FM. The frustration will here be taken up in domain walls perpendicular to the interface, allowing the AFM moments to twist, as shown in Fig. 1.2 (b). As an alternative to being taken up in domain walls perpendicular to the interface, the frustration could be taken up in domain walls parallel to the interface, as shown in Fig. 1.2 (c). The domain walls parallel to the interface in

the AFM like in Fig. 1.2 (c) essentially decouple AFM moments from the FM moments [38, 39]. The resulting coupling between FM layers in an FM/AFM/FM trilayer in that case would be small. Evidence of this step-induced magnetic frustration was found in the Fe/Cr(001) system were the uncompensated Cr(001) surface can be partially compensated by the presence of the random steps [9, 10].
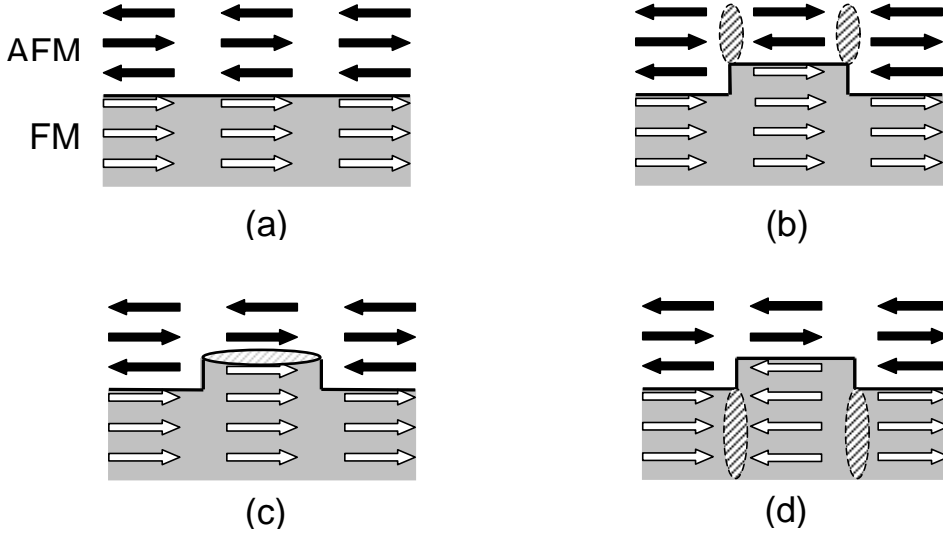
Figure 1.2: Relieving spin frustration at an FM/AFM interface: (a) perfect interface, no frustration; (b) frustration caused by a step is relieved by walls in the AFM; (c) frustration relieved at the interface; (d) frustration relieved by walls in the FM.

The interlayer coupling between two FM layers across an ideal AFM spacer layer (in the absence of the interface roughness) tends to produce either parallel (ferromagnetic) or antiparallel (antiferromagnetic) coupling. However, when roughness is present at the interface, not all the spins will be in their preferred alignment in the antiferromagnet, in the ferromagnet, and also across the interface. Some pairs of spins will necessarily not be in their minimum energy configuration, that is, the coupling between spins will be "frustrated" [7, 8]. In realistic spacer layers, the thickness fluctuations will act within a region defined by the lateral response length ℓ of the magnetic layer to average the coupling contributions from lateral regions of different thickness. When the average bilinear coupling J_1 becomes small enough, as a result of spacer layer thickness fluctuations, the multilayer finds its minimum energy state when the magnetic moments of the magnetic layers turn into a direction perpendicular to each other. This is the basis of the model proposed by Slonczewski [13] that takes into account the fluctuations $\Delta J_1(n)$ in the bilinear coupling as the coupling $J_1(n)$ changes sign from one discrete layer thickness to the next. If the overlayer thickness of a ferromagnetic layer t_{FM} is small compared to the characteristic length scale L of the terraces producing the thickness fluctuations, the leading

contribution to the biquadratic term in this model is:

$$J_2 \cong -\frac{(\Delta J_1)^2 L^2}{A_{ex} t_{FM}} \tag{1.3}$$

where the A_{ex} is the intralayer exchange coupling which hinders magnetization fluctuation in the magnetic layer, as they would be dictated by fluctuations in the bilinear coupling over a lateral response length ℓ. The model is invalid when $L > \ell$. It follows that in the limit of $L \to 0$ the contribution to the biquadratic exchange coupling disappears. Structures exhibiting fast spatial variations lead to an average torque which in our case translates into a decrease of bilinear coupling. More perfect interfaces exhibit a smaller ferromagnetic restoring torque and that results in a larger biquadratic coupling.

Slonczewski has later proposed another phenomenological model specifically for coupling across an antiferromagnetic spacer layer [14]. This model, known as the proximity or torsion model, depends on the intrinsic antiferromagnetism of the spacer and strong coupling across the interface to the ferromagnetic layers. The behavior of the antiferromagnetic spacer depends on the proximity of the ferromagnetic layer.

The coupling energy per unit area in the proximity model is given by:

$$E_c = J_{odd}\theta^2 + J_{even}(\theta - \pi)^2 \tag{1.4}$$

where θ is the angle between the magnetization directions $\overrightarrow{m_1}$ and $\overrightarrow{m_2}$ of the ferromagnetic layers, $-\pi < \theta < \pi$. The coefficients J_{odd} and J_{even} reflect the contributions of regions of the spacer layer that are, respectively, an odd or an even number of atomic monolayers (ML) thick. These coefficients are proportional to the fractional areas of the two regions and the energy to twist the magnetization in the antiferromagnet as is explained below [11]. For an odd or even number of AFM layers, the minimum energy state has the FM layers coupled with magnetization directions parallel or antiparallel, respectively. If there are thickness fluctuations so that both regions with odd and even AFM thickness are present, the energy is minimized by the AFM moments in the region with an odd numbers of layers winding up like a torsion spring with one sense, and regions with an even number of layers with the opposite sense, to reach the same average direction of the top FM layer. The general case of AFM thickness fluctuations in this model leads to a noncollinear coupling, the magnetizations remain at a finite (not 0 or π) angle for all applied fields, giving magnetization curves with a gradual approach to saturation. The proximity model assumes a strong coupling across the interface in between the antiferromagnet and the ferromagnet and also a uniform magnetization of the FM layers. With these assumptions, the frustration of the spin alignment will be relieved by a rearrangement of spins in the antiferromagnet [17, 18, 19]. The proximity model considers how the spins in the antiferromagnet adjust to minimize the energy within a region of lateral dimensions given by the response length of the ferromagnet to achieve a coupling angle θ between the magnetization

directions of the ferromagnetic layers. By minimizing the total coupling energy, E_c, one obtains the coupling angle between the magnetization directions $\overrightarrow{m_1}$ and $\overrightarrow{m_2}$ of the ferromagnetic layers. It can be expressed as:

$$\theta = \pi \frac{J_{even}}{J_{odd} + J_{even}} \tag{1.5}$$

From eq. 1.5 it can be seen that the spatial distribution of the thickness fluctuations, that is, the relative areas corresponding to an even or odd number of ML in the spacer within a lateral region given by the magnetic response length of the ferromagnetic layers, is crucial for the determination of the coupling angle.

1.3 Magnetostatic coupling

In this section coupling effects the origin of which is magnetostatic interaction are addressed. In the case of magnetic films with finite lateral extension the generation of "magnetic poles" near its ends gives rise to a magnetic field called demagnetizing field. The strength of this field depends on the geometry and magnetization of the FM layer. The simplest form of magnetostatic interaction between two ferromagnetic films is stray field coupling. It arises because each ferromagnetic layer is placed in the magnetostatic stray field of the other. The two films will have a tendency to orient their magnetizations antiparallel in order to produce a flux closure. The result of this is to decrease the Zeeman energy. In contrast to the indirect interlayer coupling, the magnetostatic coupling is highly nonuniform over the area of the interface. While it is approximately uniform within the central region, it diverges near the edges of the sample. For devices of submicron lateral dimensions, the stray fields at the edges of the devices could induce significant coupling [21].

It is possible for multilayer structures to exhibit "positive", i.e., parallel, magnetostatic coupling. For most materials evaporated as thin films, the surface of the layer is not completely flat. The layer may have a topography which has been described as that of an orange peel. This leads to the prediction of what is known "orange–peel" (Néel) coupling [22]. If the interfaces of two neighboring ferromagnetic layers have correlated roughness, dipoles are set up at the homologous protrusions and bumps at the interfaces, as shown schematically in Fig. 1.3. The magnetostatic interactions between the dipoles favor parallel alignment of the respective magnetizations of the two FM layers. In the case of multilayers, these exposed poles can act to reduce the strength of the RKKY-like or electronic AFM coupling (cf. Sec.1.1). The coupling energy due to the "orange–peel" effect, in the limit of rigid in-plane magnetization in the two layers, is given by [40]:

$$E_{OP} = -\frac{\pi^2}{\sqrt{2}\lambda}\mu_o A^2 M_s M_s' e^{-\frac{2\pi t_{NM}\sqrt{2}}{\lambda}} \tag{1.6}$$

where M_s, M_s' are the values of saturation magnetization of the two ferromagnetic layers, A
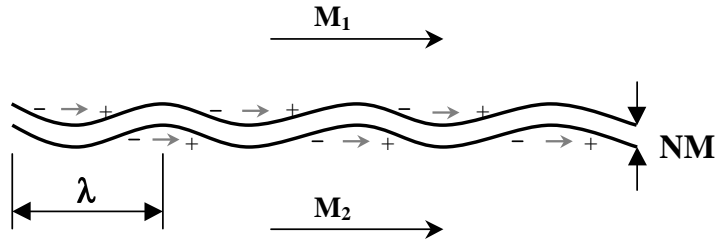
Figure 1.3: Schematic of layer geometry giving rise to Néel's "orange–peel" coupling in ferromagnetic layers separated by nonmagnetic spacers (NM).

is the amplitude, and λ is the wavelength of topographically correlated interfaces, which are separated by a nonmagnetic spacer the thickness of which is t_{NM}.
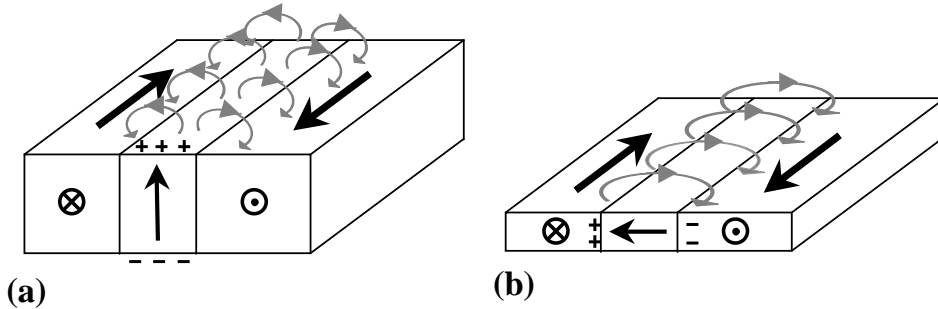
Figure 1.4: Schematic representation of a Bloch wall (a) and a Néel wall (b) in single layers films. The stray fields associated with each domain wall are schematically shown by brighter lines.

In addition to the various kinds of magnetostatic interactions between layers which have been discussed above, it is also possible to observe local magnetostatic interactions between domain boundaries in such films [23, 24]. A domain wall will always have a pole density associated with it. It will have an associated stray field, which can exert a local force on an adjacent film in a multilayer structure. This can result in a modification of the structure and energy of the domain walls, and in an effective attraction or repulsion between two domain walls in adjacent films. The total energy of a domain wall consists of the sum of the exchange, the anisotropy, and the magnetostatic energies. The spin configuration in the domain wall is determined by the minimization of this total energy. It has been found that in very thick films, as in bulk materials, so-called Bloch walls are present, in which the magnetization turns about an axis in the plane of the film and perpendicular to the plane of the wall. As a consequence of the anisotropic shape of thin films, the energies and the widths of domain walls in thin films are very different from those in bulk materials. At the intersection of the wall with the surface of the specimen free poles occur, which lead to magnetic stray fields. In thin films, however, the poles are at a

distance equal to the film thickness, so that high magnetic stray fields exist. The fact that the stray field energy plays such an important role in thin films leads to a new type of domain wall, first predicted by Néel [41]. When the film thickness is small, the magnetostatic energy of the wall can be reduced if the spins in the wall rotate about an axis perpendicular to the plane of the film. Free poles are then formed not on the film surface, but on the wall surface. Schematic drawings of these two wall structures and the stray fields are schematically shown in Fig. 1.4.

(a)   (b)   (c)
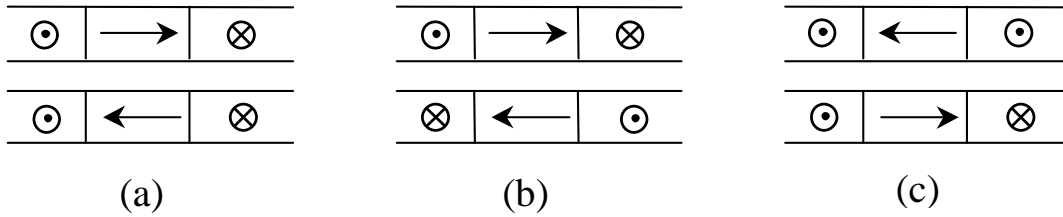
Figure 1.5: (a) Néel wall pair separating parallel domains; (b) wall pair separating antiparallel domains; (c) a wall-quasiwall pair.

Examination of Fig. 1.4 shows that the effective magnetization of a Bloch wall is perpendicular to the film plane, while that of the Néel wall lies in the plane. This implies that two superimposed Néel walls of opposite polarity can exist in a nearly closed flux loop configuration. This effect lowers the energy of pairs of Néel walls in multilayer films by comparison with that of Bloch walls, and makes them the favored structure. The demagnetized Néel configuration can exist in three different situations, shown in Fig. 1.5. In Fig. 1.5 (a) we see a pair of walls separating domains in each film, in which the superimposed domains are parallel. This is a configuration which might be expected when the film as a whole has positive coupling. Fig. 1.5 (b) shows the walls separating antiparallel domains, as might be expected in films exhibiting negative coupling. When another film is deposited on top of the first film, another way of reducing the magnetostatic energy of the Néel wall becomes possible. The flux of the Néel wall can be closed through the other film by inducing a second Néel wall in which the magnetization is antiparallel to the magnetization in the first Néel wall. The second wall is called a quasi-Néel wall as it is not a true boundary between domains with opposite magnetizations [42]. Fig. 1.5 (c) shows that the wall in one film, separating two domains, has induced a quasiwall in the second film.

The domain walls might be close together but not superimposed. Let us suppose that the magnetization of the two walls are parallel, as schematically shown in Fig. 1.6 (a). Such a configuration is presumably imposed by a field applied along the perpendicular to the domain wall. As a result of the previous considerations, the magnetostatic interactions between the walls should tend to bring them very close together. Indeed, that is not the case. The Néel wall in each film induces a quasi-wall of opposite magnetization in the other film. In this case the wall-quasi-wall interaction within each film will be repulsive and one may expect a certain
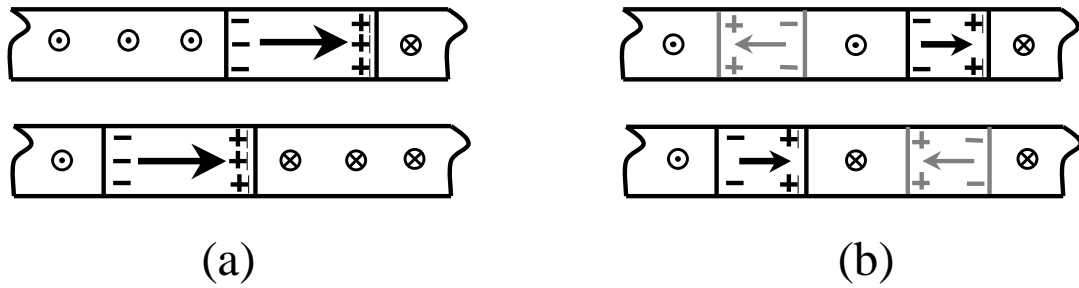
Figure 1.6: (a) Theoretical structures and positions of two Néel walls with parallel magnetizations; (b) Model of a pair of Néel walls and of the quasi-Néel walls induced by them.

separation distance to be established. The domain walls, with their parallel magnetization, will therefore not be superimposed but will lie close together. Such a configuration is shown in Fig. 1.6 (b).

Chapter 2

Experimental aspects

The goal of this chapter is to provide a basic description of the experimental techniques involved in this work. The chapter starts with a short overview of commonly employed magnetic imaging techniques. The magnetic contrast mechanism achieved by exploiting X-ray magnetic circular dichroism is then also described in the first section of this chapter, Sec. 2.1.

The photoelectron emission microscope used for imaging of magnetic domains is presented in Sec. 2.2, with some emphasis on the way the magnetic information can be extracted. In the second part of the same section, element-specific vector magnetometry using XMCD-PEEM is demonstrated.

Besides the magnetic characterization, the samples have also been investigated with respect to their structural and morphological behavior. Details of the sample preparation and the surface investigation techniques employed are shortly outlined in the last section of this chapter, Sec. 2.3.

2.1 Magnetic contrast mechanism in photoemission microscopy

Magnetic domains are the elements of the microstructure of magnetic materials that link the basic physical properties of a material with its macroscopic properties and applications. The analysis of magnetization curves requires an understanding of the underlying magnetic domain structure. Furthermore, the determination of the local domain alignment can be used to identify, and quantify, the possible interlayer and intralayer coupling mechanisms present in these films. This situation has led to the development of a number of experimental techniques for determining the domain structure of a ferromagnet: the Bitter method, Lorentz microscopy, scanning electron microscopy with polarization analysis (SEMPA), spin polarized scanning tunnelling microscopy (SPSTM) and optical microscopy making use of various magneto–optical effects to generate contrast of the signals coming from differently magnetized regions in the sample [43].

The imaging of magnetic domains by means of a photoemission electron microscope was reported already in 1957 [44]. These experiments exploited the deflection of the emitted electrons

due to the Lorentz force in the magnetic stray field above the sample surface. This contrast mechanism may be seen as the emission counterpart to the transmission Lorentz microscopy. The Lorentz force contrast mechanism requires reasonably high magnetic stray fields, and, therefore, works best with hard magnetic materials. It does not provide, however, any elemental selectivity.

The magnetic domain structure of a multilayer on an appropriate length scale can be obtained by magnetic microscopy in its many and various forms [45], but the magnetic mapping is typically averaged by a depth weighting factor and does not resolve the magnetization directions of the individual layers. One exception is magnetic imaging exploiting X-ray magnetic circular dichroism (XMCD) [46] (magneto-optical techniques [47] also have this capability with spatial resolution but only for very particular systems).

The development of magnetic dichroism techniques in X-ray absorption spectroscopy [48] has placed XMCD as a new way for imaging magnetic domains at the experimenter's disposal. Today, XMCD is a world-wide used technique for the determination of element-specific magnetic properties [49] and vector magnetometry [50], even identifying the hysteretic behavior of an ultrathin buried magnetic layer [51]. Magnetic dichroism means that the shape of a photoabsorption or emission spectrum and the relative intensity of the spectral features varies distinctly with a change of the magnetization direction or with a change of the polarization state of the incident light. The microscopic origin of this effect involves the interplay of spin–orbit coupling and exchange interaction in the electronic states which participate in the photoexcitation processes. The principle of magnetic dichroism in photoabsorption is explained in Fig. 2.1, for a

Figure 2.1: Principle of X–ray magnetic circular dichroism in X–ray absorption illustrated for the case of L_3 edge absorption in a $3d$ transition metal. The transitions occur from a $2p_{3/2}$ core shell to $3d$ empty conduction band states above the Fermi level, labelled E_F.

$3d$ transition metal. The circularly polarized light is used to excite electrons from a spin–orbit split core level, for example, a p level. Due to the spin–orbit coupling in the core electronic state, the transition matrix element becomes spin-dependent, causing the excited electrons to

be spin-polarized. A spin splitting of d states is assumed, and, as a consequence, there are more empty spin up than spin down states. Since momentum must be conserved during optical excitation, the photons will transfer their angular momentum to the excited photoelectron. If the photoelectron originates from a spin–orbit split level, e.g. $p_{3/2}$ level (L_3 edge), the angular momentum of the photon spin can be transferred in part to the spin through the spin–orbit coupling. Photons with their opposite angular momentum will excite photoelectrons with opposite spins. Since the $p_{3/2}$ (L_3) and $p_{1/2}$ (L_2) levels have opposite spin–orbit coupling, the spin polarization will be opposite at the two edges. Since spin flips are forbidden in electric dipole transitions governing X-ray absorption, spin-up (spin-down) photoelectrons from the p core shell can only be excited into spin-up (spin-down) d empty states. Hence, the spin split valence shell acts as a detector for the spin of the excited photoelectron, and the transition intensity is proportional to the number of empty d states of a given spin.

The dichroism in the initial absorption signal is transferred to the emitted electrons in a two-step process. The photoexcitation of a $2p$ electron creates a core hole in the $2p$ shell. This core hole decays within a certain lifetime either by emission of fluorescence radiation or by an Auger process. In the latter case the magnetic dichroism in the absorption is transferred to the Auger electron yield. On their way to the sample surface the characteristic Auger electrons experience inelastic scattering events and thus produce a cascade of secondary electrons. In a first approximation, the intensity of the secondary electrons is proportional to the number of initially excited Auger electrons. In this way, the XMCD signal created in the initial step of photoabsorption is transferred via the intermediate step of the Auger electron emission finally to the low-energy secondary electrons. The total electron yield that is measured as the total number of emitted electrons at the surface decays exponentially as a function of X-ray penetration depth. Siegmann [52] has shown that the escape depth in the transition metals is largely determined by the scattering process from filled to empty states and is therefore inversely proportional to the number of d–holes. It is highest for materials with completely filled d bands like Cu, Ag, and Au. Electron escape depths of 17 Å for Fe and 25 Å for Co and Ni have been experimentally measured in the total electron yield technique, at the L_3 edge, for samples prepared as wedges [53]. This relatively large information depth of XMCD in total electron yield recommends this technique for the study of coupled magnetic films. As a rule of thumb one can still "see" layers that are buried as deep as three times the electron escape depth [54].

Circularly polarized X-rays are particularly useful for the study of ferromagnets, systems with a net magnetic moment. Figure 2.2 shows an X-ray absorption spectrum for 8 ML Co/20 ML $Fe_{50}Mn_{50}$ epitaxially grown as a continuous film on Cu(001) as a substrate. The different intensities at the L_3 and L_2 edges correspond to parallel and antiparallel orientation of the photon spin direction and magnetization. These differences are quantitatively related to the size of the spin and orbital magnetic moments by the sum rules [55, 56]. The intensity changes as a function of photon energy lend itself as contrast mechanism for X-ray microscopy. The former
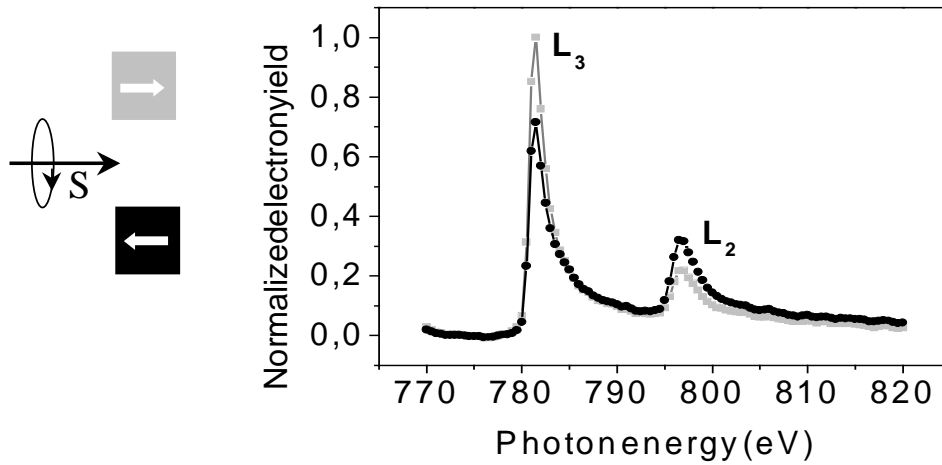
Figure 2.2: Illustration of X–ray absorption magnetic circular dichroism spectra caused by unidirectional orientation of the magnetic moments of 8 ML Co/20 ML $Fe_{50}Mn_{50}$/Cu(001) relative to the photon spin. The left-hand side sketch shows schematically the relative orientation of the photon spin and magnetization directions. The peak intensity at the Co L_3 (L_2) absorption edge is higher (lower) for parallel alignment of the photon spin and magnetization direction, respectively.

contrast mechanism is a variation of the electron yield caused by a change in photon energy. For example if the photon energy is tuned to the L_3 edge energy of element A, the measured signal from the sample will emphasize A over other elements. A second contrast mechanism is based on X-ray polarization. If we use, for example, circularly polarized light, regions of the sample with element A whose magnetization direction is parallel to the photon spin are highlighted. Magnetic domains with a local magnetization vector parallel or antiparallel to the photon spin $\overrightarrow{q}$ will exhibit a dark (bright) contrast, because areas with $\overrightarrow{M}$ parallel and antiparallel to $\overrightarrow{q}$ have different secondary electron yields. Magnetic domains with $\overrightarrow{q} \perp \overrightarrow{M}$ exhibit intermediate contrast.

Hence, magnetic circular dichroism can be used to determine the direction of the atomic magnetic moments and, therefore, fulfills the requirement for a magnetic contrast mechanism in magnetic microscopy.

2.2 The photoelectron emission microscope

In a conventional photoelectron emission microscope, or PEEM, the sample is illuminated by a light source, typically in the ultraviolet (UV) spectral range, which causes it to emit electrons. An image of the sample surface is formed using the emitted electrons, by an electron-optical imaging system. Two contrast mechanism are available in UV-PEEM: topographical contrast and work function contrast. Topographical contrast is due to the distortion of the electric field

around surface topographical features. The field distribution distortions disturb the electron trajectories which leads to image contrast. Work function contrast is manifest in the intensity modulation of the photoemission intensity due to the different emission probability in regions of different work function. Additional imaging modes are available when X-ray photons are used to stimulate photoelectrons. Elemental contrast is achieved by tuning the incident X-ray wavelength through absorption edges of elements. Areas on the surface containing the corresponding element emit more photoelectrons and thus appear brighter in the PEEM image at the given absorption edge X-ray energy.

In photoemission microscopy, it is not the resolution that is the primary motivation for the field, since other methods have better resolution (down to the atomic scale) [57, 58], and the fundamental limit for PEEM is around 20 Å[59]. For many applications element specificity is more important than high lateral resolution. Materials of magnetic storage media or the building elements of the spin-electronic devices are often composed of several chemical elements. It thus becomes necessary to distinguish the various magnetically active components in a system.

Today, there are several main areas of application of PEEM: the investigation of chemical surface reactions, e.g. the real time observations of the spatio-temporal behavior of catalytic reactions [60], the element specific imaging of the surfaces using tuneable X-rays from a synchrotron radiation source [61], and magnetic domain imaging exploiting the magnetic X-ray circular dichroism (XMCD) [46, 62].

The photoemission microscope used in this work is a commercially available Focus IS-PEEM, with a resolution in the threshold photoemission that is better than 30 nm. The sample illuminated by UV light or an X-ray beam is located in front of the electrostatic immersion objective lens as shown in Figure 2.3. The principle of image formation involves an electrostatic tetrode lens and a contrast aperture. During the operation of the microscope the sample is held at ground potential and the photoemitted electrons are accelerated in an external electrostatic field applied in between the objective lens and the sample of about 5–7 kV/mm. Image contrast can be optimized by a set of circular diaphragms with different sizes mounted onto a slide which can be positioned in-situ by a piezo-motor. This contrast aperture can be conveniently adjusted during the operation of the instrument and its size can be selected between 500 and 30 μm. The influence of non-spherical aberrations of the electron optics are corrected by an electrostatic octupole stigmator inserted into the back focal plane of the objective. In addition, the stigmator may serve as an x, y-deflector by means of which the field of view can be changed without moving the sample. A continuously variable field aperture (iris) in the first intermediate plane allows the selection of the field of view, in particular for microspectroscopy purposes. The image is magnified by two projective lenses, intensified by a multichannel plate and converted into visible light by means of a scintillator crystal. The image is then computer recorded with 12-bit resolution by a Peltier–cooled camera (PCO SensiCam). The camera accommodates variable exposure times, with typical image acquisition times of a few seconds to several tens

CCD-camera

YAG-screen

Channelplate

2. Projective lens

1. Projective lens

Field aperture

Stigmator-deflector

Contrast aperture

Object lens

$h\nu$

Sample stage
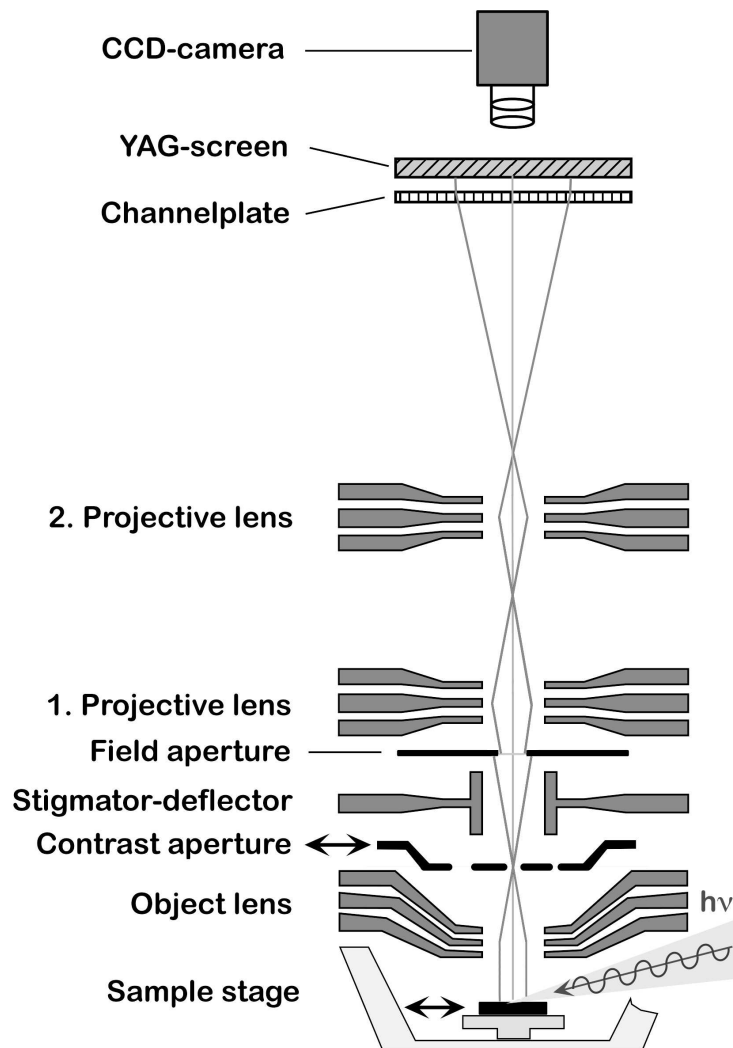
Figure 2.3: Schematic set–up of a photoemission electron microscope Focus IS–PEEM [63].

of seconds. The sample holder forms an integral part of the electron optical column. It is fixed by three springs at the object plane of the microscope. In this way the uncontrolled motions of the sample relative to the objective lens are greatly reduced, and the image quality is less affected by vibrations. The lateral movement of the sample in the object plane is controlled by two orthogonal piezo-driven microslides. These allow a convenient positioning of the sample within a scan area of 5 mm × 5 mm.

The microscope can be operated in two imaging modes: a survey mode and a high resolution mode. The high-resolution mode employs high extraction voltages resulting in a field of view down to 20 μm. The survey mode works with low-extraction fields, and the field of view may be as high as 700 μm.

The PEEM measurements were performed at the beam line UE56/2–PGM2 of BESSY II in Berlin. Circularly polarized light with a degree of polarization of about 80% was used, incident to the sample under an angle of 60° from the surface normal. For imaging of magnetic domain patterns, magnetic X-ray circular dichroism (XMCD) in the total photoyield at the L_3 absorption edge was exploited. In a single image the magnetic information due to magnetic dichroism is superimposed onto the contrast generated by the sample surface topography or inhomogeneous distribution of the individual components of the sample. In order to separate magnetic and non-magnetic contributions to the image contrast, one takes advantage of the fact that a reversal of the light helicity reverses the "magnetic information contrast", while leaving the non-magnetic contrast contribution unaffected. Therefore, by subtracting two images taken at the same photon energy, but with opposite light helicity, the non-magnetic contribution is eliminated. Alternatively, one can calculate the XMCD asymmetry image, defined as the difference of the images acquired for opposite helicities divided by their sum,

$$A_{XMCD} = \frac{I_{RCP} - I_{LCP}}{I_{RCP} + I_{LCP}} \tag{2.1}$$

where I_{RCP}, (I_{LCP}) denotes the image recorded with right (left) circularly polarized light at the L_3 and L_2 absorption line. The asymmetry is proportional to the projection of the local magnetization direction on the light incidence direction for a given element and constant magnetic moment. Due to this directional dependence one can determine the local direction of the magnetization vector by acquiring two different images at the same position of the sample for two different azimuth incidence directions of the exciting X-rays. Magnetic domains with a magnetization direction parallel to the film plane will undergo a contrast reversal after a rotation of 180° of azimuth angle. The asymmetry of magnetic domains with magnetization direction oriented parallel or antiparallel to the normal of the surface does not change since the light component perpendicular to the film plane does not change by this rotation. An example is shown in Fig. 2.4. It presents magnetic domain images of a 10 ML Fe film epitaxially grown as a continuous film on W(001). Two images for two different azimuthal orientations of the light incidence, indicated by arrows labelled "$h\nu$", have been obtained by rotating the sample about its surface normal and re-adjusting the lateral position in order to keep the same field of view. The two images represent thus two independent measures of the local magnetization direction projection at each point of the image, which suffice to determine the two degrees of freedom of the magnetization direction in angular space. Comparing the two images, it is in particular easy to distinguish magnetization directions, in the film plane, along the photon spin and magnetization directions perpendicular to the photon spin. Arrows in same domains indicate the local magnetization directions resulting from such an analysis. Different gray scale levels correspond to different projections of the local magnetization direction onto the direction of incoming light. A darker (brighter) gray scale level corresponds to a more antiparallel (parallel) component of magnetization direction with respect to the light propagation vector. Looking to the images
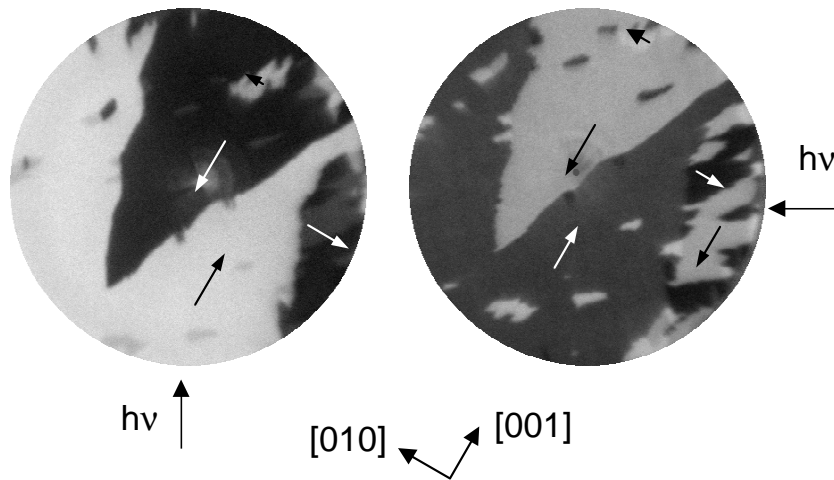
Figure 2.4: Magnetic domain images of a 10 ML Fe on W(001). The two images show the same region of the sample for two different light incidence azimuth angles as indicated by arrows labelled "$h\nu$". The local magnetization directions are indicated in the domains.

of Fig. 2.4 one recognizes that the tip-like domain with a magnetization direction along $[00\bar{1}]$ undergoes a contrast reversal upon the near-90° change in the X-ray incidence azimuth. No such a contrast reversal is observed in the domains where the local magnetization direction is oriented along $[010]$ and $[0\bar{1}0]$ crystal axes.

2.3 Experimental details

In this work, sample preparation and characterization was carried out in–situ under ultra high vacuum (UHV) conditions in two distinct UHV-systems. Both UHV-systems are equipped with surface investigation techniques as: Auger electron spectroscopy (AES), low energy electron diffraction (LEED) to acces the structural information, and magneto–optical Kerr effect (MOKE) to probe the film magnetization. The photoemission experiments with synchrotron radiation were carried out in a UHV-system, called PEEM chamber in the following, equipped with a photoelectron emission microscope (PEEM). The second UHV-system, called MBE-machine (molecular beam epitaxy machine) consists of separate chambers for substrate preparation, sample transfer, sample preparation, surface analysis (scanning tunnelling microscopy-STM), magneto-optical Kerr effect, allowing the preparation and characterization of the sample without any exposure to ambient atmosphere.

The base pressure in each chamber of the MBE–machine is in the low 10^{-10} mbar range. Sample treatment is accomplished in the analysis chamber which is equipped with a sputter gun with a differential pumping line, resistive current heating, and surface analysis units for

low energy electron diffraction and Auger electron spectroscopy. Access to the different chambers is provided by magnetic linear and rotary motion drives with perpendicular handing over. Sample holders in the preparation and analysis chamber can be positioned by xyz manipulators. Ultrahigh vacuum is maintained by ion getter and titanium sublimation pumps for each chamber. The substrate used for growing the films was a disk-shaped Cu single crystal with the [001] direction normal to the surface. The clean Cu(001) surface was prepared by cycles of 1 keV argon ion bombardment at 300 K until no contaminations were detectable by AES, followed by annealing at 873 K for 15 minutes. The substrate temperature was controlled by an N-type thermocouple attached to the sample holder. The presence of surface contaminants is below the detection limit of the Auger system ($\approx 2\%$ of a ML). This cleaning procedure was repeated until a sharp (1×1) LEED pattern was observed coinciding with large atomically flat terraces. Typical STM images of Cu(001) surface show atomic steps with a mean separation larger than 100 nm. This corresponds to a deviation below $0.1°$ from a (001) surface plane. The growth mode was monitored in situ using reflection high energy electron diffraction RHEED (STAIB) technique [64]. A typical RHEED measurement system consists of an electron gun, a phosphor screen and an image-processing hardware and software. The electron beam impinges onto the sample surface at an angle that is typically in the range of $0.5°$–$2.5°$. The diffracted intensity pattern is then converted into visible light by a phosphor screen. The intensity of the specular spot was measured using a computer-controlled CCD camera and data acquisition system. The inset of Fig. 2.5 shows the RHEED pattern of 8 ML Co/Cu(001) for an incidence
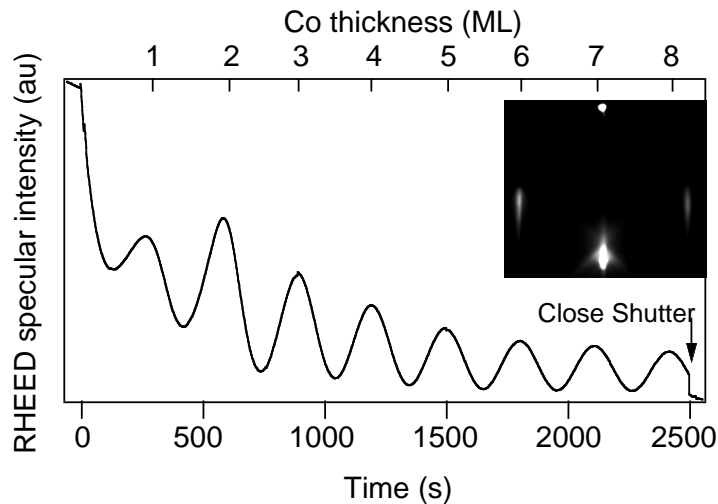
Figure 2.5: RHEED specular beam intensity oscillations vs time acquired during epitaxial growth of Co on Cu(001). The inset shows the RHEED pattern after deposition of 8 ML Co on Cu(001).

angle of $0.7°$–$0.8°$ (first anti–Bragg condition) and an azimuth direction near the [110] Cu crystallographic axis. The specular beam intensity shows oscillatory behavior as a function of time

during evaporation of Co, Fig. 2.5. Within the kinematic approximation the intensities of the diffracted beams vary due to changes of the surface step density during film growth [65, 66]. These oscillations are especially pronounced when the angle of incidence is chosen that leads to destructive interference ("out-of-phase" condition) between adjacent terraces for a given beam. For the ideal layer-by-layer growth, the oscillations in the step density will lead to intensity oscillations of the specular beam with constant amplitude and frequency in a RHEED experiment. In this case the completion time for a monolayer corresponds to the time between two oscillation maxima. The gradual decrease of the amplitude of oscillations, Fig. 2.5, as the growth proceeds, can be attributed to roughening of the growing surface. Therefore, the intensity oscillations of RHEED provide a useful method for in-situ layer quality control and thickness measurement during MBE growth. Additionally the structure and morphology of the growing films can be determined from a detailed analysis of the diffraction pattern. This allows the observation of, for example, superstructure formation. In principle one could also gain important information from a quantitative analysis of the intensity variation of the specular spot during growth since it is related to changes in morphology. Controlled by RHEED intensity oscillations, the deposition in each experiment is stopped at the desired film thickness. However, the exact film thickness determination is done by using STM after film deposition.

The films studied in this work were grown on the clean substrate at room temperature by electron beam assisted thermal evaporation. Fe, Mn, Co and Ni rods were cut from high purity wires (99.99% purity) of $2\,\text{mm}$ diameter for Fe, Co, Ni and $5\,\text{mm}$ diameter for Mn. $Fe_{50}Mn_{50}$ alloys were obtained by simultaneous deposition of Fe and Mn from two different sources. The evaporants were degassed by prolonged heating before actual experiments. The rate of deposition, typically of 1–2 ML per minute for $Fe_{50}Mn_{50}$ alloy and 0.2 ML per minute for Co, was determined by means of RHEED intensity oscillations of the specular spot recorded during the deposition of the film.

The composition and thickness of the $Fe_{50}Mn_{50}$ alloy has been complementarily checked by using cylindrical mirror analyzer based Auger electron spectroscopy (AES). A beam of energetic electrons of 3 keV is used to eject a core level electron from surface atoms. The energy of the Auger electron, specific to the atom from which it originated, is measured. The quantity of Auger electrons is proportional to the concentrations of the atoms on the surface and in the near surface region. The Auger electrons have a very short path length before inelastic scattering occurs, which makes the spectra characteristic of the outermost atomic layers. In the case of a Fe_xMn_{1-x} alloy film on Cu(001) as a substrate, one can experimentally get the Auger electron intensities of the three elements I_{Fe}, I_{Mn} and I_{Cu}, and obtain the ratio between the Cu and Mn (Fe) Auger intensities as $R_{Mn} = \frac{I_{Cu}}{I_{Mn}}$ ($R_{Fe} = \frac{I_{Cu}}{I_{Fe}}$). The Fe concentration x can be estimated using formulas (2.2–2.3) [67]:

$$R_{Fe} = \frac{S_{Cu} \cdot \exp^{-\frac{d}{\Lambda_{Cu}}}}{S_{Fe} \cdot x \cdot (1 - \exp^{-\frac{d}{\Lambda_{Fe}}})} \qquad (2.2)$$

$$R_{Mn} = \frac{S_{Cu} \cdot \exp^{-\frac{d}{\Lambda_{Cu}}}}{S_{Mn} \cdot (1 - x) \cdot (1 - \exp^{-\frac{d}{\Lambda_{Mn}}})} \qquad (2.3)$$

where d is the thickness of the FeMn film in ML. S_{Cu}, S_{Fe}, S_{Mn} are the sensitivities of the Auger electron transitions for Cu, Fe and Mn, λ_{Cu}, λ_{Fe}, λ_{Mn} are effective inelastic mean free paths.

The magnetization hysteresis loops have been measured by longitudinal magneto–optic Kerr effect (LMOKE) using s or p-polarized light [68]. In LMOKE, linearly polarized light has its polarization rotated and becoming elliptically polarized upon reflection from a magnetized surface. As the applied magnetic field is cycled for measuring a magnetization curve, the rotation changes and hence, also the beam intensity reaching the detector. Light from a laser diode, operated at a wavelength of $\lambda = 675$ nm, passes through a polarizer, and is focused onto the sample by an optical lens. The angle of incidence is of about $70°$ from the normal of the surface of the sample. The reflected light passes through a 50 kHz photoelastic modulator, an analyzing polarizer and finally, the beam reaches a photodiode detector. The signal goes to a lock-in amplifier, where the detection of the signal is accomplished by phase sensitive detection, using a reference signal from the modulator controller. The magnetic field is applied in the plane of the sample. The linear background caused by the Faraday effect [68] through the optical lens was subtracted.

Scanning tunnelling microscopy (STM) experiments were carried out with a commercial room temperature UHV-STM (Omicron GmbH) [69] operating at a base pressure of 2×10^{-10} mbar. All the STM images shown in this work were recorded at room temperature in the constant-current mode of operation. The vertical sensitivity of the tube scanner was calibrated on monoatomic steps of the Cu(001) substrate. All images presented were plane fitted on atomically flat terraces to correct the tilt of the sample. The scanning tips are made from polycrystalline PtIr. Spectroscopic information is gained by measuring at each pixel of a topographic scan the variation of the tunnelling current as a function of voltage at a constant tip–sample separation, under open feedback conditions. The acquisition time for each spectroscopy data point was 160 μs with a number of 41 points in each spectroscopy curve. The epitaxial growth of 5 ML Co on Cu(001) as a substrate is illustrated by the STM topographic image shown in Fig. 2.3. A nearly filled fifth atomic layer, with small brighter islands corresponding to the nucleation in the sixth layer and holes (darker features) one atomic layer depth, reaching down to the fourth layer, are clearly visible.

The background pressure in the PEEM chamber is in the 10^{-10} mbar range, while during deposition it could rise up to the lower range of 10^{-9} mbar. The films were deposited by elec-
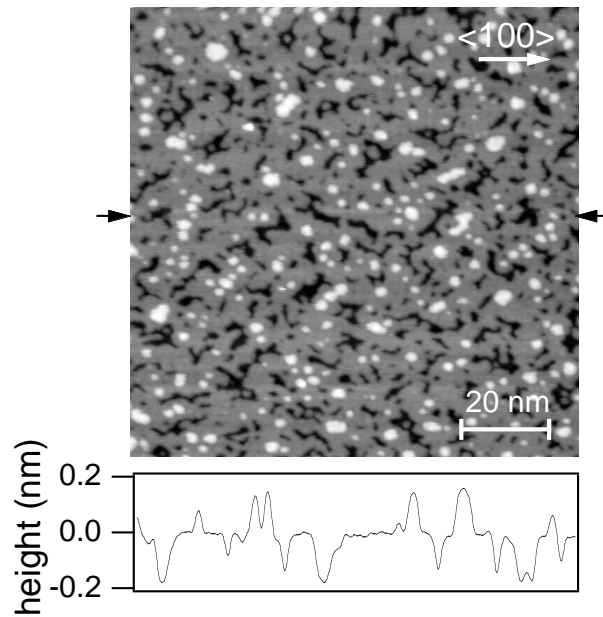
Figure 2.6: STM constant current topography image of 5.0 ML Co/Cu(001). Tunnelling voltage and current +0.2 V and 0.2 nA, respectively. The line profile taken along the width of the image at the position marked by arrows is shown at the bottom of the image.

tron beam assisted thermal evaporation (as described above). The rate of deposition of growing films (Co, FeMn, FeNi, Cu), typically of about 1–2 ML per minute, has been measured by recording the intensity of the specular spot of the medium energy electron diffraction (MEED) during deposition. The micro-wedge-shaped samples have been prepared by placing a rectangular aperture of $2 \times 0.5 \, \text{mm}^2$ in front of the sample, at a distance of 1 mm to the sample surface [70]. During the evaporation of the films the sample has been rocked about the long axis of the aperture. The exact position on the wedge could be obtained by taking the ratio between the intensity at the L_3 absorption edge and the pre-edge intensity.

Chapter 3

Epitaxial growth and magnetic coupling across Fe$_{50}$Mn$_{50}$

The experimental results on the magnetic interlayer coupling across an AFM spacer layer, Fe$_{50}$Mn$_{50}$ in the present studies, are grouped together in this chapter. The characterization of the layer-by-layer growth and the surface morphology of Fe$_{50}$Mn$_{50}$ on Cu(001) are presented in Sec. 3.1. In Sec. 3.2 layer-resolved domain imaging and MOKE measurements on FeNi/Fe$_{50}$Mn$_{50}$/Co and Co/Fe$_{50}$Mn$_{50}$/Co trilayers outline the influence of surface roughness in the phase and strength of coupling. Sec. 3.3 and Sec. 3.4 present the interlayer coupling in Ni/Fe$_{50}$Mn$_{50}$/Co and Ni/Fe$_{50}$Mn$_{50}$/Ni trilayers on Cu(001). The latter leads to some conclusions on the magnetic spin structure of Fe$_{50}$Mn$_{50}$.

3.1 Growth and surface morphology of Fe$_{50}$Mn$_{50}$ alloy on Cu(001)

Magnetic properties such as interlayer exchange coupling, giant magnetoresistance, surface anisotropy, are closely related to the surface and interface morphology. It has been shown by Heinrich *et al.* that the strength of bilinear exchange coupling between Fe and Cr layers can be changed by as much as a factor of 5 by varying the substrate temperature during growth [71]. This behavior revealed clearly how the growth and surface morphology of the FM/AFM interface can influence the magnetic coupling behavior. Therefore, to gain deeper insight into magnetic interlayer coupling across Fe$_{50}$Mn$_{50}$ alloy thin films, the growth and morphology aspects were investigated first.

As a bulk material FeMn alloy exhibits a variety of different structural phases, depending on composition. In the Fe rich part of the phase diagram a supersaturated *hcp* solid solution ε has been found, while in the Mn rich part a solid solution of α-Mn is present. The Fe$_{50}$Mn$_{50}$ alloy as a bulk material has an *fcc* γ-FeMn structure. The stabilization of the antiferromagnetic *fcc* γ-phase is of particular importance especially as a possible application in spin valves [72].

The *bcc* α-phase and *hcp* ε-phase, both present in the phase diagram of Fe$_{1-x}$Mn$_x$ alloys, have a lower ordering temperature.

Ideal layer-by-layer growth in heteroepitaxy is generally believed to require a small lattice mismatch, immiscibility in the bulk, and an abrupt interface between substrate and film. For FeMn these requirements can be met by Cu(001) [73]. The (001) surface of Cu is a very popular substrate for growth of metallic thin films. Cu exhibits an *fcc* crystal structure and an equilibrium lattice constant $a_{Cu} = 3.61$ Å i.e., the misfit to γ-FeMn ($a_{FeMn} = 3.629$ Å) [74] amounts to $f = \frac{a_{FeMn} - a_{Cu}}{a_{Cu}} = 0.52\%$.
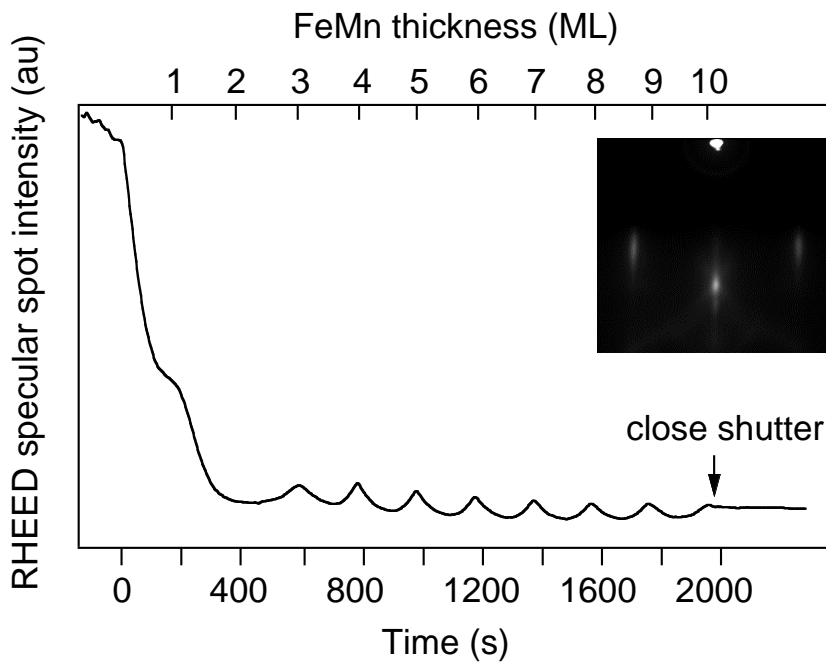
Figure 3.1: RHEED specular beam intensity oscillations vs time acquired during deposition of Fe$_{50}$Mn$_{50}$ alloy on Cu(001) as a substrate. The inset shows the RHEED pattern of 10 ML Fe$_{50}$Mn$_{50}$/Cu(001).

The growth of the films was monitored in situ by a RHEED experiment at gracing incidence. Figure 3.1 presents the RHEED specular spot intensity acquired during the growth experiment. The substrate temperature during deposition was held at 300 K, and the evaporation rate was about 0.5 ML/min. The inset of Fig. 3.1 shows the RHEED pattern for an incidence angle of 0.7°–0.8° (first anti-Bragg condition) and an azimuthal direction near the $\langle 110 \rangle$ Cu crystallographic axis after deposition of 10 ML Fe$_{50}$Mn$_{50}$. The presence of the RHEED oscillations is a strong indication for a layer-by-layer growth of Fe$_{50}$Mn$_{50}$ on Cu(001). The initial phase of the growth is characterized by a pronounced decrease of intensity and an intensity minimum at 2 ML Fe$_{50}$Mn$_{50}$. Additionally, visual inspection of the RHEED pattern reveals that after deposition of approximately 1 ML Fe$_{50}$Mn$_{50}$ this pattern becomes very diffuse. Connected to

the rise in intensity of the RHEED beams around 3 ML is an increase in spot sharpness. Above this thickness a regular intensity oscillation and an increase in sharpness of the diffraction spots have been observed. From these observations it is obvious that the initial growth mode of the Fe$_{50}$Mn$_{50}$ films is not a "perfect" layer-by-layer growth. The absence of regular intensity oscillations in the thickness range of 0–3 ML and the broadening of the diffraction spots are inconsistent with such a growth mode.

The morphology of Fe$_{50}$Mn$_{50}$ on Cu(001) has been studied for different coverages using scanning tunnelling microscopy . By depositing low coverages I will first address the quality of the bottom interface, between the Fe$_{50}$Mn$_{50}$ alloy and Cu(001). STM images have been taken in constant current mode, at room temperature. The sequence of STM images, together with selected line profiles, of different amounts of Fe$_{50}$Mn$_{50}$ deposited at room temperature on Cu(001) substrate are presented in Fig. 3.2.
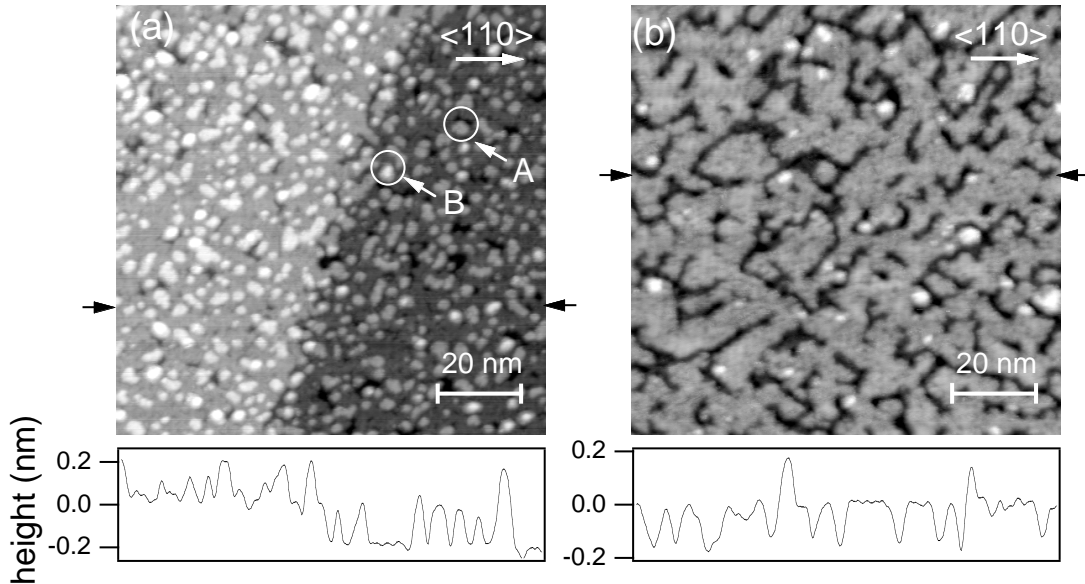
Figure 3.2: Sequence of STM constant current images measured at room temperature: (a) 1.3 ML Fe$_{50}$Mn$_{50}$ ($U_{sample} = 0.2$ V, $I = 0.1$ nA); (b) 2.7 ML Fe$_{50}$Mn$_{50}$ ($U_{sample} = 0.5$ V, $I = 0.2$ nA). Line profiles taken along the width of images, at positions marked by arrows, are shown at the bottom side of each image.

After deposition of 1.3 ML Fe$_{50}$Mn$_{50}$ alloy, Fig. 3.2 (a), the morphology of the surface is dominated by relatively small brighter dots corresponding to the nucleation of islands in the second layer, with an average density of 44×10^3 μm^{-2}, seemingly randomly distributed on top of a nearly closed first layer. Mean island sizes are typically of the order of 2–5 nm linear dimensions. A closer inspection of this image shows that while the first monolayer is not fully completed the nucleation and growth of the second one already becomes significant

(bright white islands). These islands resemble basically two different classes (labelled A and B in Fig. 3.2 (a)): (A) with an apparent height of 0.208 nm and (B) with an apparent height of 0.355 nm at $U_{sample} = 0.5$ V. The apparent height of islands of (B) type is not the double height of islands of (A) type. Therefore, it must be that A and B islands are of different constituent elements. The effect of imaging the (B), (A) type islands with a lower/higher apparent height is presumably due to a chemical contrast. Variation of the bias voltage shows a significant influence on the apparent height. For a negative bias voltage on the sample of about -0.6 V the apparent height of (A) type islands is 0.168 nm while of (B) type islands it is 0.303 nm. It can be seen that the apparent height of these islands depends on the bias voltage. A similar bias-dependent contrast has been observed previously in the Cu/W(110) system by Mo and Himpsel [75]. They attributed it to a Cu induced empty state at 0.6 eV above the Fermi level. Although band structure knowledge of the elements is needed to understand the bias-dependence corrugations in detail, it seems reasonable to attribute them to Cu. It may be that the corrugation reflects the diffusion of Cu through the surface of Fe$_{50}$Mn$_{50}$ alloy. Based upon the existing data it is not possible, however, to define a concise structural model. Further investigations with suitable methods (angle resolved ultraviolet photoemission spectroscopy (ARUPS), scanning tunnelling spectroscopy (STS)) should be applied for a full understanding.

In summary, at 1.3 ML there are exposed first monolayer, some holes that correspond to the substrate level and islands nucleated on top of the first monolayer which are one or two monolayers high. The two monolayers high islands (B) reflect the diffusion of Cu from substrate through the first FeMn layer, which act as a pinning centers for the further deposited film.

Deposition of 2.7 ML Fe$_{50}$Mn$_{50}$ alloy onto Cu(001), Fig. 3.2 (b), leads to bigger islands, with the island edges preferentially oriented along $\langle 100 \rangle$ crystallographic directions of the Cu(001) surface. Also, the density of "blobs" (brighter spots), islands nucleated in the next layer (in the third one), has substantially decreased, whereas the apparent width is not much affected and stays at a value of 5 nm.

Based on the STM results described above, the following initial growth mechanism could be proposed. Below 2 ML FeMn, growth proceeds via formation of two dimensional monolayer or bilayer islands in the typical size of a few nm. According to STM observations, the presence of these small islands promotes a decrease of the sharpness of the RHEED pattern and of the specular spot intensity in the 0–3 ML FeMn thickness range.

The formation of small islands in the first stage of growth in collaboration with the absence of RHEED oscillations has been observed in other metal-on-metal systems. Co on Cu(001), for example, grows initially in bilayer islands, followed by layer-by-layer growth [76]. The growth in this low coverage regime is mainly governed by surface free energy effects. It is known that the surface free energy of Co ($\gamma_{Co} = 2.7$ Jm^{-2}) is higher than that of Cu ($\gamma_{Cu} = 1.9$ Jm^{-2}). It follows then from Bauer's criteria for the dimensionality of the critical nucleus that the Co atoms will preferably agglomerate in the initial stage of growth. Thermodynamically, exposing

more of the substrate reduces the energy of the system.

The growth of Co on Au(111) also forms small islands two atomic layers high that coalesce with increasing coverage [77]. Here, bilayer growth has been attributed to the large lattice mismatch between Co and Au (14%). The mismatch leads to substantial strain energy in the growing film. The atoms relax in the second layer, thus bilayer islands reduce the overall strain energy of the film. The mismatch between $Fe_{50}Mn_{50}$ and Cu(001) is much less (–0.52%). In addition, analysis of the RHEED pattern and previous LEED experiments performed on this system indicates that the film remains pseudomorphic with the substrate up to a thickness of 26 ML $Fe_{50}Mn_{50}$ [78]. Therefore, stress relaxation as a driving mechanism for such a bilayer growth could not be involved in the case of epitaxial growth of $Fe_{50}Mn_{50}$ on Cu(001).

An alternative explanation relies on the different adatom mobility between the first and successive $Fe_{50}Mn_{50}$ layers. The difference is responsible for the transition from island nucleation to layer-by-layer growth after 3 ML as observed by STM. Since the surface is covered by a high density of small islands, a significant fraction of the incident atoms will arrive on top of the islands prior to coalescence. Atoms that adsorb on top of the islands may be hindered from descending onto the Cu(001) surface by the presence of a step edge barrier [79, 80]. This additional barrier leads to a build up of adatoms in the second layer prior to the completion of the first. Once the Cu(001) substrate is covered, $Fe_{50}Mn_{50}$ adatom mobility is increased. This increase produces a sharp transition between completion of the second atomic layer and growth of the third one.

The regular oscillations of the RHEED specular spot intensity observed above 3 ML $Fe_{50}Mn_{50}$ are regarded as the finger-print of layer-by-layer growth. Further, the morphology of the $Fe_{50}Mn_{50}$ alloys in a thickness range of 8 ML to 12 ML will be presented. The sequence of STM topographic images and selected line profiles for different coverages of $Fe_{50}Mn_{50}$ alloy layers are shown in Fig. 3.3. The STM topographic image of 8.26 ML $Fe_{50}Mn_{50}$, Fig. 3.3 (a), reveals large and atomically flat terraces. The brighter islands with an apparent height of 0.18 nm correspond to the 9th atomic layer. Small holes ($\approx$ 5 nm length) of one atomic layer depth are also present (darker features). In addition, a fine structure (intermediate gray level) with an apparent corrugation height of about 0.05 nm is recognized. This can be distinguished on the line profile displayed beneath the topography image as a modulation with a small amplitude. Upon increasing the thickness of deposited $Fe_{50}Mn_{50}$, Fig. 3.3 (a)–(c), the STM topographic images corresponding to 9.15 ML, 10.1 ML and 11.74 ML show mainly the same morphology. Hence, also STM confirms the nearly perfect layer-by-layer growth as already concluded from the presence of RHEED oscillations.

The high features 0.18 nm are steps/islands one atom high/deep. The question is then what is the fine structure seen in all the surface topography images of $Fe_{50}Mn_{50}$ in Fig. 3.3. The first tendency is to attribute the fine features observed in all STM topographic images to a real geometric effect. The atomic radius of Mn is 5 pm larger than of Fe and could account for
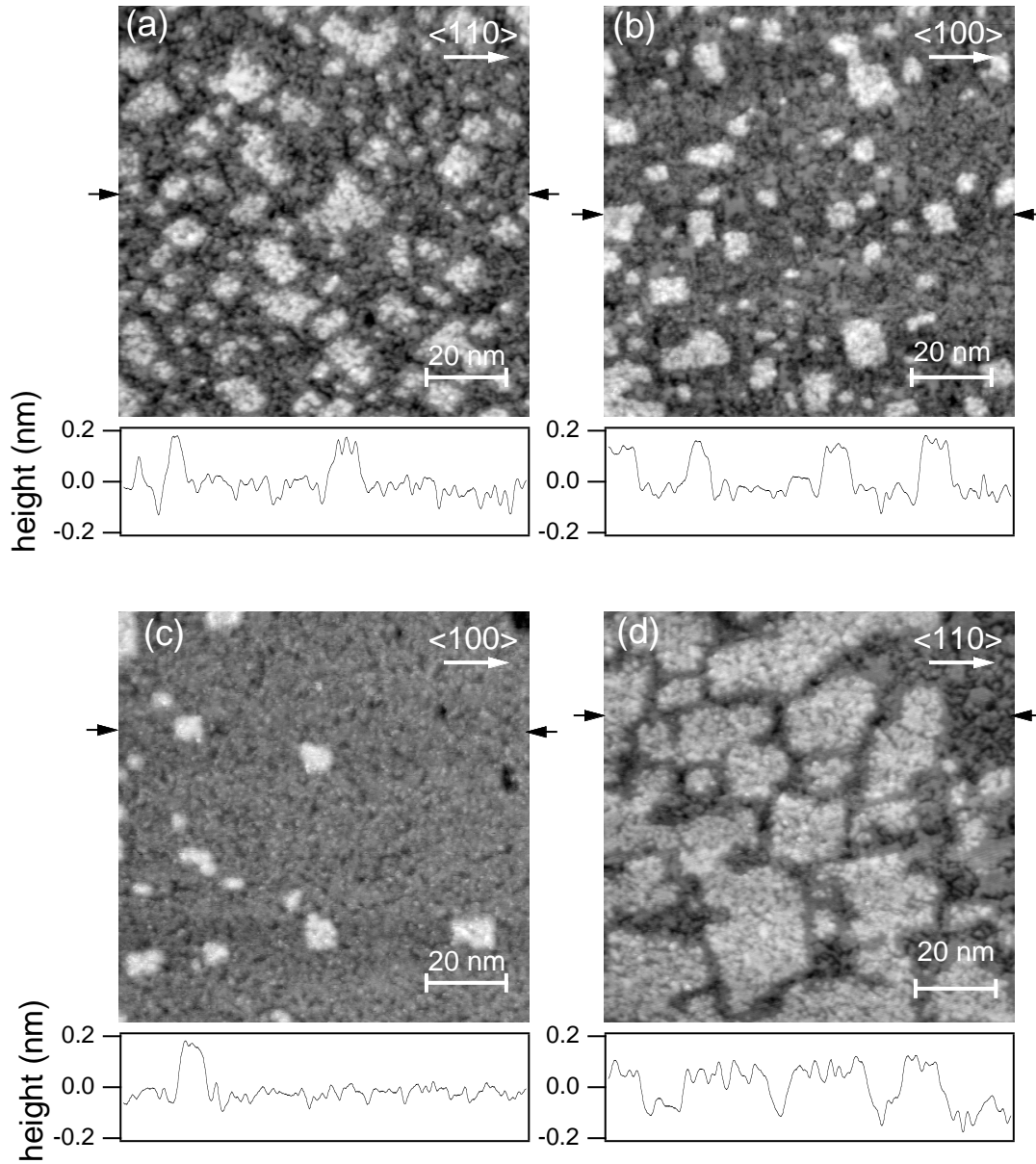
Figure 3.3: Sequence of STM constant current images measured at room temperature: (a) 8.26 ML Fe$_{50}$Mn$_{50}$; (b) 9.15 ML Fe$_{50}$Mn$_{50}$; (c) 10.04 ML Fe$_{50}$Mn$_{50}$; (d) 11.74 ML Fe$_{50}$Mn$_{50}$. Line profiles taken along the width of images, at positions marked by arrows, are shown at the bottom side of each image. Tunnelling current $I = 0.2$ nA, sample voltage $U_{sample} = 0.5$ V.

such effects. This implies that the tip retracts 5 pm when it is over a Mn atom. Therefore, the small features present in the topographic images with an apparent step height of 0.05 nm can not be attributed only to geometric effects. To identify the origin of the fine structures observed in the STM topographic images, scanning tunnelling spectroscopy (STS) measurements were performed. Fig. 3.4 (a) and (b) show current map images measured on the same area for positive and negative bias voltages. Fig. 3.4 (c) shows a constant-current topographic image of the same surface area as shown in panels (a) and (b). It is immediately evident from comparison of images (a) and (b) that the gray scale level of the related features changes with the sample bias voltage. Fig. 3.4 shows I–V curves acquired on the entire regions (A) and (B) marked in Fig. 3.4 (a). Qualitatively, in the (A) region the tunnelling I–V curve shows a plateau within 0–0.5 eV, followed by a linear increase of the current. In the negative region the tunnelling curve exhibits a strong exponential increase with a peak in dI/dV at –0.5 eV. When the tip is located over the (B) region, the tunnelling current shows a linear dependence for positive values of the bias voltage, while for negative bias voltage an exponential increase with a peak in dI/dV at –0.2 eV is observed. Since the tunnelling current for a positive bias voltage is higher (lower) above the B (A) region, in constant-current-mode the tip has to be withdrawn from (approached towards) the surface in order to keep the tunnelling current constant. Consequently, the apparent height is reduced for (A) and enhanced for (B) features.

In Fig. 3.5 line profiles taken in the panels (a), (b), and (c) of Fig. 3.4, at the same sample position, show a clear correlation between the features seen in the current map images and the small fine structure in the topography images. The curves labelled (a) and (b) in Fig. 3.5 correspond to the line profiles taken in the current map images for positive (0.4 V) and negative (–0.15 V) voltages, respectively. The (c) curve is a line profile taken in the topography constant current image. The vertical dotted lines are put at some selected positions to guide the eyes. When following the curve labelled (a) in Fig. 3.5, from left to right, some current peaks can be distinguished. They are correlated with a higher tunnelling current, for a positive voltage, when the tip is located over areas which appear brighter in Fig. 3.4 (a). At the same position on the sample, a negative voltage gives rise to a negative peak in the tunnelling current, darker areas in Fig. 3.4 (b). A closer look to the peaks seen in the line profile (a) and (b), Fig. 3.5, reveals that not only the height but also the width of these peaks is slightly different for positive and negative voltages. Now, since the topography image is measured at a positive bias voltage, in the light of the above discussion of Fig. 3.4, a current peak in curve (a) should induce a peak in the topography line profile (c). Indeed, this is what can be observed when the curves (a) and (c) are compared with each other. Most of the small features with 0.05 nm apparent corrugation height are related to features in the current map images.

The simultaneously measured topographic and spectroscopic images confirm clearly the chemical origin of the small features observed in the STM topographic images. The presence of the fine structures may be therefore associated with local concentration differences of the
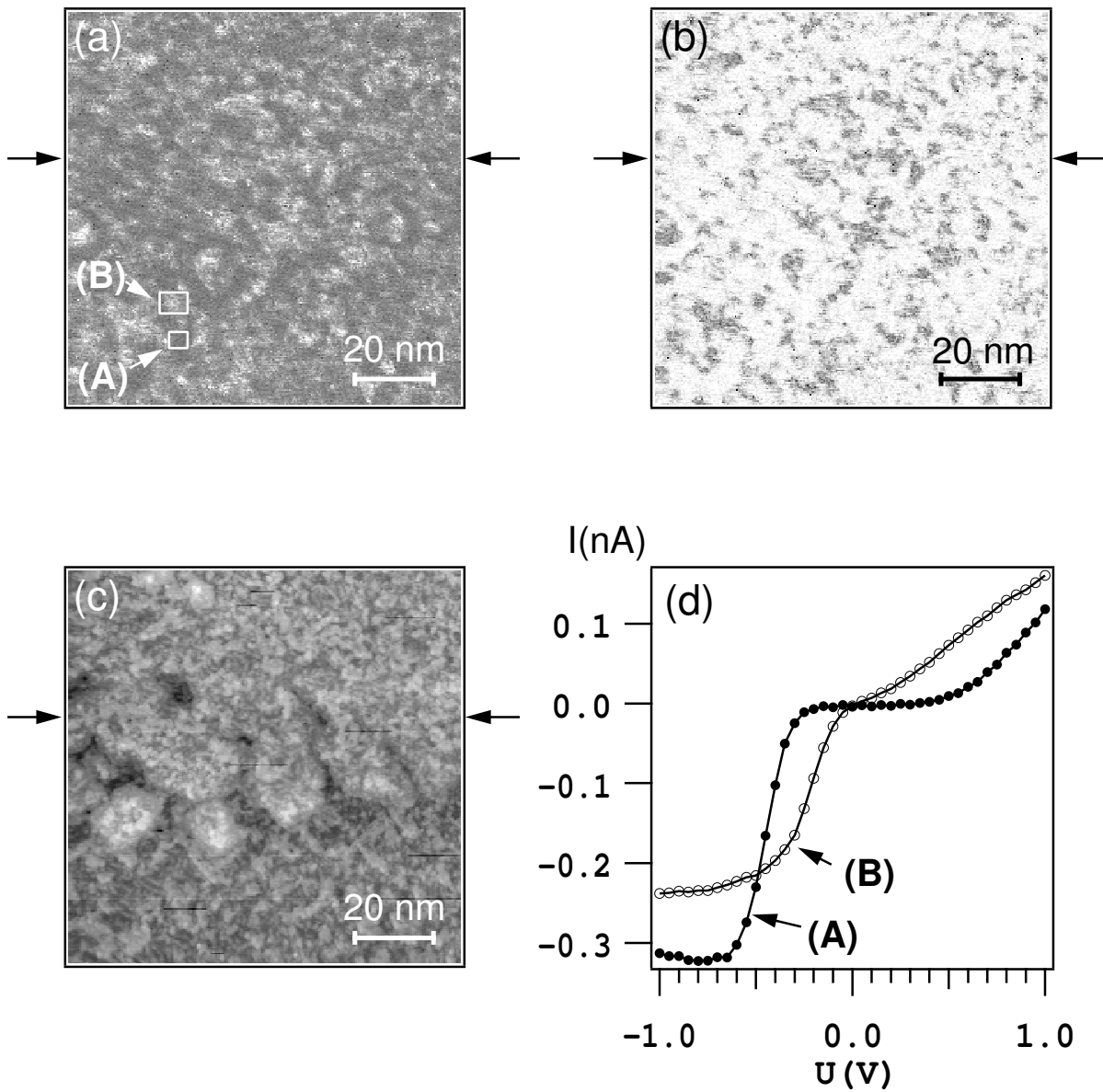
Figure 3.4: (a) Current map image at 0.4 V of 11.74 ML $Fe_{50}Mn_{50}$ epitaxially grown on Cu(001). (b) Current map image at -0.15 V, of the same area as in panel (a). (c) STM constant-current topographic image of the same surface area shown in panel (a) and (b). Tunnelling current $I = 0.2\,nA$, sample voltage $U_{sample} = 0.5\,V$. (d) Averaged I–V curves on the entire areas labelled (A) and (B) measured in panel (a).
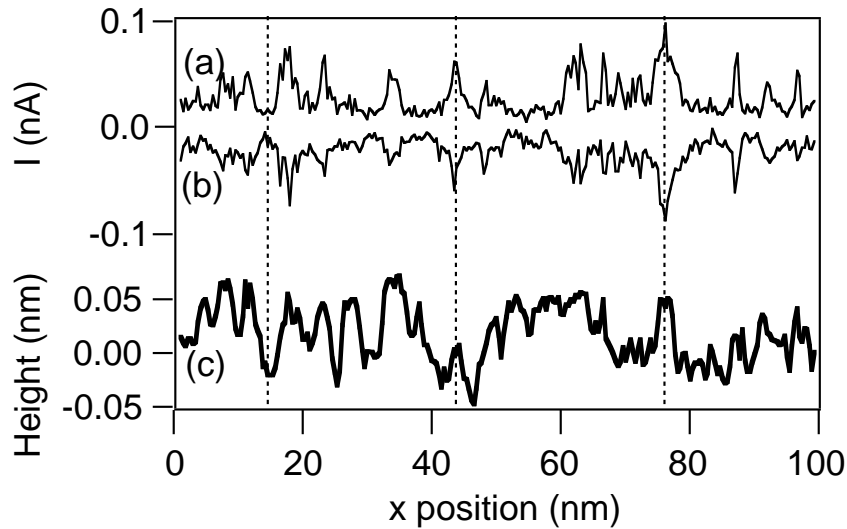
Figure 3.5: Line profiles taken in the current map images (a), (b) and topography image (c), in Fig. 3.4, at the positions marked by arrows.

constituents of the chemically disordered alloy. It means that the surface of Fe$_{50}$Mn$_{50}$ shows regions enriched in one or the other of the alloy components. A quantitative interpretation of STM/STS data presented in this section requires knowledge of the electronic surface states of sample and tip. Further experiments with surface sensitive techniques such as ultraviolet emission spectroscopy (UPS), or electron energy loss spectroscopy (EELS) must be applied for a full understanding.

3.2 The FeNi/Fe$_{50}$Mn$_{50}$/Co trilayer system

Using photoelectron emission microscopy (PEEM) combined with X-ray magnetic circular dichroism, the magnetic domain structure in coupled epitaxially grown FeNi/FeMn/Co/Cu(001) double wedge-shaped trilayers was investigated. The results have been backed up with magneto-optical Kerr effect measurements of Co/FeMn/Co/Cu(001) trilayers.

Figure 3.6 presents element resolved domain images obtained at the Co L_3 edge (left hand side) and the Fe L_3 edge (right hand side) of 6 ML FeNi deposited as a continuous film on a 20 ML Fe$_{50}$Mn$_{50}$/8 ML Co crossed double wedge on Cu(001). The Co thickness varies in the range of Fig. 3.6 from 3 to 8 ML from bottom to top, as indicated at the left axis, and stays constant with 8 ML above. The Fe$_{50}$Mn$_{50}$ thickness increases from 0 to 14 ML from left to right, as indicated at the bottom axis. Different gray scales correspond to different projections of the local magnetization direction onto the direction of the incoming light. The crystallographic axes and the direction of the light incidence are indicated by small arrows in the right upper,

respective left bottom part of each figure.

In the Co domain images different gray scale levels are recognized corresponding to domains of four different directions of magnetization. Analysis of the contrast reveals that for a thickness below 6 ML Fe$_{50}$Mn$_{50}$, the Co magnetization direction is pointing along $\langle 110 \rangle$ crystal axes, as indicated by arrows. Above 6 ML Fe$_{50}$Mn$_{50}$ thickness a change in the orientation of the magnetization direction of Co towards $\langle 100 \rangle$ is observed, as indicated by arrows. In the
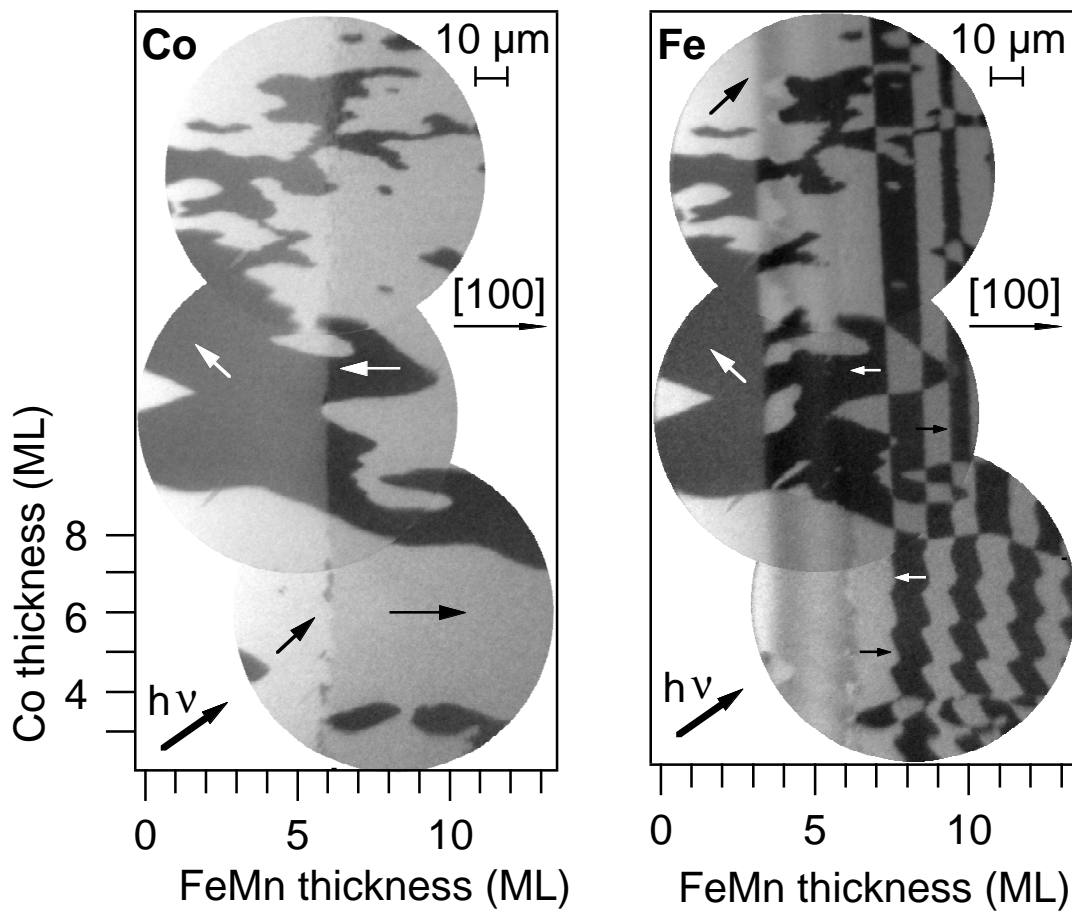
Figure 3.6: Layer-resolved domain images of Co (left) and Fe (right) of 6 ML FeNi/0–14 ML Fe$_{50}$Mn$_{50}$/3–8 ML Co grown epitaxially on Cu(001). Co and Fe$_{50}$Mn$_{50}$ thicknesses are indicated at the left and bottom axes of the images, respectively. The direction of the incoming X-rays (hν), crystallographic axes, and magnetization direction of some of the domains are indicated by arrows in each figure.

measurements of Kuch *et al.* a change in the easy axis of Co films on Cu(001) by 45° has been observed when in contact with antiferromagnetic FeMn films [15]. The change of the Co magnetization direction from $\langle 110 \rangle$ to $\langle 100 \rangle$ has been related to the transition from paramagnetism to antiferromagnetism of Fe$_{50}$Mn$_{50}$ films. In analogy to the fluctuation mechanism proposed by

Slonczewski, the above result has been explained by an effective 45° magnetic coupling of Co to Fe$_{50}$Mn$_{50}$. Therefore, in accord with these results, in this work it will be assumed that the change in the magnetization direction of Co is the result of the magnetic phase transition of Fe$_{50}$Mn$_{50}$ from paramagnetic to antiferromagnetic for a thickness of about 6 ML.

Inspection of the Fe domain image in Fig. 3.6, corresponding to the FeNi layer, shows that the leftmost one third of the image, for Fe$_{50}$Mn$_{50}$ thicknesses below 3 ML, exhibits an identical domain pattern as the Co image. The analysis of the different contrast levels reveals that for an Fe$_{50}$Mn$_{50}$ thickness below 3 ML the FeNi magnetization is aligned with the Co magnetization direction as shown by arrows. It has been reported previously by Offi *et al.* that when Fe$_{50}$Mn$_{50}$ is deposited on Co, below a thickness of about 3 ML, it becomes fully ferromagnetic by the proximity to the ferromagnetic Co layer [81]. This ferromagnetic phase leads to a direct exchange coupling between the Co and FeNi layers. The stronger in-plane anisotropy of Co compared to the FeNi anisotropy probably aligns the FeNi magnetization into the same direction as the Co magnetization.

Above 3 ML Fe$_{50}$Mn$_{50}$ thickness an undulation of the magnetization direction of FeNi between the $\langle 110 \rangle$ and $\langle 100 \rangle$ crystallographic axis is observed as a continuously changing contrast in the FeNi image between 3 and 6 ML FeMn thickness. A continuous change in the contrast from bright to light dark and then to light bright is seen when following the bright stripe-like domain in the Fe image from left to right. In this thickness range the FeNi magnetization is non-collinearly aligned to the Co magnetization. The fourfold in-plane anisotropy of the 6 ML FeNi favors the orientation of the FeNi magnetization along the $\langle 100 \rangle$ directions. The interlayer magnetic coupling tries to align the FeNi magnetization along the same direction with the Co magnetization. The competition between these two terms, anisotropy energy of the FeNi and interlayer magnetic coupling energy, leads to a canted configuration.

Increasing the Fe$_{50}$Mn$_{50}$ thickness beyond 6 ML, a periodic oscillatory changing of the contrast of the Fe domain image with a period of 2 ML Fe$_{50}$Mn$_{50}$ thickness is observed. Analysis of the gray scale of the Fe image shows that in this region FeNi and Co magnetizations are either parallel or antiparallel along $\langle 100 \rangle$ directions. These oscillations are consistent with layer-by-layer thickness dependent reversals in the orientation of the magnetization of the top FeNi layer, implying that the Fe$_{50}$Mn$_{50}$ layers are antiferromagnetically ordered.

Besides the magnetization oscillations with a 2 ML period of the Fe$_{50}$Mn$_{50}$, additional magnetization changes are observed in the bottom part of the FeNi domain image, Fig. 3.6. A closer look into these stripe-like domains reveals a ripple-like periodic modulation of the coupling phase with a period of 1 ML as a function of Co thickness. On the Co plateau no such undulation of the stripes is seen. This may indicate that for the layer-by-layer growth of Co the change of the roughness when going from a filled atomic layer to a half filled layer induces such a ripple-like modulation of the phase of the coupling. In the last chapter of this thesis a comprehensive discussion will be dedicated to this subject.

The as-grown PEEM magnetic domain images give information about the direction of the magnetization. They do not lead to a value of the strength of the coupling. The strength of the interlayer exchange coupling, i.e., the coupling energy per unit area, can be determined by applying a varying magnetic field to the trilayer structure and measuring the magnetization curves by conventional magnetometry. Such magnetization measurements have been obtained using magneto-optic Kerr effect (MOKE) at room temperature. The MOKE measurements have been performed on Co/Fe$_{50}$Mn$_{50}$/Co trilayers deposited on Cu(001). The Fe$_{50}$Mn$_{50}$ was deposited as a wedge-shaped layer of linearly increasing thickness by moving the sample in front of a shutter during deposition. Here, I underline that the LMOKE measurements have been performed in a second UHV system (MBE-machine) described in Sec. 2.3. Fig. 3.7 (a) shows hysteresis loops of 8 ML Co/Cu(001) (the narrow loop) and a 13 ML Fe$_{50}$Mn$_{50}$/8 ML Co bilayer on Cu(001). The external applied field was aligned along the $\langle 100 \rangle$ crystal axes (the magnetic easy axis (EA) of the Fe$_{50}$Mn$_{50}$/Co/Cu(001) system). Note a significantly enhanced coercivity in the coupled film ($H_c^{FeMn/Co} = 33.7$ mT) which is roughly 56 times the coercivity of the single Co layer ($H_c^{Co} = 0.6$ mT) [82, 83]. Figure 3.7 (b) illustrates a typical hysteresis loop, measured in the LMOKE geometry with s-polarization, corresponding to FM coupling between the Co layers. A kink in the loop is seen when we follow the loop from zero value of the magnetic field towards negative values. The kink feature could be associated with the switching of one layer (most likely the upper one), or with 90° orientation of the Co layers. To get more insight into the origin of this kink I have measured MOKE in the longitudinal geometry but with p-polarization. In this case besides the longitudinal component of the magnetization the Kerr signal is also sensitive to the transversal component. Fig. 3.7 (d) shows the MOKE loop measured in the longitudinal geometry with p-polarization, at the same position of the sample. When the external magnetic field is reduced from positive saturation towards zero and then to negative values, an increase (jump) of the Kerr signal can be seen, followed by a plateau and a decrease towards negative saturation. This peak from Fig. 3.7 (d) is located at exactly the same position as the kink in Fig. 3.7 (b). For the reason that the longitudinal component of the Kerr signal has to be monotonic, the peak in Fig. 3.7 (d) must be due to a transverse component.

Since the magnetization reversal is accomplished by an increase of the Kerr signal (Fig. 3.7 (d)) I propose that the kink feature observed in Fig. 3.7 (b) is due to rotation, together, of both layers, to a direction orthogonal to the external magnetic field. The metal films are thin enough so that the Kerr signal is sensitive to both FM layers. An independent rotation of the Co layers would give rise to a second kink in the hysteresis loop of Fig. 3.7 (d), which has not been observed. In other words, the magnetization reversal occurs in two distinct stages: first, by a switching by 90° followed by a second switching towards a direction parallel with the applied magnetic field. Hence, the "shelflike" feature seen in Fig. 3.7 (b) near zero Kerr signal corresponds to the range of fields for which the magnetization vectors are in an intermediate state at $\approx 90°$ to the external magnetic field direction. A closer inspection of the hysteresis loop in Fig. 3.7 (b) reveals
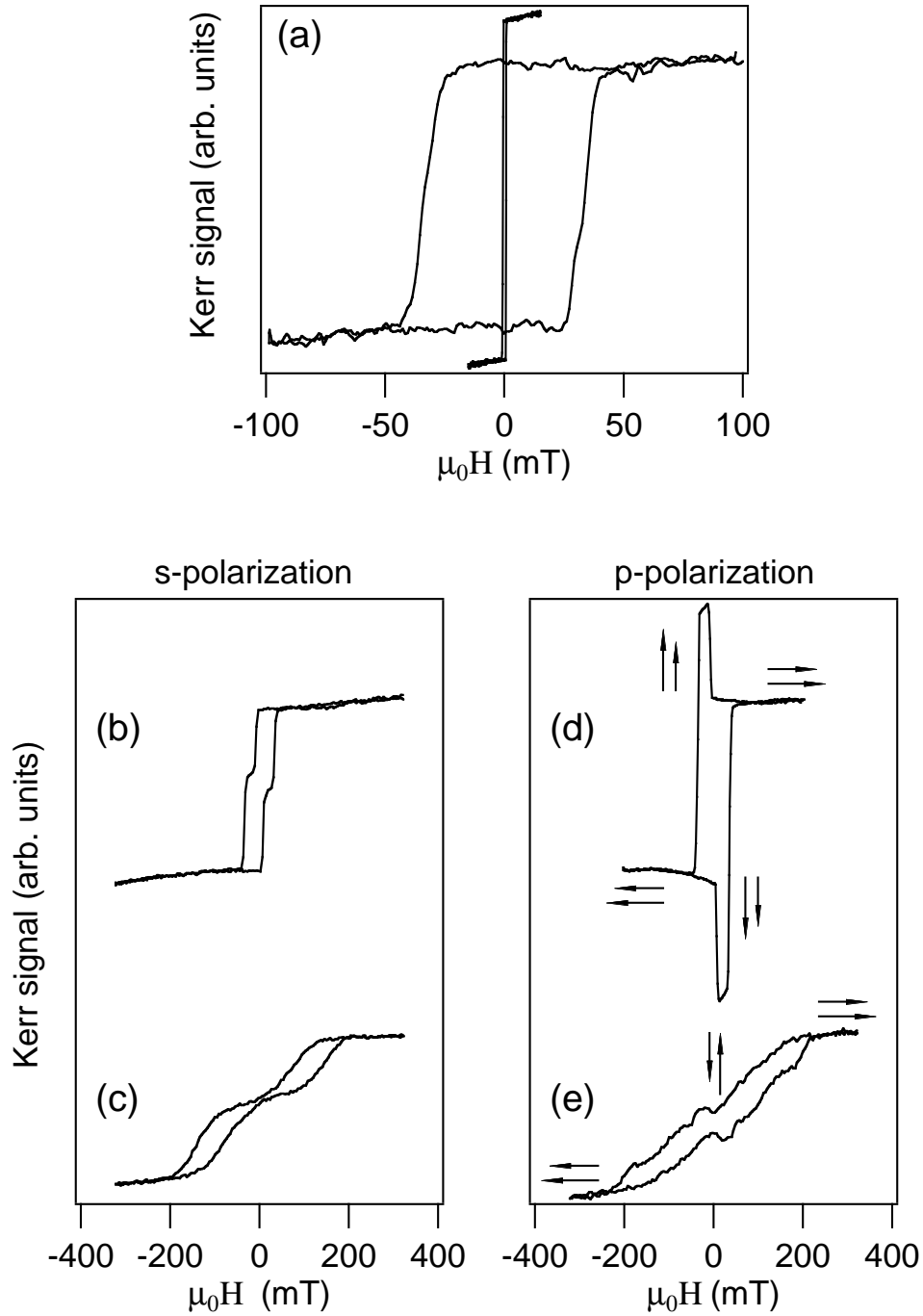
Figure 3.7: LMOKE hysteresis loops measured along the $\langle 100 \rangle$ crystal axes at RT of: (a) shows two curves corresponding to 8 ML Co/Cu(001) and 13 ML Fe$_{50}$Mn$_{50}$/8 ML Co/Cu(001), respectively. The narrow loop in panel (a) corresponds to 8 ML Co/Cu(001); (b) 6 ML Co/13 ML Fe$_{50}$Mn$_{50}$/8 ML Co measured with s–polarization of the incident beam; (c) 6 ML Co/14 ML Fe$_{50}$Mn$_{50}$/8 ML Co with s–polarization of the incident beam; (d) 6 ML Co/13 ML Fe$_{50}$Mn$_{50}$/8 ML Co with p–polarization of the incident beam; (e) 6 ML Co/14 ML Fe$_{50}$Mn$_{50}$/8 ML Co with p–polarization of the incident beam.

that the "shelflike" features on the positive and negative branches are slightly vertically shifted towards each other. In addition the height of the upper and lower peaks seen in Fig. 3.7 (d) is slightly different. These observations reflect a small misalignment ($\approx 5°$) of the crystallographic [100] axis with the longitudinal measurement direction.

In Fig. 3.7 (c) and (e) are shown hysteresis loops measured in the region of AFM coupling in between the Co layers, $t_{FeMn} = 14$ ML. For large external fields the interlayer coupling is overcome, and the layers are parallel to the field. As the field is reduced, the interlayer coupling exceeds the Zeeman energy and the thicker FM layer starts to reverse. In the remanent state both layers are oriented antiparallel (in a direction orthogonal to the external applied field direction). When the external magnetic field is increased from zero to either positive or negative values, a slight increase (decrease) of the Kerr signal is observed for the measurement with p–polarized light (Fig. 3.7 (e)). It corresponds to the rotation starting point of one FM layer while the second one is fixed.
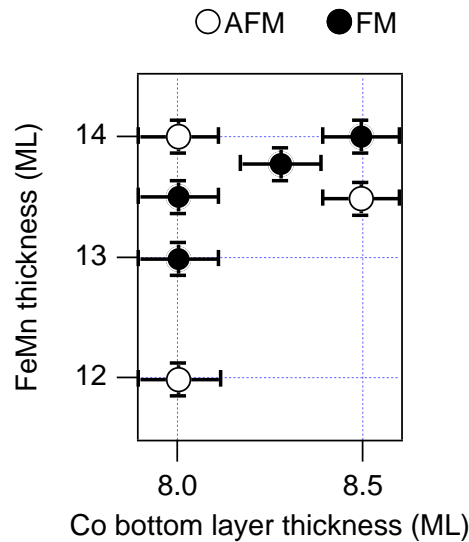
Figure 3.8: Map of the interlayer magnetic coupling of Co/Fe$_{50}$Mn$_{50}$/Co trilayers deposited as continuous films on Cu(001). The black (white) bullets denote a FM (AFM) interlayer coupling, as measured with MOKE. The errors of the thickness estimation are attached to each bullets as vertical (horizontal) bars.

In addition MOKE measurements on Co/Fe$_{50}$Mn$_{50}$/Co trilayers, deposited as continuous films, were carried out. The thicknesses of the Co bottom layer and Fe$_{50}$Mn$_{50}$ were changed in the submonolayer range. Fig. 3.8 presents a cumulative map of these MOKE measurements. The white (black) bullets are associated with antiferromagnetic (ferromagnetic) coupling in between the FM Co layers. It does not contain any information on the strength of the coupling. The Co bottom layer thickness varies from 8 to 8.5 ML, as indicated at the bottom axis, and the Fe$_{50}$Mn$_{50}$ thickness from 12 to 14 ML as indicated at the left axis. The thickness of the Co top

layer is maintained constant at 6 ML for all measurements. For a thickness of the Co bottom layer of 8 ML, and 13.5 ML Fe$_{50}$Mn$_{50}$, the interlayer coupling between the two Co layers is ferromagnetic (FM), as seen also in Fig. 3.7. Increasing the Fe$_{50}$Mn$_{50}$ thickness to 14 ML while maintaining the Co bottom layer constant, the interlayer coupling changes to antiferromagnetic (AFM). For a Co bottom layer thickness of 8.5 ML, and an Fe$_{50}$Mn$_{50}$ thickness of 14 ML, the interlayer coupling is FM. Hence, a change of the Co bottom layer thickness of 0.5 ML induces a change of the coupling from AFM to FM.
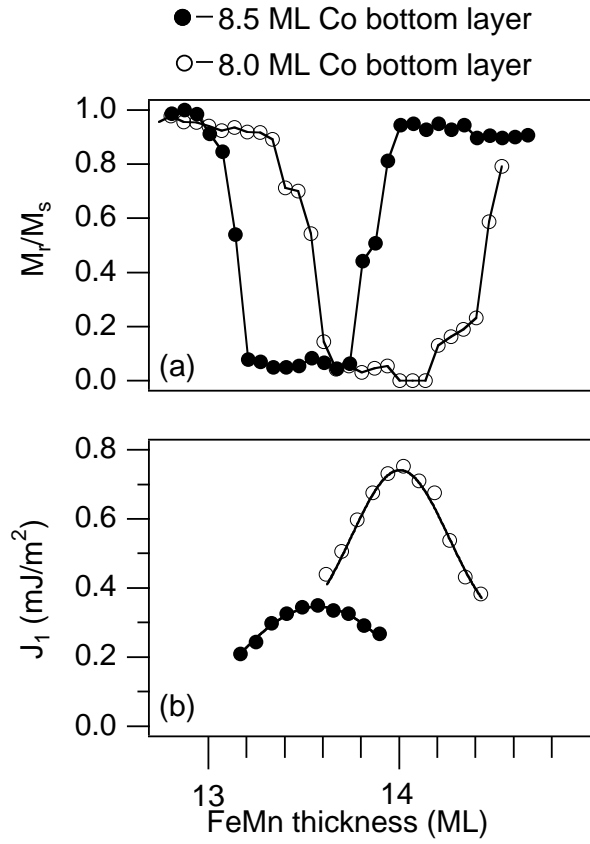
Figure 3.9: (a) Dependence of the remanence magnetization (M$_r$) normalized to the saturation magnetization (M$_s$) as a function of the Fe$_{50}$Mn$_{50}$ spacer layer estimated from LMOKE measurements of Co/Fe$_{50}$Mn$_{50}$/ Co trilayer on Cu(001). The Fe$_{50}$Mn$_{50}$ spacer layer was deposited as a wedge within a thickness range of 13–14.8 ML. The Co bottom layer thickness was 8.0 and 8.5 ML, respectively, while the Co top layer was similar for the both measurements, 6 ML. (b) Coupling strength (J$_1$) of the same sample as in the case (a) as a function of Fe$_{50}$Mn$_{50}$ thickness calculated using eq. 3.1 and the experimental estimated H_S values.

Fig. 3.9 (a) shows the dependence of the remanent magnetization (M$_r$) normalized to the saturation magnetization (M$_s$) as a function of Fe$_{50}$Mn$_{50}$ thickness for two different coverages of

the Co bottom layer, 8.0 ML and 8.5 ML, respectively. The top layer is a 6 ML Co continuous film in both cases. The Fe$_{50}$Mn$_{50}$ layer was prepared as a 13 ML continuous film followed by the deposition of 2 ML on top as a wedge. Let us first discuss the case of 8.0 ML Co bottom layer thickness (open bullets). Going from 13 ML to 14 ML Fe$_{50}$Mn$_{50}$ thickness the normalized remanence magnetization changes from unity to nearly zero. This corresponds to a change of the type of the coupling from FM ($M_r = 1$) to AFM ($M_r = 0$) between the Co layers. Above 14.2 ML Fe$_{50}$Mn$_{50}$ the value of remanence magnetization rises up again. Now, for the case of 8.5 ML Co bottom layer thickness, $M_r/M_s \simeq 1$ at 13 ML Fe$_{50}$Mn$_{50}$ and decreases to $M_r/M_s \simeq 0$ at only 13.4 ML Fe$_{50}$Mn$_{50}$ and increases again to $M_r/M_s \simeq 1$ at 14 ML Fe$_{50}$Mn$_{50}$ thickness. Comparing the graphs for the two cases, the $M_r/M_s \simeq 0$ region for 8.0 ML Co bottom layer appears wider than for 8.5 ML Co bottom layer thickness. Since the data reproduce the experimental results measured on two different samples, prepared in the same conditions, a slight change of the evaporation rate during wedge deposition can induce a change of the slope of the wedge. In Fig. 3.9 the errors of the Fe$_{50}$Mn$_{50}$ thickness estimation are within 0.2 ML.

It is possible to determine the coupling constant J_1 and the equilibrium angles between the FM layers by numerically fitting the MOKE curves following the path of minimum energy as the external magnetic field H is varied [84]. As an alternative in simple systems, some features may be determined analytically. Neglecting the anisotropy of the films, the following explicit relation between J_1 and H_S, the field at which both layers switch from antiparallel to parallel, can be written:

$$H_s = -\frac{J_1}{t_1 M_1 + t_2 M_2} \tag{3.1}$$

where J_1 is the total bilinear coupling strength and M_1, M_2 are the saturation magnetizations of layers 1 and 2 with thicknesses t_1 and t_2. For the numerical evaluation of J_1, literature values were chosen for the saturation magnetization of Co/Cu(001) estimated to be about 1.789 T in Ref. [85] and interplanar spacing distance for Co/Cu(001) to be about 1.774 Å in Ref. [86]. The coupling strength values J_1 calculated as described above are plotted in Fig. 3.9 (b) as a function of Fe$_{50}$Mn$_{50}$ thickness. The change of the Co bottom layer thickness from 8.0 ML to 8.5 ML, for the same Fe$_{50}$Mn$_{50}$ thickness, decreases the interlayer coupling strength by nearly 50% from 0.75 mJ/m^2 to 0.33 mJ/m^2.

Without going into details and possible mechanisms in this section, the phase and the strength of coupling of single crystalline films was seen to be strongly dependent on the sub-monolayer coverage of the bottom FM layer. In the last chapter of the thesis dedicated to the discussion I will give a qualitative model, and discuss and compare the coupling energy values determined here with the coupling measured in other systems.

3.3   The Ni/Fe$_{50}$Mn$_{50}$/Co trilayer system

This section presents a layer-resolved photoelectron emission microscopy (PEEM) study of the interlayer coupling in Ni/Fe$_{50}$Mn$_{50}$/Co trilayers, epitaxially grown on Cu(001). Epitaxial Co and Ni films on Cu(001) exhibit different magnetic easy axes. Whereas Co films are always magnetized in the film plane, Ni films show a spin reorientation transition from an easy axis parallel to the film plane at film thicknesses below 8 ML to an easy axis perpendicular to the film plane at thickness between 8 ML to 56 ML [89, 90, 91]. For a trilayer in the absence of interlayer coupling, the magnetic easy axes in each magnetic layer are defined by separate minimization of the anisotropy energy. In the case of a strong interlayer coupling, both magnetizations are forced to be collinear, whereas for weak coupling the individual magnetization directions will be along their own easy axes. Reorientation transitions between these two situations can occur for intermediate values of the coupling strength [93]. The coupling across Fe$_{50}$Mn$_{50}$ between Co with an in-plane easy axis and Ni with an out-of-plane easy axis will be addressed in this section.

Fig. 3.10 shows element selective domain images obtained at the Co L_3 edge (left) and at the Ni L_3 edge (right) of 15 ML Ni deposited as a continuous film on an Fe$_{50}$Mn$_{50}$/Co crossed double wedge on Cu(001) as a substrate. The Co thickness varies in the range of Fig. 3.10 from 3 to 8 ML from bottom to top, as indicated at the left axis, and the Fe$_{50}$Mn$_{50}$ thickness from 0 to 14 ML from left to right, as indicated at the bottom axis. The crystallographic axes and the direction of incoming light are indicated in the right upper and left bottom part of each panel, respectively. The Co image shows relatively large magnetic domains. When following the image from left to the right, a change in the gray scale contrast at about 7 ML Fe$_{50}$Mn$_{50}$ is observed. It reflects a change of the direction of magnetization of Co from [$\bar{1}\bar{1}0$] towards [$0\bar{1}0$] above 7 ML Fe$_{50}$Mn$_{50}$. As has been discussed in the previous section, this change in the easy axis of Co after deposition of Fe$_{50}$Mn$_{50}$ reflects a phase transition from paramagnetism to antiferromagnetism of Fe$_{50}$Mn$_{50}$.

Inspection of the Ni image of Fig. 3.10 (right) reveals an identical domain pattern as the Co image for an Fe$_{50}$Mn$_{50}$ thickness below 3 ML. In this area the Ni magnetization is in-plane, aligned with the Co magnetization direction. A reorientation of the Ni magnetization direction from in-plane to nearly out-of-plane starts at about 3 ML Fe$_{50}$Mn$_{50}$.

Within the thickness range 3 to 7 ML Fe$_{50}$Mn$_{50}$ can be seen. A closer look to the dark stripe-like domain at around 5 ML Fe$_{50}$Mn$_{50}$ thickness reveals a continuous change of the contrast from light gray at the edge to darker in the middle of the stripe. This can be explained by a gradual canting of the Ni magnetization direction as a function of Fe$_{50}$Mn$_{50}$ thickness, probably due to RKKY-like interlayer coupling across the paramagnetic Fe$_{50}$Mn$_{50}$ layer as in previous section.

Now, let us follow the Ni image, Fig. 3.10, as a function of the Co bottom layer thickness.
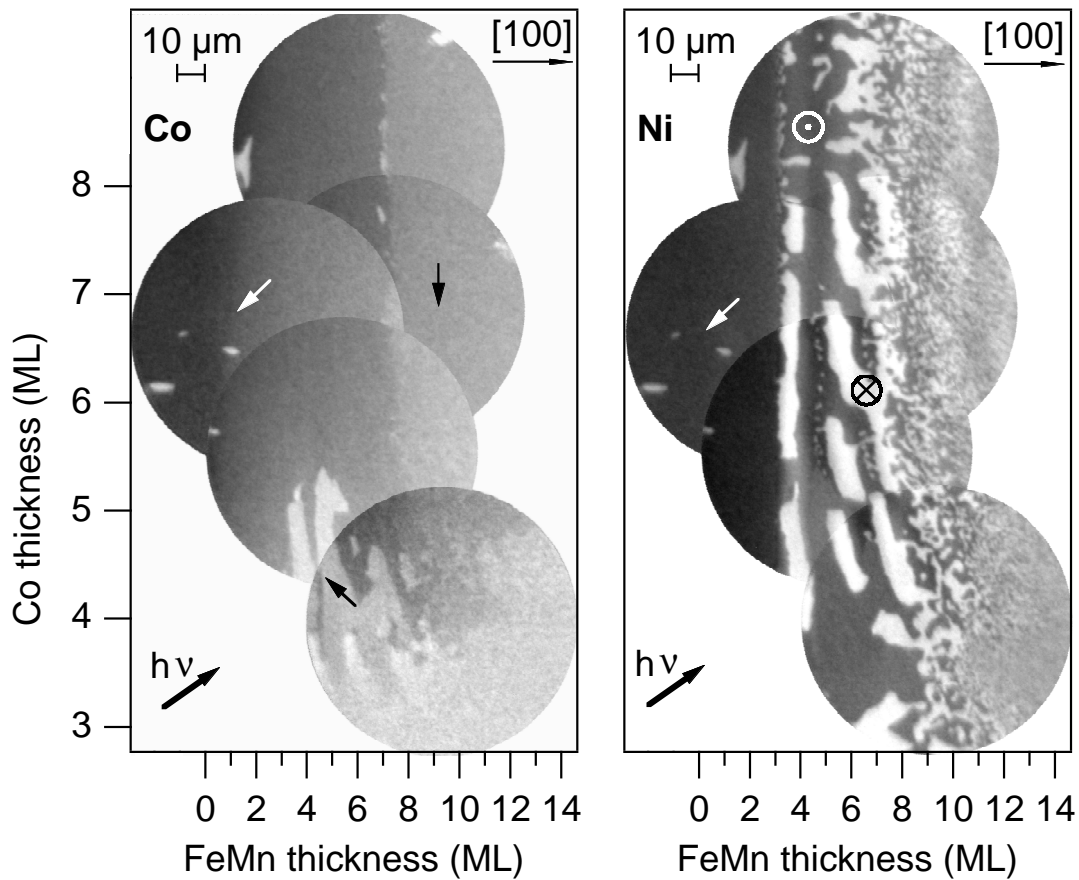
Figure 3.10: Layer-resolved magnetic domain images of a 15 ML Ni/0–14 ML $Fe_{50}Mn_{50}$/3–8 ML Co trilayer on Cu(001). A map of domain images of the Co bottom layer is shown on the left hand side, the map of domain images of the Ni top layer on the right hand side. A change of the Co magnetization direction and of the Ni domain structure are observed when the $Fe_{50}Mn_{50}$ thickness displayed at the bottom axes is changed. The local magnetization directions are indicated in some domains.

An oscillating behavior when looking to the white stripes of the Ni domain image at 6 ML $Fe_{50}Mn_{50}$, from bottom to top of the image, is observed. For a fixed $Fe_{50}Mn_{50}$ thickness, increasing (decreasing) the Co thickness by less than one monolayer changes the direction of the Ni magnetization from pointing "up" to pointing "down". A quite interesting observation is that these oscillatory stripes are present only on the Co wedge, and just above 4 ML Co. On the Co plateau, the upper part of the Ni image, domains of an irregular shape, with an out-of-plane magnetization can be seen. The 1 ML Co bottom layer thickness periodicity of these stripes, and the presence only on the wedge, may indicate a connection with the interface roughness.

There must be a mechanism that leads to a correlation between the as-grown out-of-plane magnetization direction of the Ni layer and the in-plane direction of the underlying Co layer.

Oscillations of the direction of the out-of-plane magnetization could consequently also be related to oscillations of the sign of the interlayer coupling. These could be seen as a clear indication that either the coupling or this mechanism has to do with the roughness of the Co–Fe$_{50}$Mn$_{50}$ interface.

Kuch *et al.* have found a correlation between the Ni out-of-plane domains and the Co in-plane domains, in Co/Cu/Ni trilayer system. The Co magnetic domains show different directions of magnetization on top of "up" or "down" Ni domains [92]. However, in Fig. 3.10, the Co bottom layer show a single domain within the white stripes in Ni top layer.

In the Co image the change of the magnetization direction from [$\bar{1}\bar{1}0$] to [$0\bar{1}0$], as mentioned above, is seen for an Fe$_{50}$Mn$_{50}$ thickness of 7 ML, exactly the same thickness where the small domains in the Ni layer appear. This thickness thus corresponds to a change of Fe$_{50}$Mn$_{50}$ from paramagnetic to antiferromagnetic at room temperature. Similar observations were made by Kuch *et al.* in the as-grown Co on Fe$_{50}$Mn$_{50}$ wedge on Cu(001) [15] in this system. Above 10 ML Fe$_{50}$Mn$_{50}$ small magnetic domains are formed in the Co layer. The 10 ML corresponds to the thickness of ordering transition at room temperature of the antiferromagnetic Fe$_{50}$Mn$_{50}$. Local exchange interaction between Co and Fe$_{50}$Mn$_{50}$ induces a replicate domain pattern of the Fe$_{50}$Mn$_{50}$ domains in the Co as-grown layer. Heating the sample above the Néel temperature of Fe$_{50}$Mn$_{50}$ promotes larger domains in the Co layer. This may be an indication that the presence of small domains in the as-grown state of a FM layer deposited on top of an AFM layer is related to the local exchange interaction FM/AFM
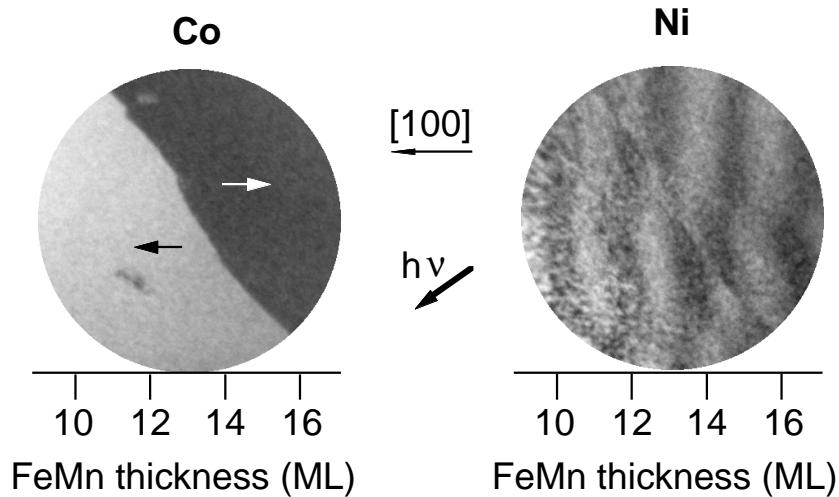
Figure 3.11: Layer-resolved magnetic domain images of a 15 ML Ni/9.8–16.2 ML Fe$_{50}$Mn$_{50}$/8 ML Co trilayer on Cu(001). The domain image of the Co layer is shown on the left hand side, the domain image of the Ni layer on the right hand side. The change of the Co magnetization direction is replicated in the Ni faint stripes domain pattern, superimposed on a domain pattern of small domains.

On the upper right part of the Ni image (Fig. 3.10), above 7 ML Fe$_{50}$Mn$_{50}$ one can see that faint stripes are superimposed onto small domains with magnetization pointing up or down. The faint stripes are seen better in Fig. 3.11, which shows domain images obtained at the Co L_3 edge (left) and Ni L_3 edge (right) at a different position of the same sample. The Fe$_{50}$Mn$_{50}$ thickness varies here from 9.8 ML to 16.2 ML. The Co image shows domains of different gray scale corresponding to two different magnetization directions as labelled by arrows. Following one of the stripes in the Ni image from bottom to the top of the image a jump of the stripe contrast is seen. It corresponds to a change of magnetization direction of Co along the diagonal of the image. While the Co/Fe$_{50}$Mn$_{50}$ and Ni/Fe$_{50}$Mn$_{50}$ type of interface coupling is always the same, either FM or AFM, for a certain Fe$_{50}$Mn$_{50}$ thickness, a change of the Co bottom layer magnetization induces a change of the upper Ni layer magnetization. The stripes are thus interpreted as a canting of the Ni magnetization direction away from pure out-of-plane directions by an oscillatory coupling to the Co layer across the AFM Fe$_{50}$Mn$_{50}$ with 2 ML period.

From the above results, it can be concluded that the Ni layer experiences two effect from the underlying Fe$_{50}$Mn$_{50}$/Co bilayer: one is a spatially fluctuating pinning of the out-of-plane component of magnetization, leading to the occurrence of the small out-of-plane domains, the other is an oscillatory coupling of the in-plane component of magnetization, which leads to a periodic canting of the Ni magnetization into directions parallel and antiparallel to the Co magnetization. An in-plane spin component in Fe$_{50}$Mn$_{50}$ which changes direction with each additional layer, pinned to the Co layer, can be responsible for the 2 ML Fe$_{50}$Mn$_{50}$ thickness periodic canting of the Ni magnetization direction. In addition, the antiferromagnetism of the Fe$_{50}$Mn$_{50}$ layers leads to the occurrence of small domains in the out-of-plane component of the top Ni layer.

In the following, the question of the origin of these small domains in the Ni image with stripes superimposed, was tested in another experiment. In a previous study it has been shown that deposition of 3 ML Co on 15 ML Ni induces a spin reorientation transition of the Ni magnetization from out-of-plane to in-plane [93]. Based on these previous experimental observations, the study of these small domains is addressed by depositing 3 ML Co on top of Ni/Fe$_{50}$Mn$_{50}$/Co trilayer. Fig. 3.12 shows domain images obtained at the Co L_3 edge (left) and the Ni L_3 edge (right) after deposition of 3 ML Co. The directions of crystallographic axes and incoming light are indicated at the left side of each image. The Co signal "seen" in this case is a superposition of the signal coming from the top 3 ML and from the bottom Co layer. This can be clearly recognized in the top image of the Co image map, Fig. 3.12. The stripes in the Co appear with a different contrast below and above a diagonal of the top Co image, from bottom right to the upper left. Stripes in the left bottom part show two different gray level: dark and bright. In the upper right part stripes appear heavy dark and light gray. These different contrast levels seen in the upper right and bottom left part of the top Co image must not be associated with other directions of magnetization of the top layer than along the [100] and [$\bar{1}$00] axes, but appear due
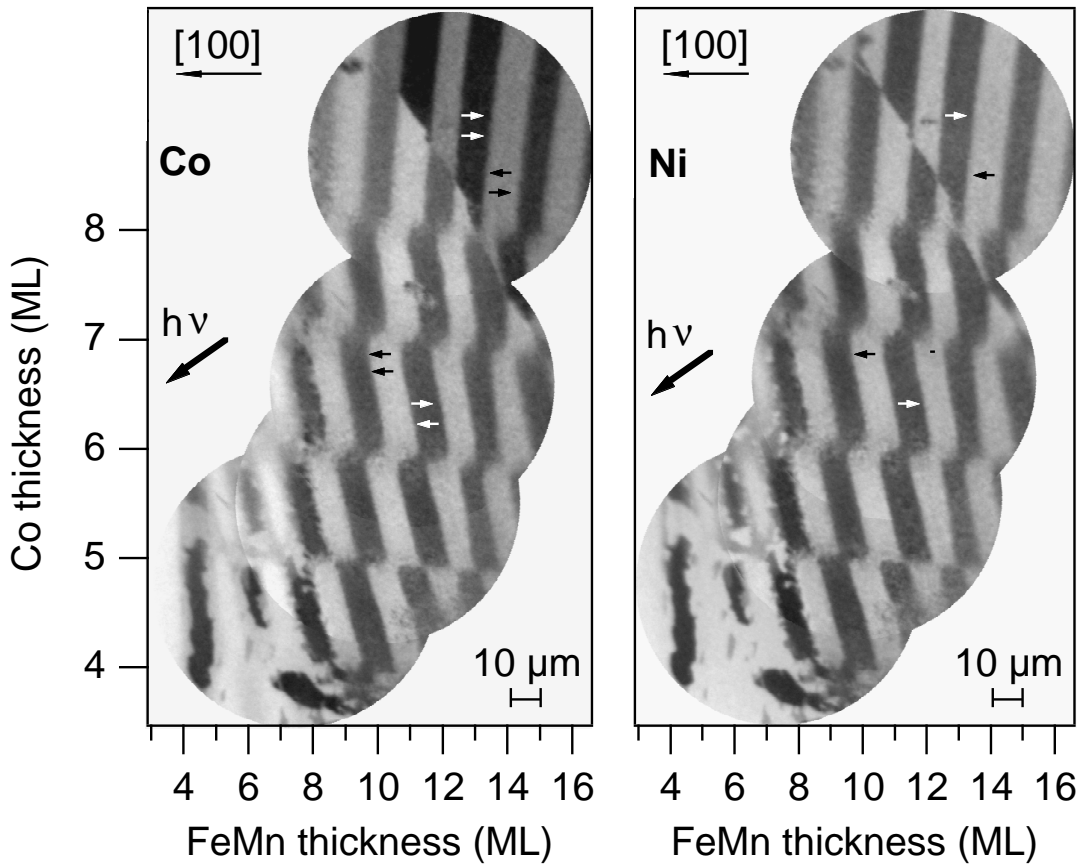
Figure 3.12: Layer-resolved magnetic domain images of a 3 ML Co/15 ML Ni/3–16 ML FeMn/3–8 ML Co trilayer on Cu(001). A map of Co domain images is shown on the left hand side, the map of the Ni domain images on the right hand side. The Co and Ni magnetizations are in-plane collinear aligned. Arrows in the Co image correspond to magnetization direction of the top and bottom layers.

to the above mentioned averaging of the signal measured at the Co L_3 edge along the thickness of the layers. In the upper right part of the image, the same region as in Fig. 3.11, the magnetization of the Co bottom layer is pointing along [$\bar{1}$00] and appears with a dark contrast. In the bottom part of the Co image, the magnetization of the Co bottom layer is oriented along [100], and appears brighter. The magnetization of the top Co layer oscillates with 2 ML Fe$_{50}$Mn$_{50}$ thickness, from [100] to [$\bar{1}$00], showing bright and dark contrast. The white/dark contrast of the bottom Co layer adds to the contrast at the Co L_3 edge giving rise to intermediate gray levels contrast on different sides of the image. Following one of the vertical white stripes in Co, from lower to upper side, a change of the contrast from white to heavy dark is seen. For a certain Fe$_{50}$Mn$_{50}$ thickness, the interlayer coupling between the bottom and top Co layers is either FM or AFM. A change of the direction of magnetization of the Co bottom layer will induce a change

of the magnetization direction of the Co top layer, while the type of coupling is maintained.

Inspection of the contrast of the Ni image shows that the deposition of 3 ML Co induces indeed a spin-reorientation-transition of the Ni from canted out-of-plane to in-plane. A periodic oscillatory stripe domain pattern with 2 ML period as a function of Fe$_{50}$Mn$_{50}$ thickness is observed when following the Ni image from left to the right, Fig. 3.12. Since the Co bottom layer is presumably in single domain in most of the range of the images and just changes magnetization direction at the domain boundary at the top of the images, this indicates an oscillating coupling with the Fe$_{50}$Mn$_{50}$ thickness. The out-of-plane small domains observed in the as-grown state in Ni above 7 ML Fe$_{50}$Mn$_{50}$ have disappeared. Analysis of the contrast reveals that the magnetization in these stripes is indeed parallel and antiparallel to the magnetization of the Co bottom layer.

Now, when following the Ni image from lower to the upper side it can be seen that the phase of coupling is periodically modulated as a function of the Co bottom layer thickness. Actually, this is similar to the step-wise character observed in the Fe$_{50}$Mn$_{50}$ thickness region of 5 up to 12 ML in Fig. 3.10 and in Fig. 3.6.

Analysis of the Ni image, Fig. 3.12, reveals a correlation of the magnetic domain structure with the one of Co. Morever, above 7 ML Fe$_{50}$Mn$_{50}$, over the entire image a periodic oscillatory coupling with 2 ML Fe$_{50}$Mn$_{50}$ is observed in the Ni and top Co layer. A slightly different domain pattern is seen below 7 ML Fe$_{50}$Mn$_{50}$, the left bottom side of the each image, Co and Ni, respectively. In spite of stripes of 1 ML Fe$_{50}$Mn$_{50}$ thickness width, domains with a less defined shape appear. Looking backward to Fig. 3.10, 7 ML Fe$_{50}$Mn$_{50}$ is the thickness where the small domains appear in Ni, and the Fe$_{50}$Mn$_{50}$ changes from paramagnetic to antiferromagnetic. It is the same thickness of Fe$_{50}$Mn$_{50}$ where a transition from a 2 ML Fe$_{50}$Mn$_{50}$ oscillatory coupling to a less ordered domain structure is seen in Fig. 3.12.

The period of all oscillations is determined with a relative error of about $\pm 10\%$. Whereas $\pm 10\%$ of the absolute thickness prohibits any statements about the absolute phase of the oscillations.

The periodical oscillation within the monolayer range of the Fe$_{50}$Mn$_{50}$ thickness suggests a correlation with the antiferromagnetic structure of the Fe$_{50}$Mn$_{50}$. The canting of Ni within the small domains grouped in stripes is governed by the direct coupling to the Fe$_{50}$Mn$_{50}$ layer. A non-collinear spin structure of Fe$_{50}$Mn$_{50}$, at least when sandwiched between Co and Ni layers, may explain the above experimental observations. This will be discussed in Sec. 5.4. The out-of-plane spin component is reflected in the presence of the out-of-plane small domains in Ni top layer, while the in-plane spin component gives rise to 2 ML Fe$_{50}$Mn$_{50}$ thickness in-plane oscillatory coupling as evidenced by the superimposed stripes. One question that rises up in this moment is whether the non-collinear spin structure of Fe$_{50}$Mn$_{50}$ is an intrinsic property or just a particular case, when sandwiched in-between Co and Ni layers. The in-plane spin component may be favored by the exchange coupling to the in-plane magnetization of the Co layer, while an

out-of-plane spin component by the exchange coupling to the out-of-plane magnetized Ni layer. In order to answer to this question, in the next section, the Fe$_{50}$Mn$_{50}$ is sandwiched between two Ni layers with an out-of-plane direction of magnetization.

3.4 The Ni/Fe$_{50}$Mn$_{50}$/Ni trilayer system

In this section the coupling between two FM Ni layers across Fe$_{50}$Mn$_{50}$ is addressed. An epitaxial Ni/Fe$_{50}$Mn$_{50}$/Ni trilayer has been prepared on Cu(001), in which both the Fe$_{50}$Mn$_{50}$ and the bottom Ni layer were deposited as a crossed double wedge, rotated in the film plane by 90° with respect to each other, and the top layer was a continuous film of 15 ML Ni. As has been described in the previous section, epitaxial Ni films grown on Cu(001), above 8–10 ML, show an easy axis perpendicular to the film plane.

After deposition of the first Ni layer, an external magnetic field ($\approx$ 500 Oe) in a direction perpendicular to the sample surface has been applied. This is sufficient to magnetize in saturation the bottom Ni layer, removing any internal domain structure. As discussed also in the previous section, the signal measured at the Ni L_3 edge contains information of both, the upper and bottom Ni layers. However, the signal attenuation by overlayers has an exponential decay as a function of the overlayer thickness. For example, in the case of Ni buried by 20 ML Fe$_{50}$Mn$_{50}$, the total electron yield measured at the Ni L_3 edge that reaches the surface is about 16% compared to that of the uncapped Ni layer [53]. In the light of the above discussion, it can be concluded that any domain structure seen in the Ni/Fe$_{50}$Mn$_{50}$/Ni trilayer at the Ni L_3 edge reflects only the magnetic structure of the upper Ni layer.

Fig. 3.13 shows the domain image obtained at the Ni L_3 edge. The thickness of the bottom Ni layer varies in the range of Fig. 3.13 from 0 to 15 ML, from bottom to top, as indicated at the left axis, and the Fe$_{50}$Mn$_{50}$ thickness from 0 to 15 ML from left to right, as indicated at the bottom axis. The small arrow at the left bottom corner indicates the direction of incoming light.

Different regions as a function of the bottom Ni layer and Fe$_{50}$Mn$_{50}$ spacer layer thicknesses can be distinguished. Now let us focus on the lower part of the image, below 8 ML Ni. Small irregular domains with an average size depending on the Fe$_{50}$Mn$_{50}$ thickness can be observed. Between 0–3 ML Fe$_{50}$Mn$_{50}$ a dark stripe is formed in Ni. Above 3 ML Fe$_{50}$Mn$_{50}$ a white stripe with some very small dark domains is seen. Within 7–17 ML Fe$_{50}$Mn$_{50}$ relatively larger domains appear in Ni. Regarded as a function of the Ni bottom layer thickness these appear elongated along the Ni wedge, with lateral dimensions decreasing with increasing Ni thickness. Within this thickness range, the Ni bottom layer is either in a paramagnetic or ferromagnetic state with magnetization oriented in-plane. Above 17 ML Fe$_{50}$Mn$_{50}$, in the most down-right part of the image, small domains magnetized out-of-plane are formed in Ni top layer. Since there is no Ni bottom layer in this region, the small domains are formed in the top Ni layer after deposition
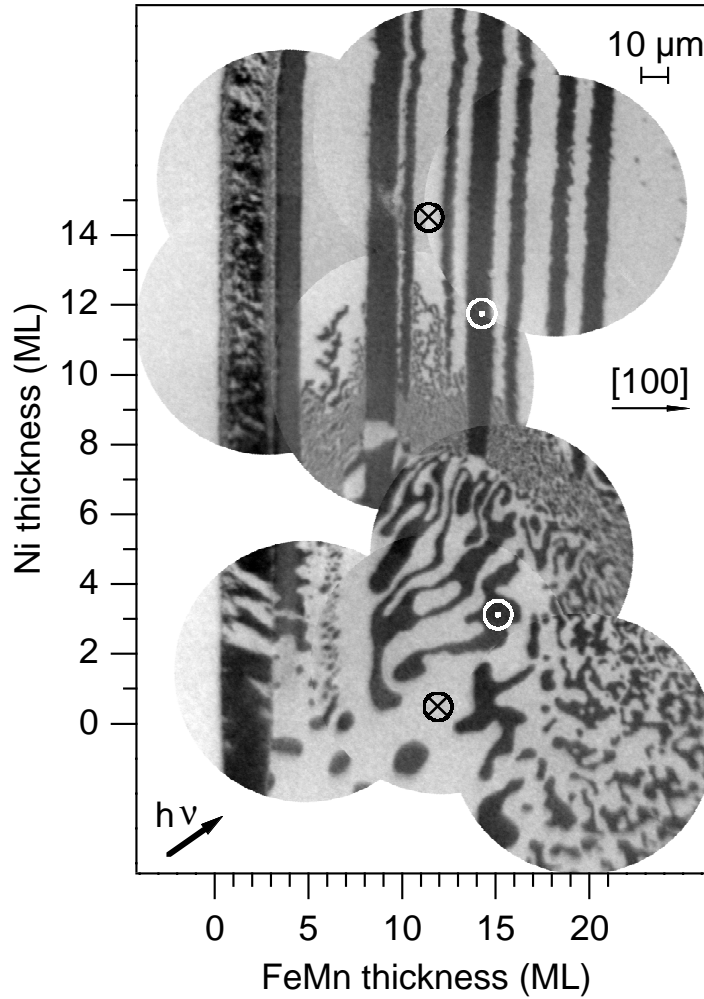
Figure 3.13: Layer-resolved magnetic domain images of a 15 ML Ni/0–20 ML Fe$_{50}$Mn$_{50}$/0–15 ML Ni trilayer epitaxially grown on Cu(001). After deposition of the first Ni layer an external magnetic field as a short pulse has been applied along a direction perpendicular to the sample surface. The image represents the domain pattern of the top Ni layer.

on top of 17 ML Fe$_{50}$Mn$_{50}$.

A stripe of very small domains extends from $t_{Ni} = 8$ ML, $t_{FeMn} = 5$ ML to $t_{Ni} = 5$ ML, $t_{FeMn} = 17$ ML. These small domains extend to higher Ni thicknesses only in the white domains of the stripe-like domain pattern observed for $t_{Ni} > 10$ ML. For Ni on Cu(001), 8 ML thickness corresponds to the spin-reorientation-transition from in-plane to out-of-plane direction of magnetization. Small domains are formed in the top Ni layer as a consequence of the interlayer coupling between Ni top layer with an out-of-plane magnetization direction and Ni bottom layer with an in-plane magnetization direction [93]. To lower its magnetostatic stray field energy,

domains of alternatingly up and down magnetization are energetically more favorable in the top Ni layer. Because the effective anisotropy is reduced by the coupling to the in-plane Ni magnetized layer smaller domains become energetically more favorable. Lowest the energy it cost the creation of domain walls inside which the in-plane magnetization is present. The white stripes correspond to a ferromagnetic coupling between bottom and top Ni layers. Presence of the interface roughness may introduce, in addition, an "orange-peel" like coupling which adds to the ferromagnetic coupling. Therefore, small domains are formed to minimize the energy. These small domains are not present in the black stripe because the energy of the system for an antiferromagnetic coupling is lower as compared with ferromagnetic coupling.

When the thickness of the bottom Ni layer exceeds 10 ML (the upper part of the image), oscillations of the magnetization direction as a function of Fe$_{50}$Mn$_{50}$ are observed. The most left part of the image, where no Fe$_{50}$Mn$_{50}$ is deposited, the white single domain reveals an out-of-plane direction of magnetization of Ni bottom layer. In the thickness range of 0 to 3 ML Fe$_{50}$Mn$_{50}$, a stripe-like domain is seen with very small features inside. In the previous section when Fe$_{50}$Mn$_{50}$ is deposited on Co, below an Fe$_{50}$Mn$_{50}$ thickness of about 3 ML, it becomes fully ferromagnetic by the proximity of the ferromagnetic Co layer. Assuming a similar ferromagnetic behavior of Fe$_{50}$Mn$_{50}$ when deposited on Ni, a ferromagnetic coupling between the bottom and top Ni layers may be expected. A comparison of this stripe with the white single domain where no Fe$_{50}$Mn$_{50}$ tells us that both Ni layer may be in-plane here. Indeed, analysis of the gray scale of Ni reveals a canting towards in-plane of the Ni magnetization direction.

When following the upper part of Fig. 3.13 an oscillatory change of the top layer magnetization direction as a function of Fe$_{50}$Mn$_{50}$ thickness can be seen. From a fit of the oscillatory behavior of the Ni magnetization a long oscillation period with 5 ML period and a short oscillation period of 2 ML period with the Fe$_{50}$Mn$_{50}$ thickness are deduced. The short period of oscillations are present only above 8 ML Fe$_{50}$Mn$_{50}$. As seen in the previous section, Sec. 3.3, when Fe$_{50}$Mn$_{50}$ sandwiched in between two FM layers, the phase transition from paramagnetism to antiferromagnetism occurs at room temperature at about 7 ML thickness. Hence, the presence of small period of oscillation might be related with the ordered antiferromagnetic state of Fe$_{50}$Mn$_{50}$.

Studies of the growth and surface morphology of Ni on Cu(001) have reported a transition to a "multilayer" growth with well-separated 3 D rectangular islands at a thickness of 4 ML [94]. Post annealing, of the deposited film, at 450 K causes a coalescence of the islands, resulting in a morphology with a smoother surface, similar to that of layer-by-layer growth, without segregation of Cu [95].

The presence of two periods of oscillation in Fig. 3.13 is addressed in a second experiment where the bottom Ni layer has been annealed in order to smooth the surface. After deposition of 15 ML Ni as a continuous film the sample was annealed for 15 minutes at 450 K. After cooling down to room temperature, an external magnetic field ($\approx 500\,\text{Oe}$) has been applied in a

direction perpendicular to the sample surface. On top of this, 24 ML Fe$_{50}$Mn$_{50}$ were deposited as a wedge, followed by deposition of another 15 ML Ni as a continuous film.
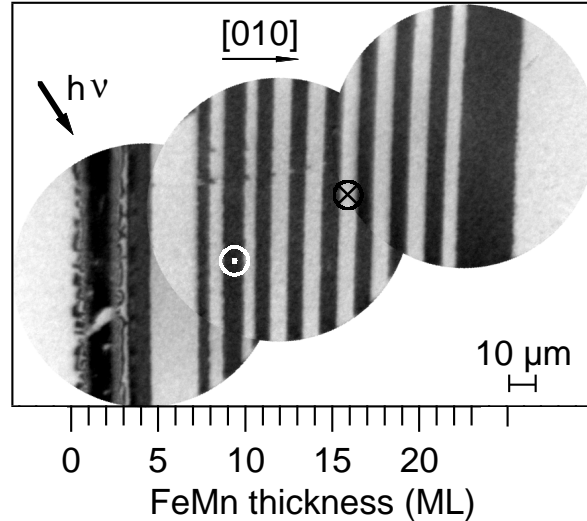
Figure 3.14: Layer-resolved magnetic domain images of a 15 ML Ni/0–24 ML Fe$_{50}$Mn$_{50}$/15 ML Ni trilayer epitaxially grown on Cu(001). The image represents the domain pattern of the top Ni layer. After deposition of the first Ni layer, the sample was annealed at 450 K for 15 minutes and cooled down to room temperature before deposition of Fe$_{50}$Mn$_{50}$. The direction of the top Ni layer magnetization shows an out-of-plane oscillatory change with a period of 2 ML Fe$_{50}$Mn$_{50}$ thickness.

Fig. 3.14 presents the magnetic domain image obtained at the Ni L_3 edge. The Fe$_{50}$Mn$_{50}$ thickness varies in the range of Fig. 3.14 from 0 to 24 ML from left to right, as indicated at the bottom axis. The direction of the incoming light is indicated by a small arrow at the upper left side of the image.

The left most part of the image in the region without Fe$_{50}$Mn$_{50}$ and in the right most part of the image, on the Fe$_{50}$Mn$_{50}$ plateau, both layers are in a single domain state. Below 3 ML Fe$_{50}$Mn$_{50}$ a black stripe with small features at the edges is seen. Similar to the case of the not-annealed sample, in this thickness range the magnetization of the Ni layer is canted towards in-plane directions. The black stripe seen at about 4 ML Fe$_{50}$Mn$_{50}$ in Fig. 3.13 is also present in the Fig. 3.14. A periodic out-of-plane oscillatory coupling with 2 ML period starts above 7 ML Fe$_{50}$Mn$_{50}$. For the as-grown sample, Fig. 3.13, the short period oscillations are also present only above 7 ML Fe$_{50}$Mn$_{50}$. The increased width of the right most dark stripe is probably just an artifact related to the rounded beginning of the plateau at the upper end of the Fe$_{50}$Mn$_{50}$ wedge. The irregular position of the 24 ML abscise axis is intended to illustrate this effect.

In order to gain deeper insight into the spin structure of Fe$_{50}$Mn$_{50}$ in these trilayers, the same procedure as in the previous section, Sec. 3.3, is applied. Deposition of a Co layer,
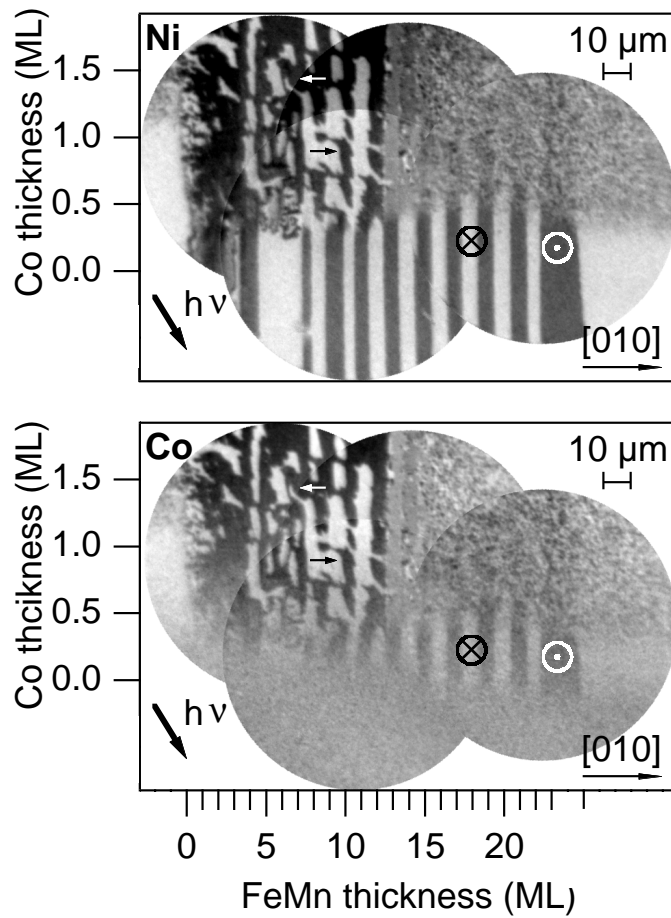
Figure 3.15: Layer-resolved magnetic domain images of 0–2 ML Co/15 ML Ni/0–24 ML Fe$_{50}$Mn$_{50}$/15 ML Ni/Cu(001). The map of Co domain images is shown at the bottom side, the map of the Ni domain images at the upper side. Deposition of more than 0.5 ML Co top layer induces a spin-reorientation-transition in Ni from out-of-plane to in-plane. Small domains, in-plane magnetized are present only above 12 ML Fe$_{50}$Mn$_{50}$ thickness.

with an in-plane anisotropy, can induce a spin-reorientation-transition of the top Ni layer from out-of-plane to in-plane.

Fig. 3.15 shows domain images obtained at the Ni L_3 edge (upper panel) and (Co L_3 bottom panel) of the 0–2 ML Co deposited as a wedge on top of the same Ni/Fe$_{50}$Mn$_{50}$/Ni trilayer. The Fe$_{50}$Mn$_{50}$ thickness varies in the range of Fig. 3.15 from 0 to 24 ML Fe$_{50}$Mn$_{50}$ from left to right, as indicated at the bottom axis, and the Co thickness from 0 to 2 ML from bottom to top, as indicated at the left axis. The direction of the incoming light is illustrated by the arrows at the left bottom corner of each image.

The bottom part of the Co image, of Fig. 3.15, below 0.5 ML Co, shows the same oscillatory

changing of the magnetic contrast as before Co deposition, Fig. 3.14, with 2 ML Fe$_{50}$Mn$_{50}$ period. The out-of-plane Ni anisotropy obviously turns the Co magnetization out-of-plane within this region. The deposition of the top Co layer with a thickness below 0.5 ML does not exert any influence on the Ni magnetization direction.

For a Co thickness above 0.5 ML, the direction of the Ni magnetization changes from out-of-plane to in-plane as indicated by small arrows. The wide white out-of-plane stripe seen in Ni at 5 ML Fe$_{50}$Mn$_{50}$ for $t_{Co} < 0.5$ ML, forms relatively small domains, magnetized in plane, after deposition of more than 0.5 ML Co. Above 6 ML Fe$_{50}$Mn$_{50}$ elongated in-plane domains are seen. In this region some correlation between the Ni out-of-plane stripe like magnetic domains structure before Co deposition and the in-plane domains after the spin-reorientation-transition induced by the Co layer is observed. For an Fe$_{50}$Mn$_{50}$ thickness above 12 ML very small domains, most likely magnetized in-plane, are formed in the top FM layer, exactly as they are observed in as-grown Co/Fe$_{50}$Mn$_{50}$ bilayers [15]. This means that in the entirely out-of-plane magnetized Ni/Fe$_{50}$Mn$_{50}$/Ni trilayer, there must be still a statistically fluctuating in-plane component which can force the in-plane direction of magnetization of the top FM layer to a small domain configuration. Such small domains are energetically unfavorable and disappear as soon as the antiferromagnetic layer is heated above the Néel temperature [15]. They do not occur in trilayers with identical anisotropy of both ferromagnetic layers, or in bilayers in which the ferromagnetic layer is deposited first, see for example Fig. 3.6, page 38. The presence of small domains in the top ferromagnetic layer in trilayers with different anisotropy, however, shows that perpendicular spin component behaves independently, as if the bottom ferromagnetic layer was not present. A three-dimensional spin structure in the Fe$_{50}$Mn$_{50}$ layer has consequently to be considered. This will be discussed in Sec. 5.4.

Chapter 4

Magnetic coupling across Cu layers

Besides the well studied indirect oscillatory magnetic interlayer exchange coupling also micro-magnetic mechanisms can lead to a coupling between magnetic layers across nonmagnetic spacer layers in thin film multilayered structures. They are related to the microscopic properties, such as structure or morphology, but also to the purely magnetic microstructure, i.e., the magnetic domain structure. The latter, a coupling related to the magnetic domain structure, is mediated by magnetostatic stray fields from domain walls.

Despite its obvious importance, relatively little work up to now has focused on the micro-magnetic interactions in magnetic interlayer coupling. This may be due to the lack of adequate techniques, which must not only provide microscopic lateral resolution but also allow layer-selective probing of the magnetic domain structure.

Spin valve systems (SVS) have attracted considerable interest because of their potential in applications such as nonvolatile magnetic random access memory (MRAM) and read heads of magnetic hard disk drives [96]. In its simplest form, the SVS consists of two magnetic layers with different coercivity, respectively called soft and hard, separated by a non-magnetic spacer layer. The magnetization of one FM hard layer can be fixed by an adjacent antiferromagnetic (AFM) layer (the pinning layer) through exchange bias coupling. The performance of the SVS depends critically on the way the magnetization distribution evolves under the application of an external magnetic field. Up to now, much attention has been paid to the study of the transport properties and its dependence on the roughness or chemical homogeneity of the interface [97]. However, many other effects such as magnetization reversal processes, domain formation and implication of the domain structure of each magnetic layer have been only recently considered [98].

A direct consequence of these features is that the domains and domain walls give rise to conduction channels with different resistances determined by the lateral fluctuations of the angle between the magnetic moments of the two magnetic layers. When the soft layer has a single domain configuration, after switching, the magneto-resistance (MR) signal is only sensitive

to the direction of magnetization direction. In contrast, magnetic domains can introduce low resistance channels. Acting like "shortcuts", the presence of walls will not allow the resistance of the junction to reach its maximum value. Fig. 4.1 shows schematically how the magnetic domains in the hard layer locally disturb the fully parallel (a), respective antiparallel (b) alignment of the ferromagnetic layers.

(a)   (b)
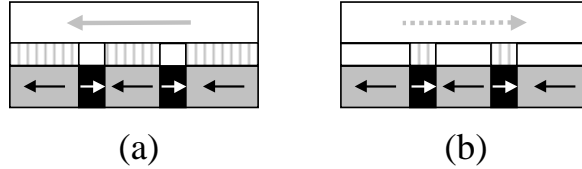
Figure 4.1: Schematic view of the different conduction channels corresponding to walls, as a function of the relative orientation of the magnetization direction of the FM layers.

Previous studies for coupled films have shown that when the soft layer, Co in that case, was cycled in an external magnetic field, lower than the coercive field of the hard layer, the magnetic moment of the hard $Co_{75}Pt_{12}Cr_{13}$ layer decayed logarithmically with the number of switching cycles [99]. When coherent field rotation of the soft layer was used to achieve magnetization reversal, no such decay was observed. Because field reversal normally proceeds by formation or motion of domain walls (or both), neither of which occurs during field rotation, it appears likely that domain walls in the soft layer might have been responsible for the decay.

It has already been demonstrated using depth-selective Kerr microscopy how the switching behavior of the top Fe layer in Fe/MgO/Fe(001) is influenced by the stray fields from the moving domain walls of the Fe substrate [100]. The stray field of each domain wall can either increase or decrease the effective field seen by the soft layer depending on its orientation with respect to the applied field. So, this inhomogeneous field can induce a domain structure in the soft layer if the energy needed to create domain walls is lower than the coupling energy.

In this chapter I will present a photoelectron emission microscopy (PEEM) study of ultra-thin single-crystalline FeNi/Cu/Co/FeMn and Co/Cu/Ni layered systems grown epitaxially on Cu(001). Using X-ray magnetic circular dichroism (XMCD) as magnetic contrast mechanism, discussed in chapter 2, this method is capable of layer resolved microscopic domain imaging due to the element-selectivity of XMCD. This allows to image the domain configuration of each magnetic layer separately, and identify local coupling phenomena caused by domain wall stray fields.

The aim of the first section of this chapter, Sec. 4.1, is to show for FeNi/Cu/Co layered films how the magnetization reversal of the soft FeNi layer is influenced by the domain structure of the hard Co layer. In the second part, Sec. 4.2, I present layer resolved domain images of Co/Cu/Ni trilayers which show that the stray fields from Ni domain walls strongly influence the Co domain structure in the as-grown state. By application of competing external magnetic

fields the strength of this coupling due to domain wall stray fields can be estimated to about 250 Oe.

4.1 The FeNi/Cu/Co trilayer system

In this section I present a layer-resolved PEEM study of the magnetic coupling between an FeNi alloy (60% Fe, 40% Ni) layer and a Co layer, across Cu as a nonmagnetic spacer layer, epitaxially grown as continuous films on Cu(001). Conclusions about the global and the micromagnetic coupling between the Co and FeNi magnetic layers can be drawn from the comparison of magnetic domain images of the Co and FeNi layers at the same position on the sample. The magnetization of the Co layer is pinned to an adjacent antiferromagnetic FeMn layer through exchange interaction. In the as-grown state of Co on FeMn with a thickness higher than 10 ML, small domains are induced in Co, with magnetization pointing along the $\langle 100 \rangle$ in-plane directions. By heating up the sample to 480 K (above the AF order temperature of FeMn), the Co magnetization rearranges into bigger domains. In these domains Co is magnetized along $\langle 110 \rangle$, in-plane directions. After cooling back to room temperature, the domain pattern remains qualitatively identical, while the Co magnetization direction is oriented along $\langle 100 \rangle$ for Co thicknesses below ≈ 10 ML. For Co thicknesses above 15 ML, the Co magnetization on top of antiferromagnetic FeMn is found to rotate back along $\langle 110 \rangle$ directions due to increasing total anisotropy energy in the Co film [101] as the film becomes thicker .

Figure 4.2 shows element resolved domain images of 5 ML FeNi/5 ML Cu/15 ML Co/15 ML FeMn/Cu(001). The left hand panels (a), (c) and (e) show domain images of the FeNi layer, obtained at the Fe L_3 edge, panels (b), (d) and (f) on the right hand side show domain images of the Co layer, obtained at the Co L_3 edge. The incoming light direction is indicated by the small arrow at the bottom side of the figure. Frames (a) and (b) show the as-grown domain patterns of the FeNi and Co layer. Within the field of view, relatively large domains are seen in Co with magnetization oriented along $[\bar{1}10]$ and $[1\bar{1}0]$. The direction of magnetization is indicated in some of the domains by small arrows. Analysis of the different gray scales of the Fe L_3 image, frame (a), reveals that the FeNi magnetization direction in the as-grown state is oriented along the four $\langle 100 \rangle$ crystal axes, as indicated by arrows. A closer look at the big domains observed in the FeNi reveal that they are mainly related to the similarly shaped Co domains.

The magnetization of the FeNi domains located over brighter domains in the Co layer with the magnetization along $[\bar{1}10]$ is mainly oriented along $[010]$, while the FeNi domains located over darker Co domains with the magnetization along $[1\bar{1}0]$ are mainly pointing along $[0\bar{1}0]$. These observations can be interpreted as a ferromagnetic coupling competing with different anisotropy in Co and FeNi, Co along $\langle 110 \rangle$, FeNi along $\langle 100 \rangle$. Probably the weaker interlayer coupling energy than the FeNi magnetic anisotropy energy could not align the Co and FeNi magnetizations.
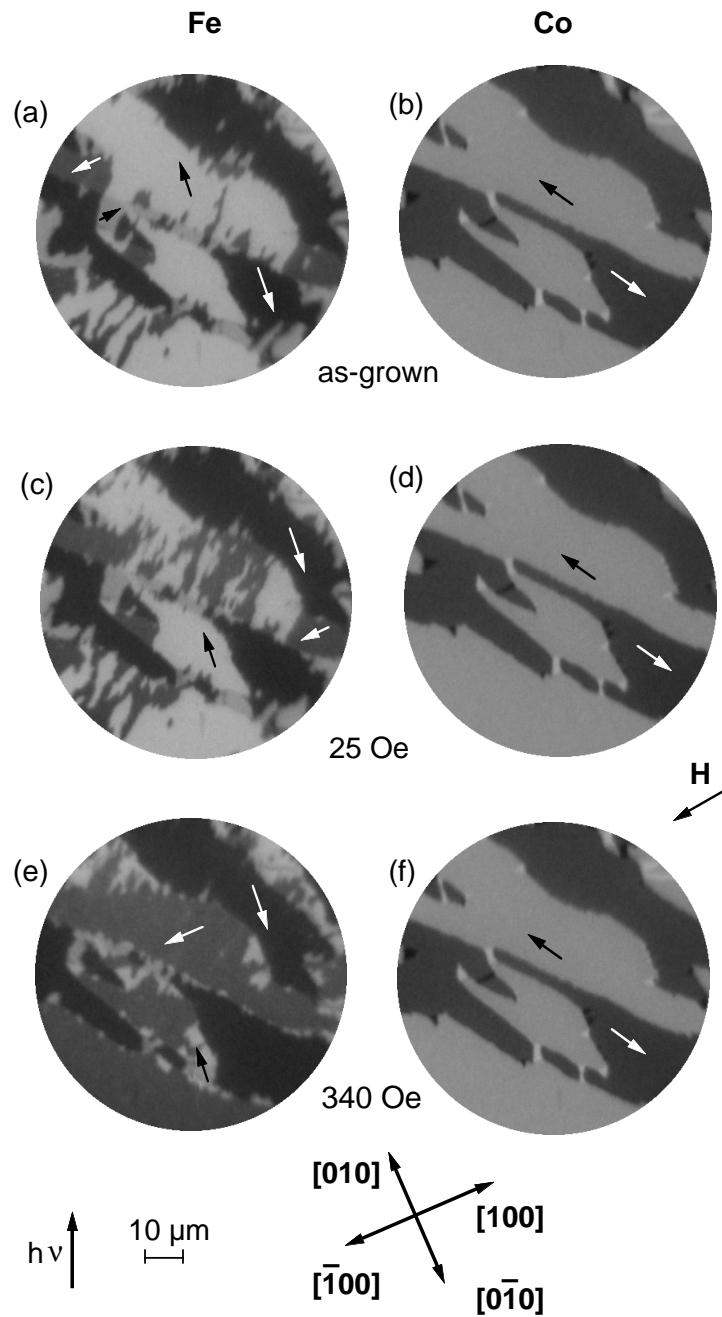
Figure 4.2: Element resolved domain images of a 5 ML FeNi/5 ML Cu/15 ML Co/15 ML FeMn film structure on Cu(001). (a), (c), (e): FeNi domain patterns, (b), (d), (f): Co domain patterns. (a) and (b) show the domain patterns of the as-grown trilayer; (c) and (d) after the application of a 25 Oe external field in the direction labelled by "H"; (e) and (f) after the application of a 340 Oe external field in the same direction.

Panels (c) and (d) of Fig. 4.2 show Fe and Co element resolved domain images, respectively, after the application of an external in-plane field of 25 Oe in the direction indicated by "H", which was approximately along the $[\bar{2}\bar{1}0]$ direction. No changes are seen in the Co image (d) after the application of the external field. Some darker domains have nucleated within the white domains in the Fe image. The small dark domains with the magnetization oriented along $[\bar{1}00]$, located at the edge of the brighter domains in panel (a), become bigger after the application of the external field. Fig. 4.2 (e) and (f) show the layer resolved Fe and Co domain images, respectively, after the application of a 340 Oe external magnetic field, much higher than before, in the same direction. The Co image (f) is still unchanged after the application of the external field, but significant changes are observed in the Fe image, panel (e), with respect to panel (c). The magnetization in the originally FeNi brighter domains, located above the brighter Co domains with the magnetization oriented along $[\bar{1}10]$, changed nearly everywhere by 90° from $[010]$ to $[\bar{1}00]$. However, small domains, with the magnetization direction still oriented along $[010]$, decorate the edges of the big domains. When superimposing the domain walls from Co, panel (f), onto the Fe image, panel (e), we can clearly see that these unchanged domains are located along the Co domain walls. No visible changes are seen within the darker domains in the Fe image after application of the external magnetic field in the direction indicated on the figure. These regions are those located over Co dark domains with magnetization pointing along $[1\bar{1}0]$. The ferromagnetic coupling between the Co and FeNi layers will favor both $[0\bar{1}0]$ and $[100]$ easy directions of the FeNi layer above a Co black domain. In an external magnetic field

Fe   **Co**

(a)   (b)

H

-340 Oe

hν   10 µm

[010]   [100]

[$\bar{1}$00]   [0$\bar{1}$0]
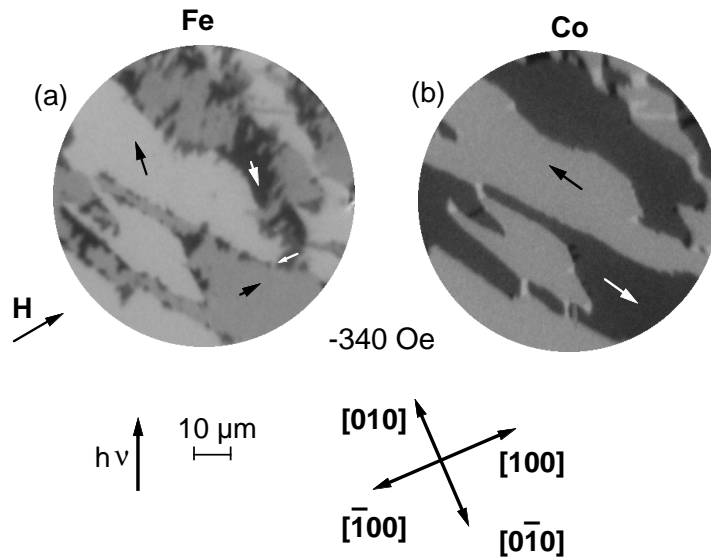
Figure 4.3: Element resolved domain images of a 5 ML FeNi/5 ML Cu/15 ML Co/15 ML FeMn film structure on Cu(001). (a) FeNi domain pattern, (b) Co domain pattern after the application of a 340 Oe external field in the direction labelled by "H".

applied close to the $[\bar{2}\bar{1}0]$ direction, the $[100]$ direction becomes unfavorable from an energetic point of view. The switching to $[\bar{1}00]$ would require a higher magnetic field in order to overcome the ferromagnetic coupling to the dark domains in the Co layer, with magnetization pointing along $[1\bar{1}0]$. Hence, for FeNi located over darker domains in Co, the energetically most favorable orientation is $[0\bar{1}0]$. The $[010]$ and $[\bar{1}00]$ directions are favored by the coupling in the FeNi layer when located above a Co white domains with the magnetization along $[\bar{1}10]$. A small external magnetic field applied along $[\bar{2}\bar{1}0]$ could be high enough to make the $[\bar{1}00]$ direction the most favorable. The measurements with an external magnetic field applied in an opposite direction confirms that the mechanism presented is responsible for the observed changes.

Figure 4.3 shows the magnetic domain images after application of a 340 Oe external magnetic field in the direction labelled by "H", opposite than in the case shown in Fig. 4.2. The FeNi layer located over brighter domains in Co has now mainly switched back to the $[010]$ direction, while large parts of the FeNi layer located over darker domains in Co rotates to $[100]$. No changes are observed in the Co image. A closer look to the Fe image, Fig. 4.3 (a), reveals again the presence of small domains, now dark, with the magnetization oriented along $[\bar{1}00]$, located over the domain walls of the Co layer.

Indeed, the subtraction of the two images, acquired after an external field of 340 Oe applied in the two opposite directions (Fig. 4.2 (e) minus Fig. 4.3 (a)), shown in Fig. 4.4, confirms clearly that only these regions are not switching after the application of the external magnetic field. The difference images were compiled by careful alignment and subtraction of one image from the other. This procedure is useful in detecting slight changes in the magnetic domain images acquired after application of an external magnetic field of different values. Unchanged regions will appear with contrast corresponding to zero (brighter areas in Fig. 4.4), while the high dark contrast results from the regions altered by the magnetization changes of the FeNi layer. The
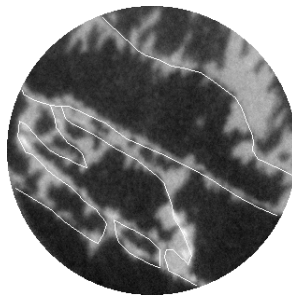
Figure 4.4: Subtraction of two element resolved images of Fe after application of an external field of 340 Oe in opposite directions. In the dark regions, the FeNi magnetization has switched while it remained unchanged in the bright regions located over domain walls in the Co layer. The white thin lines superimposed to the FeNi image indicate the position of the domain walls of the Co layer.

position of the Co domain walls, obtained from a contour plot of the Co domain pattern, is

shown superimposed on the Fe difference image, Fig. 4.4, as white lines. It is clearly seen that the regions in the FeNi layer that are either harder to switch or turn back to their original magnetization direction after the end of the field pulse are located in the vicinity of the domain walls in the Co layer. This can be interpreted as the effect of a local field induced by the stray field of Co domain walls which adds to the ferromagnetic coupling field thus increasing (decreasing) the value of the external magnetic field needed to reverse these regions.

In Fig. 4.2 the Co magnetization direction in the big white and dark domains is pointing along $[\bar{1}10]$ and $[1\bar{1}0]$. Assuming a Néel type of domain wall in Co, the stray field associated with it, will have an in-plane component either along the $[110]$ or $[\bar{1}\bar{1}0]$ crystal axes. Let us arbitrarily assume a stray field oriented along $[110]$, from Co dark to Co white domains. In the vicinity of the domain walls the stray field adds to the ferromagnetic coupling between the FeNi and Co layers. For example, above the white Co domain, close to the domain walls, the $[010]$ easy direction of the FeNi will be more favorable. The external magnetic field must not only "break" the interlayer coupling but also overcome, locally, the domain wall stray field. In Fig. 4.2 (e) the small domains located over the domain walls of Co appear brighter and in Fig. 4.3 (a) darker. It means that when following a Co Néel wall, locally, the stray field shows different orientations. This will be discussed in more detail in Sec. 5.5.

4.2   The Co/Cu/Ni trilayer system

In this section the stray field induced coupling is investigated for domain walls of 15 ML Ni with an easy axis oriented out-of-plane, cf. Sec. 3.3. Epitaxially grown 15 ML Ni films on Cu(001) show alternatingly up and down magnetized stripe-like domains. This leads to a partial flux closure outside the Ni layer and reduces the otherwise unfavorable magnetostatic dipolar energy of perpendicularly magnetized films. Close to the walls between these domains the flux lines outside the Ni layer provide a substantial magnetic field component in the film plane, in the direction perpendicular to the domain wall. A schematic sketch of the stray field for perpendicularly magnetized films is shown in Fig. 4.5. Layer resolved domain images of the Co/Cu/Ni trilayers, presented in this section, show that the stray fields from Ni domain walls strongly influence the Co domain structure in the as grown state. In Fig. 4.6 element resolved domain images of a 4 ML Co/5.7 ML Cu/15 ML Ni/Cu(001) trilayer are presented. The left panel (a) shows the domain image of the Ni layer, and panel (b) on the right shows the domain image of the Co layer. The crystal axes and the direction of incoming light are indicated at the left bottom side of panel (a). In addition to the very different domain patterns in Ni and Co, also indications for microscopic interaction between the two layers can be found. White lines in the Co image mark the position of the Ni domain walls obtained from the 50% intermediate contour line between the white and black contrast in a contour plot of Fig. 4.6 (a). They facilitate the discussion of the correlation between the as-grown Ni and Co domains patterns. All the
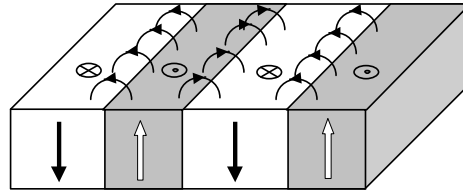
Figure 4.5: Schematics of the magnetic stray field above a perpendicularly magnetized film with stripe domains. Above the domain walls the flux closure lines provide a magnetic field component in the film plane, perpendicular to the domain wall.

larger black domains in the Co image, Fig. 4.6 (b), are related to similarly shaped Ni domains of Fig. 4.6 (a). At about the middle of the image these black domains in Co correspond to black domains in Ni, whereas at the bottom of the image a black domain in Co is located at the position of a white domain in Ni. Closer inspection of the element resolved domain patterns reveals that in the regions of correlated domain patterns the domain walls in Co are shifted right or left with respect to the corresponding domain walls in Ni. Two such positions are pointed out by lines at the bottom of Fig. 4.6 (b), and the situation at these domain boundaries is illustrated by sketches below the images. The shift of the Co domain walls can be explained by stray fields from the Ni domain walls. Let us first consider the left sketch. A domain wall in Ni separates a white/down domain on the left from a black/up domain on the right. This causes a stray field above the Ni film with an in-plane component pointing to the left, as indicated in the sketch. The Co layer, at that position, has a white/right domain on the left hand side, and a black/left domain on the right hand side. Since the in-plane component of the stray field from the Ni domain wall is pointing to the left, the domain wall in Co is shifted to the left in order to expand the black/left domain on the expense of the white/right domain. The other sketch on the right hand side illustrates a spot on the sample where the opposite situation is encountered: Here a domain wall is separating a white/right domain in Co on top of a black/up domain in Ni on the left hand side from a black/left domain in Co on top of a white/down domain in Ni on the right hand side. The stray field above the Ni domain wall is now pointing to the right. This extends the white/right domain in Co, and leads to a shift of the Co domain wall to the right.

To demonstrate the influence of these stray fields on the Co layer, we present in Fig. 4.6 (c) and (d) histogram plots of the Co magnetization above Ni domain wall sections vertical to the image. Here the meaning of "vertical" was extended to include domain walls in Ni that are inclined by up to 8° from the vertical image direction. The gray scale bars at the top of panels (c) and (d) indicate the graytones of Fig. 4.6 (b) which correspond to the respective histogram bars. Fig. 4.6 (c) shows the histogram corresponding to the situation of the left sketch, where a Ni domain wall separates a white/down domain on the left from a black/up domain on the right. It is clearly seen that in the Co layer virtually everywhere above this kind of Ni domain wall
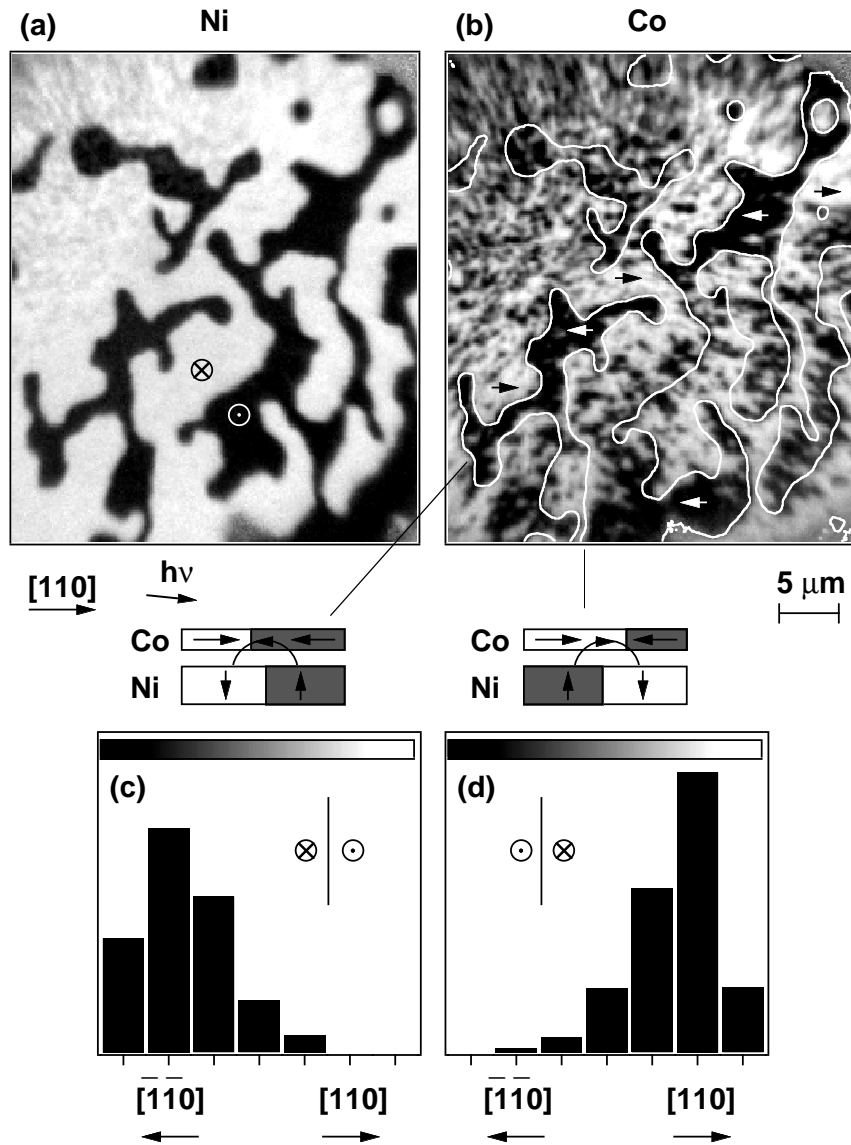
Figure 4.6: Element resolved domain images of an as-grown 4 ML Co/5.7 ML Cu/15 ML Ni on Cu(001) trilayer. (a) domain image of the Ni layer; (b) domain image of the Co layer. The white lines in (b) mark the position of Ni domain walls in (a). Two sketches underneath the domain images illustrate the relative orientation of Co and Ni magnetization at the two indicated spots in the image. (c) histogram of the Co magnetization contrast above Ni domain wall sections which run within 8° along the image vertical and correspond to the situation shown in the left sketch; (d) the same as in (c), but for Ni domain wall sections corresponding to the right sketch.

the magnetic contrast is black, i.e., the magnetization is pointing to the left. This minimizes the Zeeman energy of the Co magnetization in the local stray field of the Ni domain wall. The situation corresponding to the opposite sense of rotation of Ni domain walls is presented in Fig. 4.6 (d). Here the Co magnetization is nearly exclusively pointing to the right, in agreement with what is expected from the stray field argument.

To get an estimate of the size of the stray fields from the Ni domain walls in the Co layer, the effect of an external magnetic field on the Co domain pattern in Co/Cu/Ni/Cu(001) was studied. Figure 4.7 shows the effect of an external magnetic field on element resolved remanent domain images. Here the sample was a 4 ML Co/6 ML Cu/15.5 ML Ni trilayer on Cu(001), and the magnetic field was applied by pulses of about 1 ms duration in between subsequent exposures. The field of view was selected to have Ni domain walls running predominantly in one direction, here roughly along [120]. Frames (a) and (b) show the as-grown domain patterns of the Ni and Co layer, respectively. The light incidence azimuth was along [010], as indicated at the bottom of Fig. 4.7. Arrows in the images indicate the direction of local magnetization. Within the field of view, in Co only [$\bar{1}10$] and [$1\bar{1}0$] domains are observed, as was confirmed by azimuthal rotation of the sample. Note that for the present geometry, where the azimuthal angle of light incidence is 45° to the [110] direction, the contrast from [110] and [$\bar{1}10$] magnetization directions would be indistinguishable, and also the contrast from [$\bar{1}\bar{1}0$] and [$1\bar{1}0$]. Only one of the two senses of correlation between Ni and Co magnetization, the one corresponding to the left sketch in Fig. 4.6 and its periodic extension to a stripe-like pattern, is present here. The position of Ni domain walls, obtained from a contour plot of the Ni domain pattern of Fig. 4.7 (a), is superimposed to Fig. 4.7 (b) as white lines. It is clearly seen that the domain walls in Co are shifted upwards and left compared to the Ni domain walls. Small arrows at the top of Fig. 4.7 (b) indicate the sense of the in-plane component of the stray field of each of the Ni domain walls.

Line scans of the as-grown Co and Ni L_3 asymmetry along the long side of the rectangle shown in Fig. 4.7 (a) are reproduced in the upper part of Fig. 4.8, in which the asymmetry was averaged along the width of the rectangle. For better comparison with the Co line scan, the Ni asymmetry has been reversed in sign and scaled by a factor of five. The shift of the in-plane domain walls with respect to the Ni domain walls is very well recognized. The domain wall displacement differs a bit at each domain wall, and on average amounts to about 400 nm. Panels (c) and (d) of Fig. 4.7 show the Ni and Co element resolved domain images, respectively, after the application of an external field of 240 Oe in the direction indicated by H, which was approximately along the [$\bar{2}\bar{1}0$] direction. Whereas the Ni image (c) is virtually unchanged after the application of the external field, significant changes are observed in the Co image. Some black domains have nucleated within the previously white domains. Because of the direction of the magnetic field, these black domains correspond to a magnetization along [$\bar{1}\bar{1}0$]. The white lines in panel (d) are again the 50% contour lines of panel (c). Interestingly the shift of Co domain walls compared to the Ni domain walls is now even bigger than in the as-grown images (b)

Ni   **Co**

(a)   **(b)**

as-grown

(c)   **(d)**

240 Oe

H

(e)   **(f)**

265 Oe

hν **10 μm** $[\bar{1}10]$ $[110]$

   $[\bar{1}\bar{1}0]$ $[1\bar{1}0]$
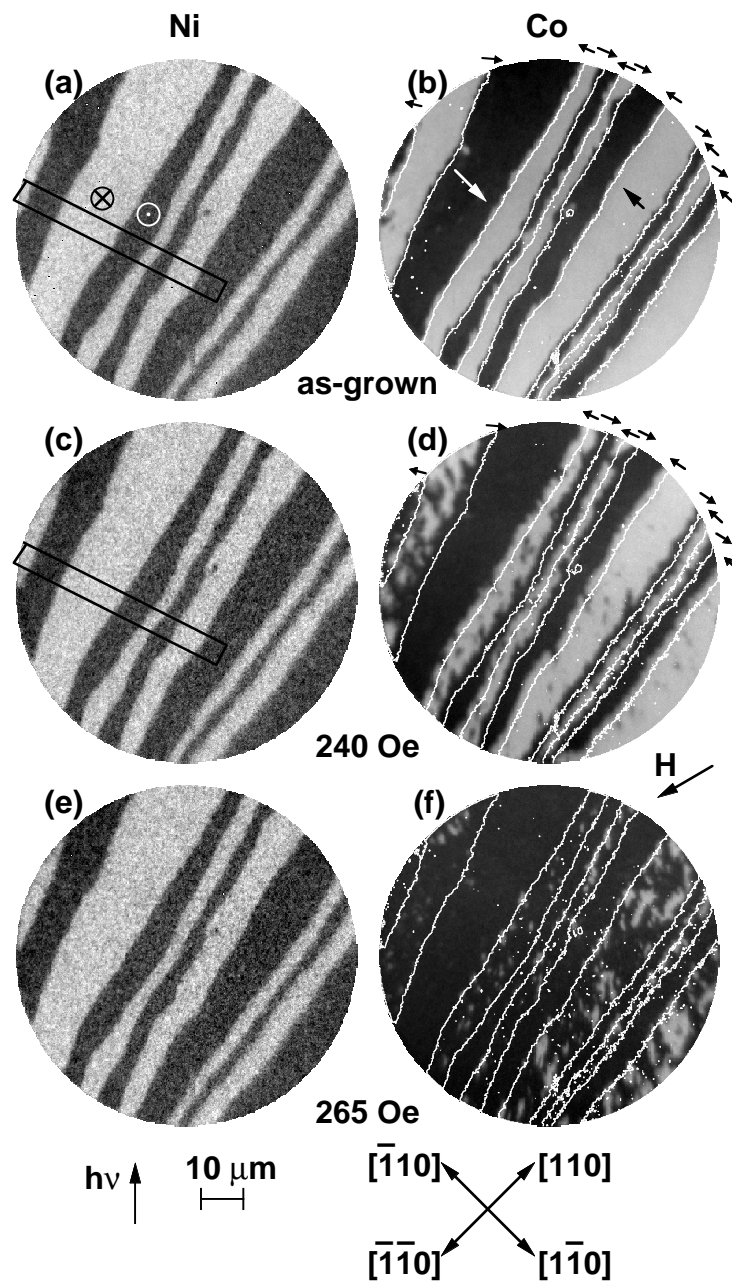
Figure 4.7: Element resolved domain images of a 4 ML Co/6 ML Cu/15.5 ML Ni trilayer on Cu(001). (a), (c), (e): Ni domain patterns, (b), (d), (f): Co domain patterns. (a) and (b) show the domain patterns of the as-grown trilayer; (c) and (d) after the application of a 240 Oe external field in the direction labelled by "H"; (e) and (f) after the application of a 265 Oe external field in the same direction. The white lines in (b), (d), (f) mark the position of Ni domain walls in the respective Ni domain images (a), (c), (e). The small arrows above the upper edge of (b) and (d) mark the direction of the in-plane component of the stray fields caused by the Ni domain walls. The rectangles in (a) and (c) indicate the area where the line scans presented in Fig. 4.8 have been taken.

vs. (a). This can be more clearly seen from linescans of Fig. 4.7 (c) and (d), which are presented in the lower part of Fig. 4.8. Like before, these scans have been taken at the region indicated by the rectangle in Fig. 4.7 (c). The displacement of the Co domain walls is now between 1.2–1.7 μm, ignoring the leftmost stripe where many dark domains have nucleated inside the previously white stripe in the Co domain image. Fig. 4.7 (e) and (f) show the layer resolved Ni and Co
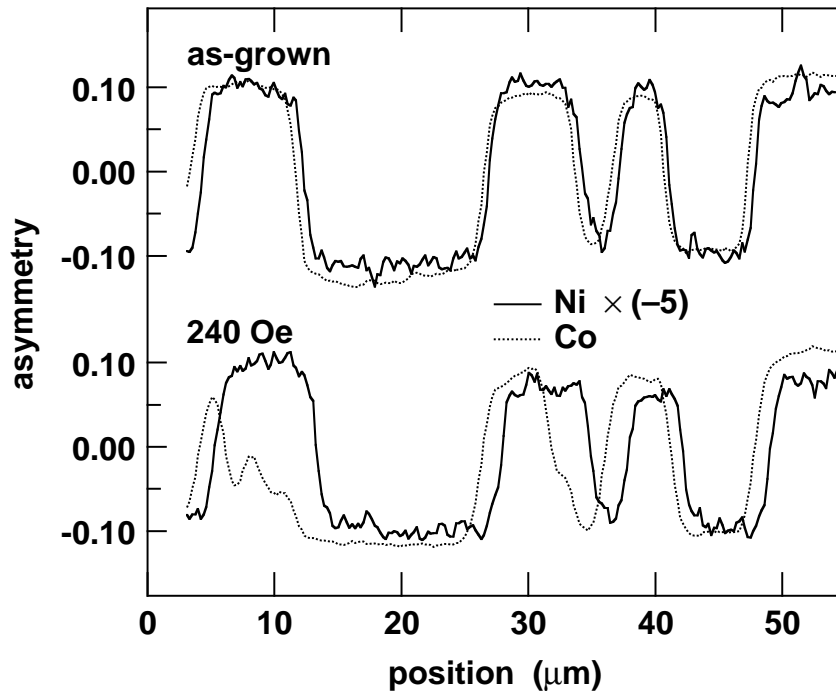
Figure 4.8: Line scans of the image asymmetry of the 4 ML Co/6 ML Cu/15.5 ML Ni trilayer on Cu(001), showing the displacement of the Co in-plane domain walls with respect to the Ni out-of-plane domain walls. Top: line scans from the as-grown domain images of Fig. 4.7 (a) and (b), taken along the long side of the rectangle displayed in Fig. 4.7 (a), averaging over the short side. Bottom: line scans from the domain images after application of a 240 Oe external field, as presented in Fig. 4.7 (c) and (d). Solid lines: scans of the Ni domain pattern, multiplied by −5, dotted lines: scans of the Co domain pattern.

domain images, respectively, of the same position after the application of a 265 Oe external magnetic field, only 15 Oe higher than before. Again the contour plot of the Ni domain walls of panel (e) is shown superimposed on the Co domain (f) by white lines. The Ni image (e) is still unchanged after the application of the external in-plane field, but significant changes are observed in the Co image, panel (f), with respect to panel (d). Now nearly everywhere a black contrast is observed, except for some white spots remaining at the position of the previously white stripe domains at the right hand side of the image. This behavior enables us to estimate the size of the stray field contribution to the local coupling between Ni and Co layers close to Ni domain walls. In the vicinity of Ni domain walls separating (from upper left to lower

right) white down domains from black up domains, the Co image exhibits a bright contrast after application of 240 Oe external field, i.e., magnetization along [$\bar{1}$10]. The in-plane component of the stray field from these domain walls is along [$\bar{2}$10]. During the 240 Oe pulse consequently a [$\bar{1}$10] domain survives, and re-expands to a certain extent after the field pulse. A 265 Oe field pulse, on the other hand, seems to annihilate these domains, so that after switching off the pulse only black contrast is observed. Because the axis of the domain wall stray field and the external field are approximately symmetric with respect to the crystallographic axes and to the horizontal of Fig. 4.7, the competition of both fields enables a direct comparison. Neglecting uniaxial magnetic anisotropies of the Co layer in the plane, it follows that the action of the in-plane component of the stray field from the Ni domain walls on the Co layer equals about that of an external field of 250 Oe.

Chapter 5

Discussion

This last part of the thesis is devoted to the discussion of the experimental results described in the previous chapters. In Sec. 5.1 the influence of roughness on the phase of coupling is understood within a qualitative model where part of the deposited AFM does not contribute to the interlayer coupling. Possible mechanisms behind this model are outlined. Sec. 5.2 focuses on the influence of roughness on the coupling strength and on the RKKY-like coupling and AFM exchange coupling. The experimental observations from Sec. 3.3 and Sec. 3.4 which lead to the conclusion of a non-collinear spin structure of $Fe_{50}Mn_{50}$ are discussed in Sec. 5.3. In the last section of this chapter, Sec. 5.5, the interlayer coupling mediated by domain wall stray fields is addressed.

5.1 Frustration of the interlayer coupling across single-crystalline $Fe_{50}Mn_{50}$

The magnetic interlayer coupling of $Co/Fe_{50}Mn_{50}/Co$ was shown in Sec. 3.2 to be strongly dependent on the atomic layer filling of the Co bottom layer. A change of the coverage of the Co bottom layer within 1 ML, for a similar $Fe_{50}Mn_{50}$ thickness, leads to a phase jump of the interlayer coupling. This could be seen even better in the layer-resolved domain images of $FeNi/Fe_{50}Mn_{50}/Co$, Fig. 3.6, page 38. A closer look into these stripes reveals a "saw-tooth" like periodic modulation of the coupling phase as a function of Co bottom layer thickness. The period of the modulation corresponds to 1 ML Co thickness. The absence of such a "saw-tooth" like modulation on the Co plateau indicates a correlation to the roughness of the bottom FM layer. Co on Cu(001) grows layer-by-layer except for the first 2 ML [76, 102]. As soon as a layer is completed, islands form in the next layer until they coalesce to form a complete layer again. This means that the film morphology periodically changes from "flat" corresponding to a complete layer to "rough" for an incomplete surface layer. Therefore, the Co roughness

oscillates with a period of 1 ML. The 1 ML Co period of the ripple-like modulation of the phase coupling in FeNi/FeMn/Co trilayers demonstrates clearly the connection to the roughness of the Co layer.

In Fig. 3.9 (a), page 43, the interlayer coupling between Co layers is antiferromagnetic (AFM) for an even nominal number of $Fe_{50}Mn_{50}$ monolayers and a Co bottom layer thickness of 8.0 ML. The term nominal (t_{AFM}) defines the actually deposited amount of $Fe_{50}Mn_{50}$ as determined, for instance, from RHEED. Increasing the thickness of the Co bottom layer, for example, from 8.0 to 8.5 ML, while the $Fe_{50}Mn_{50}$ thickness is maintained constant at 14.0 ML, the interlayer coupling changes to ferromagnetic (FM).

Based on the layered antiferromagnetic structure of $Fe_{50}Mn_{50}$ the explanation for these observations could be that some amount of the AFM spacer layer is "lost" i.e., does not contribute to the interlayer magnetic coupling. The "saw-tooth" like shape modulation of the phase coupling as a function of Co layer thickness can then be understood qualitatively in a "filling model" as shown schematically in Fig. 5.1. The basic hypothesis of this model is that the amount of AFM material that is needed for completion of a filled FM layer is "lost" for the coupling. Three different panels correspond to different atomic layer filling of the Co bottom layer. t_{FM} denotes the thickness of the Co bottom layer, where n is an integer number, the number of completely filled Co layers. t_{AFM} defines the deposited amount of $Fe_{50}Mn_{50}$, while $t_{AFM,eff}$ corresponds to the AFM spacer layer thickness which effectively contributes to the coupling.

Let us start our discussion with the left–upper panel. For a Co thickness of $t_{FM} = (n+0.2)$ ML the effective thickness of $Fe_{50}Mn_{50}$ participating to the coupling is $t_{AFM,eff} = t_{AFM} - 0.8$ ML. It means that 0.8 ML, $Fe_{50}Mn_{50}$, the hatched area, is "lost", does not participate to the coupling. Upon increasing the submonolayer coverage of the Co layer to $t_{FM} = (n+0.5)$ ML the effective $Fe_{50}Mn_{50}$ thickness participating to the coupling is $t_{AFM,eff} = t_{AFM} - 0.5$ ML. In this case only 0.5 ML $Fe_{50}Mn_{50}$ is needed to fill the Co layer. For a higher submonolayer coverage of the Co layer, $t_{FM} = (n+0.8)$ ML, the amount of $Fe_{50}Mn_{50}$ which does not contribute to the coupling is only 0.2 ML. In all three panels, while the effective $Fe_{50}Mn_{50}$ thickness contributing to the coupling is constant, the "lost" $Fe_{50}Mn_{50}$ material is a function of the filling of the Co layer. The graph at the bottom of Fig. 5.1 shows schematically a line of constant effective $Fe_{50}Mn_{50}$ thickness participating to the coupling plotted in a (t_{AFM}, t_{FM}) coordinate system. Increasing the Co layer thickness from n filled layers to the next, (n+1) filled layers, the amount of $Fe_{50}Mn_{50}$ thickness "lost" for the magnetic coupling decreases linearly. For a full Co layer, $t_{FM} = (n+1)$ ML, an abrupt change of the $Fe_{50}Mn_{50}$ thickness not participating to the coupling is observed in that model. Regarded as a function of Co layer coverage, the effective $Fe_{50}Mn_{50}$ thickness participating to the coupling exhibits a "saw-tooth" like shape with an amplitude of 1 ML. However, the amplitude of the ripple-like structure as measured in Fig. 3.6 is only 0.3 ML and 0.5 ML in Fig. 3.9, much lower than the one from the simple "filling" model. This may suggest that the simple view of "holes" filled with $Fe_{50}Mn_{50}$ which do not participate to the
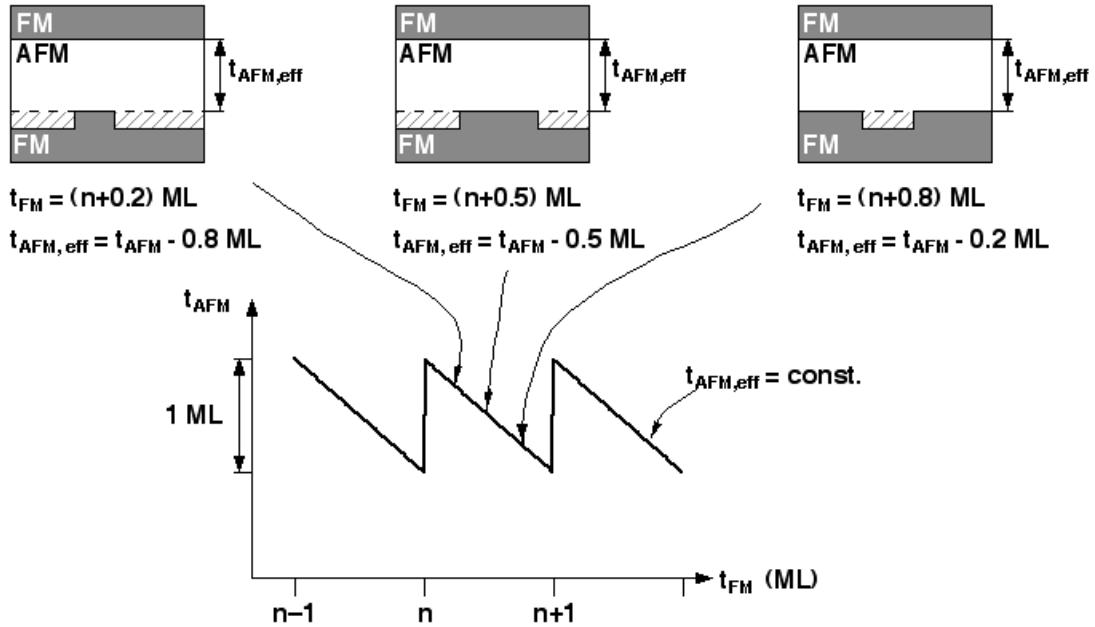
Figure 5.1: Schematic representation of the interlayer coupling as a function of submonolayer coverage of bottom Co layer thickness. Darker rectangles show the ferromagnetic layers labelled FM, and the Fe$_{50}$Mn$_{50}$ corresponds to the white spacer layer labelled AFM. The hatched area gives the amount of AFM material which does not contribute to the interlayer coupling. The graph at the bottom shows schematically the dependence of the Fe$_{50}$Mn$_{50}$ thickness (t_{AFM}) as a function of Co bottom layer coverage, for a constant effective AFM thickness ($t_{AFM,eff}$) contributing to the interlayer coupling.

coupling is not fully true. A backward look to the topography image of 5 ML Co on Cu(001), confirms that the layer-by-layer growth is not like the ideal case assumed in the present model. As can be seen in Fig. 2.3, page 28, before the completion of the 5th layer, some amount of deposited Co has already nucleated in the 6th layer. The point is that there are always holes which need some material to be filled (not the 6th layer islands). Perhaps, it will make more sense to define a critical minimum and maximum lateral dimension of the holes. Only the holes within this interval will act as a "loosing" AFM material centers.

In the sketch a t_{AFM} is chosen that leads to a smooth upper interface. This, however, does not limit the model to only the bottom interface. It is identically applicable also for other t_{AFM} if the same layer filling mechanism is assumed also for the top interface. The result will be a vertical shift (like an offset) of the "saw-tooth" like of the graph from Fig. 5.1.

The exact mechanism promoting the "loss" of AFM material is not known. Interface alloying could strongly influence the strength and phase of the coupling. Contradictory theoretical and experimental results have been reported on the Cr/Fe magnetic coupling. Heinrich *et al.* pointed out that the differences between the experimental results and the theoretical

predictions for the exchange coupling of Fe through a Cr(001) spacer layer can be caused by interface alloying [103]. Direct observation by means of scanning tunnelling spectroscopy of Cr intermixing with the Fe substrate was reported by Davies *et al.* [104]. After deposition of 1 ML Cr on Fe(001), only 10% of Cr remained in the surface layer, indicating that most of the Cr atoms have penetrated into the Fe substrate.

Theoretically, Freyss *et al.* [105] showed that the discrepancy between experiments and calculation can be accounted by the abrupt interface considered in the theoretical studies. In experiments, such perfect interfaces do not exist because of roughness or interdiffusion. For ideal Cr/Fe interfaces (without interdiffusion) the number of Fe–Cr first-neighbor bindings being for these concentrations smaller than the number of Cr–Cr first-neighbor bindings, the layer-by-layer antiferromagnetic structure of Cr prevails on the Fe–Cr antiferromagnetic coupling. When the diffused amount of Fe in Cr is larger than a certain value, the number of Fe–Cr first-neighbor bindings is no longer smaller than the Cr–Cr ones. The result is a change of the phase of the coupling.

Further the discussion is focused on the possible mechanisms that could favor interface alloying. For epitaxial layers the interface alloying is related to the surface free energies of substrate and adlayer. According to Bauer's criteria $\Delta\gamma = \gamma_a + \gamma_i - \gamma_s$ [106], the morphology of the interface between two epitaxial films is influenced by the interface energy (γ_i) and the surface free energies of substrate (γ_s) and adlayer (γ_a). Depending on the relation between the interface energy and surface free energies of substrate and adlayer, three growth modes are usually categorized: three-dimensional island growth ($\Delta\gamma > 0$), layer-by-layer growth ($\Delta\gamma \leq 0$ for each adlayer) and partial layer-by-layer growth with successive $3\,\mathrm{D}$ islanding ($\Delta\gamma \leq 0$ for a limited number of adlayers). Therefore, if γ_s is smaller than γ_a, the deposited material should follow the island growth mode. The islands, once formed, could lower their energy by alloying themselves with a thin skin of substrate material [107, 108].

Although simple thermodynamic arguments have been successful in explaining surface-alloy formation in many binary systems, recent studies reveal that the surface free energy arguments are inadequate for some cases [109]. Atomically and chemically resolved STM studies of epitaxial Mn growth on Fe an whisker revealed a diffusion of the Fe atoms through the first three Mn layers [110]. The Fe surface energy ($\gamma_{Fe} = 2.6\,\mathrm{J/m^2}$) is higher than the Mn surface energy ($\gamma_{Mn} = 1.6\,\mathrm{J/m^2}$), and from Bauer's criteria no interface intermixing should be expected. The driving forces for the surface-alloy formation have been attributed to their lattice mismatch [110]. The strain energy caused by the high lattice mismatch between Mn and Fe ($\approx 4\%$) plays the key role for the interface alloying. Besides these interface alloying mechanisms mentioned above there are some other experimental observations which claim a correlation between the presence of atomic steps and interface alloying.

Studies of Choi *et al.* [111] on the surface alloy formation of Fe on Cr(001) by means of STM showed that in the first stage the deposited Fe material is located at the Cr islands step

edges and there are no regions where they are nucleated on the terraces. It confirms that in fact alloying starts from step edges. The probability of atomic exchange near step edges is larger than at the flat interface because of a decrease of their coordination number. If steps or island edges may work as the reaction sites for incorporation of adatoms into the substrate, it might be reasonable to assume that a higher step density will give a higher intermixing at the interface.

STM investigations of Flores *et al.* [112] of the growth mechanism of Mn on Cu(001) revealed that the incorporated Mn atoms are not distributed homogeneously. The density of Mn incorporation is higher at the island edges and in the vicinity of the substrate step edges. On the open terraces, far away from islands, practically no Mn was observed.

Experimental observations of Offi *et al.* [78, 81] reveal a clear dependence of the magnetic coupling on the interface between Fe$_{50}$Mn$_{50}$ and Co on Cu(001). While the Fe moments have always been found ferromagnetically coupled with respect to Co, different behavior has been observed for Mn. In some cases Mn moments have been found with a parallel orientation with the Co film magnetization, in some other cases antiparallel oriented. The above mentioned remarks clearly prove that the magnetic state of the Mn atoms is very sensitive to oxidation and to the magnetic environment. Indeed, contradictory results have been reported on the coupling of Mn on an Fe layer. Using scanning electron microscopy with polarization analysis (SEMPA), Tulchinsky *et al.* [12] observed a ferromagnetic coupling of the Mn surface moments at the Mn/Fe interface, for epitaxial growth of Mn on an Fe whisker as a substrate. Rader *et al.* [113], by means of X-ray magnetic circular dichroism, found evidence for an antiferromagnetic coupling of Mn to the Fe films grown on a separate substrate. Besides the lattice mismatch and surface energies, the morphology of the interface, i.e., surface roughness, plays a quite important role. The Fe whisker shows very large terraces, while an Fe film deposited on a substrate shows higher roughness, with a higher density of steps. This suggests that the magnetic state of the first Mn layer is highly sensitive to the exact structure of the Mn grown, which in turn depends on the quality of the underlaying Fe layer.

Theoretical studies of Stepanyuk *et al.* [114] for Mn impurities in Co showed that the antiferromagnetic configuration is more stable than the ferromagnetic one, but only by a small energy difference of $0.12\,\mathrm{eV}$. Hence, the competition between both states might be easily changed by a small structural perturbation.

A similar mechanism, enhancement of the alloying process at the step edges, might be also effective for the system under investigation, Fe$_{50}$Mn$_{50}$/Co. Going from a filled atomic layer to a half filled layer of Co, the density of step edges increases. The presence of the step edges for a half filled Co layer may induce a Co-enriched Fe$_{50}$Mn$_{50}$ interface layer. The absence of such step edges, or at least a lower density for a complete Co bottom layer, may lead to a Co impoverished Fe$_{50}$Mn$_{50}$ interface layer, which shows a different magnetic state as the former one.

The frustration of the interlayer coupling associated with the presence of interface roughness may be another possible mechanism behind the loosing of AFM material. Only the presence

of steps may already induce a topologically different environment for the interacting atoms at the interface. For a complete Co layer, the first neighbor Fe–Mn interactions prevail over Co–Mn and Co–Fe first neighbor interactions. For a half-filled Co bottom layer the higher Co–Mn and Co–Fe first neighbor interactions may overcome the Fe–Mn first neighbor interactions, inducing a different magnetic state. Previous XMCD measurements in absorption reported an antiparallel orientation of Mn magnetization to Fe in $Fe_{90}Mn_{10}$ alloy and parallel to Co in $Co_{90}Mn_{10}$ alloy [81]. This suggests that Mn tends to couple antiferromagnetically to Fe and ferromagnetically to Co, at least when alloying. Besides the first-neighbor interaction number, the strength of the interaction comes into play for such a bicomponent AFM material. Let us assume in a first approximation that the Fe–Co strength of coupling (J_{Fe-Co}) is stronger than Mn–Fe (J_{Mn-Fe}) which is stronger than Mn–Co (J_{Mn-Co}), $|J_{Fe-Co}| > |J_{Fe-Mn}| > |J_{Mn-Co}|$. For a full Co bottom layer a stronger J_{Fe-Co} will favor a parallel alignment of Fe and Co magnetizations while a stronger J_{Fe-Mn}, ($|J_{Fe-Mn}| > |J_{Mn-Co}|$), will favor an antiparallel orientation of Mn magnetization with respect to Co and Fe magnetizations. For a half-filled Co bottom layer surface, the frustration of the first neighbor interaction at the step edges comes into play. The stronger J_{Mn-Fe} compared to J_{Co-Mn} ($|J_{Fe-Mn}| > |J_{Mn-Co}|$) may be overridden by an enhancement of the first neighbor interactions. Hence, it may be that the Mn, Fe, and Co magnetizations are all oriented in the same direction.

5.2   Influence of roughness on the coupling strength

In Sec. 5.1 we have seen how the interface roughness influences the coupling phase in $FeNi/Fe_{50}Mn_{50}/Co$ trilayers on Cu(001). Here, I want first to focus on the dependence of the coupling strength on the Co bottom layer filling, measured in $Co/Fe_{50}Mn_{50}/Co$ trilayers on Cu(001). In the second part of this section, the presence of oscillatory coupling with two different periods seen in $Ni/Fe_{50}Mn_{50}/Ni$, Fig. 3.13, page 52 and its connection with interface roughness will be outlined.

In Fig. 3.9 (b), page 43, changing the Co bottom layer thickness from 8.0 ML to 8.5 ML, the maximum coupling strength for antiparallel coupling changes from 0.75 mJ/m^2 to 0.33 mJ/m^2. It reflects a strong dependence of the coupling on the presence of interface roughness. In accordance with Slonczewski's proximity model in the presence of interface roughness, eq. 1.4, page 11, the coupling energy is a weighted average of odd and even number of atomic monolayers of the spacer layer. Within this model, Pierce *et al.* have shown in Ref. [8] how the roughness can strongly influence the short period coupling strength. The normalized short period bilinear coupling $\overline{J}_s$ decreases from 1 for ideal surfaces to 0.014 for an interface roughness $\sigma_t = 1$ ML. A similar mechanism could be responsible for the decrease of the interlayer coupling measured in $Co/Fe_{50}Mn_{50}/Co$ trilayers. An 8.5 ML Co bottom layer filling has a higher roughness than a fully filled layer, 8.0 ML Co. In the light of the above discussed model, a higher roughness

gives a lower interlayer coupling. Hence, the result will be a stronger coupling for 8.0 ML Co as compared to the case of 8.5 ML Co bottom layer thickness.

Within the same model we have seen in Sec. 1.2 that the coupling angle between the ferromagnetic layers should depend on the interface roughness. For example, at 50% atomic layer filling there will be equal contributions from the odd and even monolayer thick regions. Therefore, from eq. 1.5, page 12, a $\theta = \frac{\pi}{2}$ (90°) coupling angle between ferromagnetic layers is expected. For samples prepared like wedges, where the thickness of the spacer layer varies continuously, we might expect regions where the averaged bilinear coupling $\overline{J}_1$ changes from positive to negative going through zero. In these regions, the biquadratic coupling can become larger than the averaged bilinear coupling ($|J_2| > |\overline{J}_1|$) and we might expect a non-collinear coupling between ferromagnetic layers. None of the magnetic domain images and MOKE loops (Fig. 3.6 and Fig. 3.7), however, show any evidence for such a 90° or other non-collinear coupling.

Perhaps, the absence of the biquadratic coupling can be related to the spin structure of $Fe_{50}Mn_{50}$. The out-of-plane spin component assumed in Sec. 3.3 and Sec 3.4 might be responsible for such a behavior. Slonckzewski's proximity model was defined for an AFM with an in-plane spin component of the antiferromagnetic spacer layer. When the regions of odd and even number of monolayers are equal, this system can lower its energy by a 90° coupling between ferromagnetic layers connected with a small modulation of the FM spins. For an antiferromagnetic layer with a non-collinear spin structure it might cost less energy to cant the spin component in the antiferromagnetic layer by a few degrees towards out-of-plane.

Comparing with the maximum coupling strength values estimated in other trilayer systems, such as in an Fe/Cr/Fe(001) ($J_1 = 0.89$ mJ/m^2) [115] or across Mn known as a strong AFM, in an Fe/Mn/Fe(001) ($J_1 = 2.6$ mJ/m^2) [116] the values obtained here can be regarded as reasonable, while mentioning that what is measured here is not the maximum coupling strength but the strength for two particular $Fe_{50}Mn_{50}$ thicknesses.

Now let us focus on the presence of oscillatory coupling with two different periods observed in Sec. 3.4 in Ni/$Fe_{50}Mn_{50}$/Ni. In the as-grown Ni/$Fe_{50}Mn_{50}$/Ni trilayers, Fig. 3.13, page 52, above 7 ML $Fe_{50}Mn_{50}$, an oscillatory out-of-plane change of the Ni magnetization direction with two different periods as a function of $Fe_{50}Mn_{50}$ has been observed. Annealing and cooling back to room temperature of the bottom Ni layer, before deposition of the further $Fe_{50}Mn_{50}$ and Ni layers, leads to a 2 ML $Fe_{50}Mn_{50}$ oscillation period, Fig. 3.14, page 54. The presence of only the short period oscillation in the annealed sample, which has a smoother interface, reveals clearly the influence of the roughness and the frustration of the coupling in the not-annealed sample.

Let us compare this with other results observed for the interlayer coupling across non-magnetic and antiferromagnetic spacer layers. In Fe/Cr/Fe(001) trilayers, two oscillatory coupling periods were observed [117]. For films grown at low temperatures, the coupling oscillates with a long period, of approximately 11 Å($\approx$ 6 ML). When the layers are grown at elevated temperatures on high quality substrates, an oscillatory coupling with a period of 2 ML was observed.

The latter is associated with oscillations in the exchange coupling which causes the magnetization to change with each additional atomic layer of the spacer. Whether or not the short-period oscillations are observed depends on the roughness of the interfaces. If the interfaces are rough on a lateral length scale much shorter than the length over which the ferromagnetic layers can change the magnetization direction, the interlayer coupling is frustrated. The coupling over large regions becomes the average of the coupling for several thicknesses. As a result the short-period oscillation is weakened much more than the long-period oscillation, as observed and discussed also in this work. Here, I stress that in Fe/Cr/Fe(001) trilayers the short period oscillations are seen only above 5 ML Cr. Morever, this seems to be a more generally valid observation for coupling across AFM layers [11]. It might be interesting to see what is going on with coupling across non-magnetic spacer layers.

Investigations of the interlayer coupling across nonmagnetic spacer layers revealed also two different periods of oscillations. In Fe/Au/Fe(001) trilayers two oscillation periods of 2.48 ML and 8.6 ML were reported, in agreement with theoretical calculations derived from the Au Fermi surface [118]. Similar to the previous case of interlayer coupling across AFM, also in this case the short period oscillation is smeared out by the presence of interface roughness. While the short period oscillatory coupling across AFM starts only above a certain thickness, for the case of non-magnetic spacer layers, these are present from the "beginning". For example in Fe/Au/Fe(001) trilayers the first AFM peak is seen at 2.5 ML Au thickness. The oscillatory coupling across non-magnetic spacer layers is understood, as described in Sec. 1.1, as mediated by the electrons in the spacer layer ("RKKY"). According to eq. 1.2, the RKKY type coupling strength shows a power law decrease as a function of spacer layer thickness. For example the measured coupling strength in Fe/Au/Fe decreases from 1 mJ/m^2 at 3 ML Au spacer layer thickness to about 0.12 mJ/m^2 for 11 ML Au thickness.

The RKKY type of coupling must not be restricted only to non-magnetic layers. This type of coupling is present also in AFM. However, in the latter case it competes with the stronger AFM intralayer exchange coupling. In 6 ML Co/13 ML Fe$_{50}$Mn$_{50}$/8.0 ML Co trilayers, the measured coupling strength was estimated to be 0.75 mJ/m^2, (cf. Fig. 3.9). A simple comparison with the RKKY coupling strength, for nearly the same spacer layer thickness ($\approx$ 11 ML), shows us a 3–6 times stronger coupling across AFM spacer layers. This leads to the conclusion that the AFM exchange coupling is stronger than the RKKY coupling strength. For rougher surfaces, the interlayer coupling across AFM layers may show long period oscillations which results from an RKKY mechanism. The short period oscillation in this case, associated with the AFM layered structure is cancelled out by the presence of surface roughness. In samples with an improved surface quality, only a two monolayers period oscillations will be present. Indeed, such a behavior was observed in Ni/Fe$_{50}$Mn$_{50}$/Ni (Fig. 3.13 and Fig. 3.14). For the not-annealed sample two periods of oscillation are present. The short period is present only above 7 ML Fe$_{50}$Mn$_{50}$. A closer look reveals an increase of the stripe width of the short period oscillation and a decrease

of the stripe width of the long period oscillation as a function of $Fe_{50}Mn_{50}$ thickness. Perhaps, this is the result of the power law decrease of the RKKY coupling strength as a function of spacer thickness.

5.3 Proximity effects

The goal of the present section is to discuss the concept of interlayer exchange coupling and the influence on the magnetic state of an antiferromagnetic material. When two different materials are brought into contact, the properties of one of them can be influenced by the presence of the adjoining material giving rise to so-called proximity effects. In the first part of this section's discussion the focus will be on the FM/AFM magnetic coupling and its influence on the ordering temperature (Néel temperature) of the AFM layer. A short overview of the ordering temperature in FM (AFM) layered systems precedes the discussion of the particular data presented in Chapter 3.

It is well known that the ordering temperature decreases as one of the physical dimensions of a system is reduced. Usually, the scaling of the critical Néel or Curie temperature is expressed for the case of an ideal three-dimensional Heisenberg system as [119]:

$$\frac{T_c(\infty) - T_c(t)}{T_c(\infty)} = bt^{-\lambda} \tag{5.1}$$

where $T_c(\infty)$ and $T_c(t)$ are the critical temperatures for an infinitely thick film and for a film of finite thickness t, respectively, b is a constant and λ is related to the critical exponent ν which describes the correlation length according to $\xi = \xi_o(|1 - \frac{T}{T_C}|)^{-\nu}$ by $\lambda = \frac{1}{\nu}$. $T_c(t)$ may be regarded as either the Curie or the Néel temperature, depending on the ordering of the system investigated. Scaling has been observed in the past for a number of thin magnetic films [120, 121].

For thinner films (in the monolayer range), surfaces and interfaces may affect the magnetic properties as Curie temperature, magnetic moments, and anisotropy. It has been experimentally demonstrated that a capping by Cu of an ultrathin Co or Ni film modifies the electronic structure via hybridization and reduces the Curie temperature [122, 123].

The opposite effect, i.e., a signature of a magnetic moment in a nonmagnetic material, was observed in easily polarizable materials, such as Pd and V, if they are brought into contact with a ferromagnetic material [124, 125].

By means of element selective X-ray magnetic circular dichroism (XMCD) it has been shown that the indirect exchange coupling between Co and Ni induces a significant enhancement of the Curie temperature of the Ni layer [126].

Within the mean field theory (MFT) for a ferromagnet, the interaction responsible for the ordering temperature is the intralayer exchange energy E_{intra} between two neighboring spins $\vec{S_i}$

and $\overrightarrow{S_j}$:

$$E_{intra} = -2J_{intra} \sum_{i,j} \overrightarrow{S}_i \cdot \overrightarrow{S}_j \tag{5.2}$$

In a trilayer, the interlayer exchange energy E_{inter} is given by eq. 1.1. In a first approximation, within the MFT for interlayer coupled films, the Curie temperature can be expressed as [127]:

$$T_C^* = \frac{1}{k_B}(\frac{2}{3}J_{intra}zS(S+1) + J_1\frac{\overrightarrow{M_1} \cdot \overrightarrow{M_2}}{M_1M_2}) \tag{5.3}$$

where z is the number of nearest neighbors, J_1 is the bilinear interlayer coupling and $\overrightarrow{M}_1$, $\overrightarrow{M}_2$ the magnetizations of the ferromagnetic layers. Consequently, from eq. 5.3, an enhancement of the ordering temperature might be expected for a periodic stack of ferromagnetic layers from the additional interlayer coupling energy. According to eq. 5.3, however, the increase of the Ni Curie temperature in Co/Cu/Ni trilayer films measured by Wilhelm *et al.* [126] would require an unrealistic high value for the interlayer coupling constant.

Theoretically Jensen *et al.* have shown that the experimentally observed increase of the Curie temperature in coupled Co/Cu/Ni trilayers could be obtained by taking into account magnetic fluctuations in the Ni films [128]. Generally, spin fluctuations induced for example by the thermal agitation diminish the magnetization of thin layers more strongly than for bulk magnets. An external magnetic field suppresses the action of these fluctuations, resulting in an increase of the magnetization value. In a similar way, for coupled films, the interlayer coupling reduces the fluctuation effects since it acts as an effective external magnetic field reducing the fluctuation effect.

In contrast to studies of the proximity effects on the properties of ferromagnetic films there has been a little experimental work on this effect for thin antiferromagnetic (AFM) layers. The absence of a net magnetic moment in AFM films precludes the use of measurement techniques involved in the studies of FM films. Parkin and Speriosu suggested that some properties of the AFM layer can be indirectly determined from those of the FM probe layer which can be more easily measured [129]. In their work the ordering temperature of FeMn layers has been associated with the presence of an exchange bias field in FeMn/FeNi bilayers. The exchange coupling at the interface between a FM and a AFM layer is manifest as a shift of the hysteresis loop along the applied field axis by the exchange field anisotropy. The loss of exchange anisotropy at 300 K for a thin FeMn layer with a thickness $t_{AFM} \leq 50\,\text{Å}$ has been related with a reduction of the Néel temperature of the FeMn layer from the bulk value. This type of behavior can be ascribed to finite-size scaling effects as the magnetic correlation length becomes bounded by the size of the system, as described by eq. 5.1. However, neutron diffraction measurements performed by van der Zaag *et al.* revealed a difference between the Néel temperature and the blocking temperature in ultrathin coupled AFM/FM bilayers [130]. By definition, the blocking temperature corresponds to the onset temperature of the exchange bias field. While the blocking

temperature of the thin films was observed to decrease with decreasing AFM thickness, the Néel temperature was approximately equal to the bulk value. Indeed, the proximity of an FM layer induces an increase of the Néel temperature of the AFM layer in ultrathin films. For the epitaxial bilayer growth of FeMn/Co, Kuch *et al.* [15] have reported the transition of FeMn from paramagnetic to antiferromagnetic at 300 K at a thickness of 10 ML FeMn ($\simeq 18\,\text{Å}$), a much lower thickness than predicted by Parkin and Speriosu for sputter-deposited FeMn [15]. For the deposition of thin Cr films on an Fe(001) substrate, Unguris *et al.* observed a periodical change of the direction of the surface moment with each additional Cr layer, showing that the Cr is antiferromagnetically ordered well above the bulk Néel temperature [20]. The increase of the Néel temperature for Cr/Fe bilayers with decreasing Cr thickness has been understood within the proximity magnetism model [131]. The Fe layers with a much higher ordering temperature T_C than the Cr polarize the Cr atoms near the Fe/Cr interface and induce a magnetic order which will not exist otherwise.

Despite of the huge interest in antiferromagnetic materials, no experimental reports are available up to now on the change of the ordering temperature of an AFM layer when sandwiched between two FM layers. The direct FM/AFM exchange coupling present in trilayers at both interfaces, the bottom and the upper one, may induce a further increase of the ordering (Néel) temperature as compared with bilayer case.

As presented in Sec. 3.2, page 38, for $Fe_{50}Mn_{50}$ sandwiched in between two FM layers, Co and FeNi, the transition in AFM from paramagnetism to antiferromagnetism at room temperature starts at about 6 ML $Fe_{50}Mn_{50}$, much lower than for bilayer $Co/Fe_{50}Mn_{50}(\simeq 10\,\text{ML})$ [15]. While the transition thickness is different, qualitatively the same behavior was observed for $Ni/Fe_{50}Mn_{50}/Co$ and $Ni/Fe_{50}Mn_{50}/Ni$ epitaxial trilayers (Sec. 3.3 and Sec. 3.4). Hence, when sandwiched in between two FM layers, $Fe_{50}Mn_{50}$ shows a strong increase of the Néel temperature, corresponding to a decrease of the thickness where $Fe_{50}Mn_{50}$ becomes AFM at room temperature. The increase of the Néel temperature for AFM ultrathin films sandwiched in between two FM layers might be understood within the proximity magnetism model. In bilayers the direct FM/AFM exchange coupling induces an ordered state in the AFM near the interface. As we cover the AFM/FM bilayer with a second FM layer, an induced ordered state at the upper AFM interface can be expected. The result is a decrease of the thickness value where the AFM changes to an ordered state, which is equivalent with an increase of the Néel temperature. The spin structure of $Fe_{50}Mn_{50}$ is discussed in detail in the next section.

5.4 Spin structure of $Fe_{50}Mn_{50}$

Let us now pass on to the discussion of the experimental results from Sec. 3.3 and Sec. 3.4 on the interlayer coupling in $Ni/Fe_{50}Mn_{50}/Ni$ and $Ni/Fe_{50}Mn_{50}/Co$ trilayers on Cu(001). In Fig. 3.7, page 41, small domains distributed into faint stripes were observed in Ni for an $Fe_{50}Mn_{50}$ thickness above 7 ML, in an epitaxial $Ni/Fe_{50}Mn_{50}/Co$ trilayer. Deposition of 3 ML Co as a continuous film on top induces a spin-reorientation-transition in Ni from out-of-plane to in plane cumulated with the presence of 2 ML period of oscillation as a function of $Fe_{50}Mn_{50}$ thickness, Fig. 3.12, page 49. Morever, in Fig. 3.13, page 52, in $Ni/Fe_{50}Mn_{50}/Ni$ trilayer, the top Ni layer shows a periodical change of magnetization direction with 2 ML $Fe_{50}Mn_{50}$ thickness without any evidence of small domains.

The different behavior seen in the top Ni layer in $Ni/Fe_{50}Mn_{50}/Co$ and $Ni/Fe_{50}Mn_{50}/Ni$ trilayers before and after deposition of the top Co layer comes from a non-collinear spin structure of $Fe_{50}Mn_{50}$ spacer layer. As has been mentioned in Sec. 3.4, small domains do not occur in trilayers with identical anisotropy of both ferromagnetic layers. The presence of small domains in the top ferromagnetic layer in trilayers with different anisotropy shows that the perpendicular spin component behaves independently, as if the bottom ferromagnetic layer was not present. If the $Fe_{50}Mn_{50}$ is deposited onto an in-plane magnetized Co film, it is the out-of-plane component of the $Fe_{50}Mn_{50}$ spins which is not ordered by the Co bottom layer and gives rise to small out-of-plane domains in the top Ni layer (Fig. 3.10). In the case of $Fe_{50}Mn_{50}$ being deposited onto an out-of-plane magnetized Ni layer, the in-plane component of the $Fe_{50}Mn_{50}$ spins is laterally statistically fluctuating, leading to small in-plane domains after capping the top Ni layer by Co (Fig. 3.15). Therefore, a non-collinear spin structure has to be considered.

Indeed, the exchange interaction between the compensated interface of AFM FeMn and FM Co, was demonstrated to play an important role in determining the magnetic structure of AFM FeMn [78]. In $Fe_{50}Mn_{50}/Co$ system both the shape anisotropy and the strong in-plane magnetocrystalline anisotropy of Co could force the AFM spins to lie in the film plane. The influence of a FM layer on the AFM spin structure has been observed experimentally on the (001) surface of NiO. Using PEEM combined with X-ray magnetic linear dichroism (XMLD), Ohldag *et al.* have shown that after the Co deposition on AFM NiO(001), the AFM spins at the surface reorient and align domain by domain, parallel and antiparallel to Co spins [16].

So far contradictory theoretical and experimental models of magnetic structures in disordered bulk FeMn have been proposed: a collinear AFM (1 Q) structure and two noncollinear 2 Q and 3 Q structures, shown in Fig. 5.2. Originally, Kouvel and Kasper first detected long-range AFM magnetic ordering by neutron-diffraction measurements, and found that either the collinear 1 Q or noncollinear 3 Q structure could explain the experimental data [132]. Later, by means of neutron diffraction experiments, Umebayashi and Ishikawa determined a magnetic phase diagram in a whole composition range of $Fe_{1-x}Mn_x$ and proposed the $\langle 111 \rangle$ (3 Q) spin
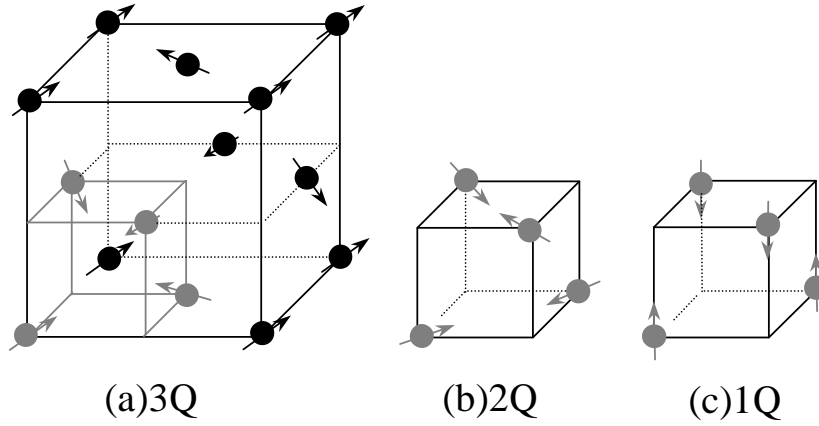
Figure 5.2: Schematic of the magnetic structures of disorder Fe$_{50}$Mn$_{50}$: (a) non-collinear 3 Q , (b) non-collinear 2 Q and (c) 1 Q collinear spin configurations . Small spheres with arrows indicate the spin directions.

structure for Fe$_{50}$Mn$_{50}$ [133]. Within this model, the magnetic unit cell coincides with the cubic unit cell, which thus comprises four magnetically distinct atoms. The magnetic moments on these four atoms, which form a tetrahedron, are directed towards the center of this tetrahedron. Fig. 5.2 (a) and (b) schematically show the 3 Q and 2 Q non-collinear spin structures of disordered Fe$_{50}$Mn$_{50}$, respectively. The 1 Q collinear spin structure of Fe$_{50}$Mn$_{50}$ is given in Fig. 5.2 (c) where the antiferromagnetically coupled spins are distributed in vertical planes.

From the theoretical point of view, using the linearized muffin-tin orbital (LMTO) method, Spišák and Hafner reported that the presence of disorder stabilizes 1 Q nearly ideal collinear layered AFM spin structure [134]. There are other theoretical calculations which find a 3 Q non-collinear spin structure as the energetically most favorable [135]. Moreover, the difference in the total energy between the two spin structures has been calculated to be rather small, so that any small imbalance could favor one or the other spin structure.

The above experimental observations on Ni/Fe$_{50}$Mn$_{50}$/Ni and Ni/Fe$_{50}$Mn$_{50}$/Co trilayers can be understood in a model with a non-collinear spin structure of the AFM, one component of which becomes influenced by the proximity of the FM layer with an EA either in-plane or out-of-plane. Fig. 5.3 and Fig. 5.4 show such an idealized spin structure model proposed for Fe$_{50}$Mn$_{50}$ sandwiched in between Co and Ni, and two Ni layers respectively. When Fe$_{50}$Mn$_{50}$ is deposited on top of the Co, the in-plane component of Co magnetization pins the in-plane spin component of Fe$_{50}$Mn$_{50}$ by direct exchange coupling while the out-of-plane spin component is "free". The term "free" has to be understood as free to have locally any of the out-of-plane directions, pointing either upward or downward. Fig. 5.3 (a) shows such an idealized spin structure model for Fe$_{50}$Mn$_{50}$. The in-plane spin component, which changes direction with each atomic layer, is drawn by small black arrows. The out-of-plane spin component of Fe$_{50}$Mn$_{50}$ is drawn by
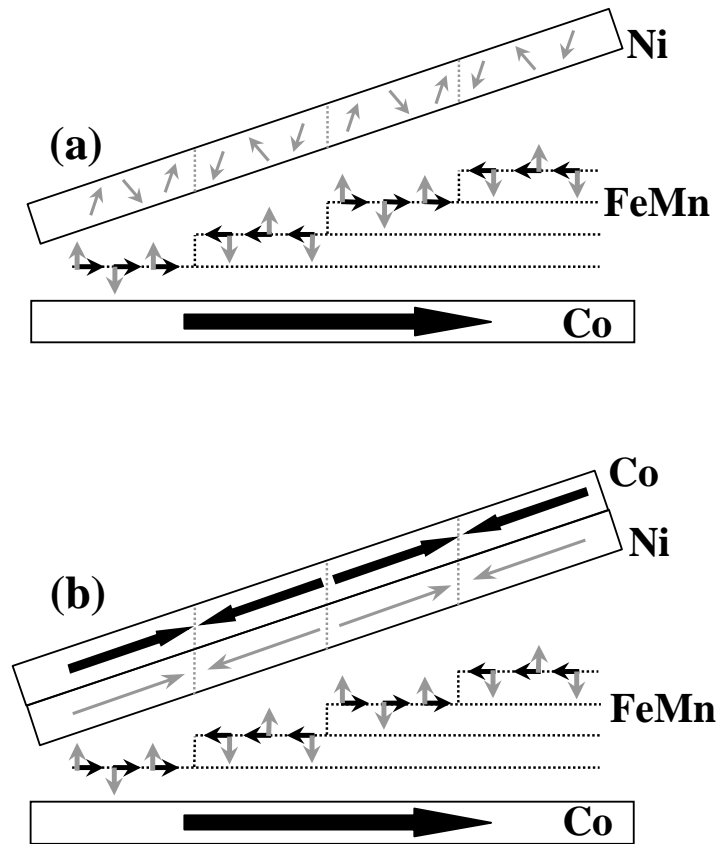
Figure 5.3: (a) Schematic representation of an ideal spin structure of $Fe_{50}Mn_{50}$ sandwiched in between Co with an in-plane magnetization direction and Ni with an out-of-plane magnetization direction. Small arrows of two different gray scale show the in-plane and out-of-plane spin components in $Fe_{50}Mn_{50}$. The brighter arrows in the Ni layer reflect the spatially fluctuating pinning of the out-of-plane component of magnetization, correlated with the out-of-plane spin component of $Fe_{50}Mn_{50}$. (b) Deposition of 3 ML Co on top of the same sample induces a spin-reorientation transition in Ni from out-of-plane to in-plane.

brighter small arrows. The spin structure has to be thought extended to the right along the dotted lines for each layer. The displayed periodic downward-upward distribution of the out-of-plane spin component is a simplified case which does not limit the applicability of the model. However, it will make more sense to regard each arrow as a spin conglomerate. The intermixing upward-downward of the out-of-plane spin component of $Fe_{50}Mn_{50}$ could be dictated by the presence of uncompensated moments at surface defects, such as monoatomic steps, terminating the regular AF spin structure. The 15 ML Ni deposited on top of $Fe_{50}Mn_{50}/Co/Cu(001)$ will "replicate" the randomly distributed out-of-plane spin component of $Fe_{50}Mn_{50}$. Deposition of 3 ML Co as a continuous film on top, Fig. 3.11, page 47, induces a spin-reorientation-transition (SRT) of Ni from out-of-plane to in-plane and a merge of the small domains. The 2 ML period

of oscillation as a function of Fe$_{50}$Mn$_{50}$ observed in Ni is regarded as an indication of the in-plane spin component in the Fe$_{50}$Mn$_{50}$. It is the in-plane spin component of Fe$_{50}$Mn$_{50}$ which imposes the direction of the in-plane (SRT) in Ni. The color code used in drawing the arrows in Fig. 5.3 (a) was chosen to reflect the physics behind. The black arrow in the Co bottom layer pins the in-plane spin component of Fe$_{50}$Mn$_{50}$ which correlates with the direction of magnetization of the Co upper layer. The out-of-plane spin component in Fe$_{50}$Mn$_{50}$ and the Ni magnetization, correlated as presented above, are drawn by brighter arrows.
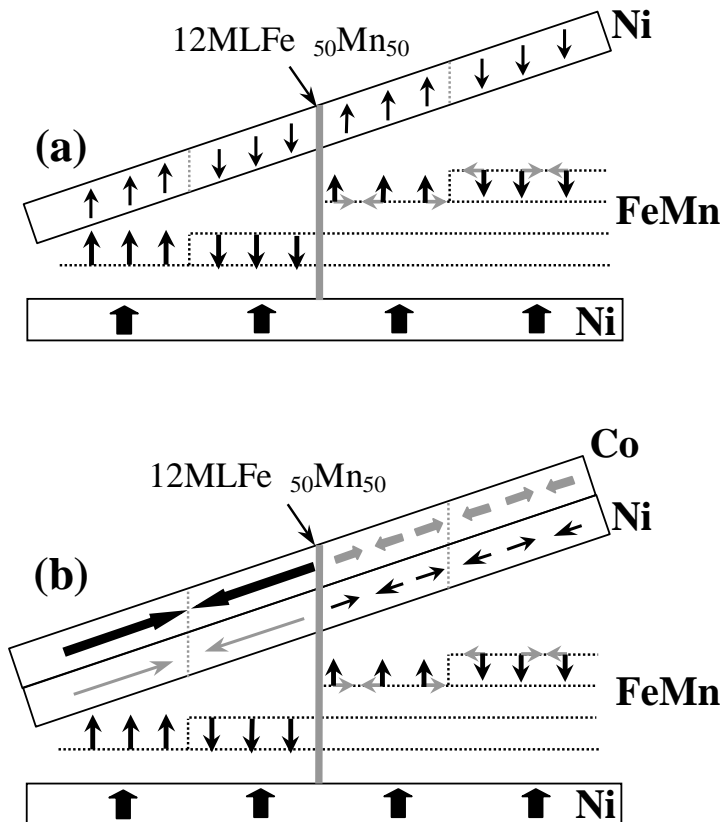
Figure 5.4: (a) Schematic representation of an idealized non-collinear spin structure of Fe$_{50}$Mn$_{50}$ sandwiched in between two Ni layers with an out-of-plane magnetization direction. Small arrows of different gray scale show the in-plane and out-of-plane spin components in Fe$_{50}$Mn$_{50}$. Above 12 ML, besides the out-of-plane spin component Fe$_{50}$Mn$_{50}$ develops an in-plane spin component randomly distributed. (b) Deposition of more than 0.5 ML Co on top induces a SRT transition in Ni from out-of-plane to in-plane. An oscillatory coupling is seen below 12 ML Fe$_{50}$Mn$_{50}$, while above this thickness small domains are formed in the upper Ni and Co layers.

In Fig. 3.15, page 55, the striking observations are the appearance of small domains, with in-plane magnetization, after deposition of the top Co layer on the Ni/Fe$_{50}$Mn$_{50}$/Ni trilayer, above 12 ML Fe$_{50}$Mn$_{50}$ thickness. There are at least two explanations that could mitigate for

such a shifting of the transition line to higher thickness. The first one could be associated with a slightly deviation of the alloy composition from the $50 - 50$ stoichiometry. For example an enhanced Fe composition will lead to a decrease of the Néel temperature. This implies an increase of the thickness where the $Fe_{50}Mn_{50}$ changes from paramagnetic to antiferromagnetic. The presence of the small domains in the top FM layer indicates an antiferromagnetic order of the $Fe_{50}Mn_{50}$ [15]. The spatially fluctuating direction of the spin directions of $Fe_{50}Mn_{50}$ acts as pinning centers at the upper $Ni/Fe_{50}Mn_{50}$ favoring the presence of the small domains. A closer look to the Ni and Co images in Fig. 3.15, page 55, reveals the presence of different domain shapes as a function of the $Fe_{50}Mn_{50}$ thickness. Below 7 ML $Fe_{50}Mn_{50}$, the thickness at which $Fe_{50}Mn_{50}$ was assumed to change from paramagnetic to antiferromagnetic, relatively small domains are formed after deposition of the top Co layer. Between 7 ML and 12 ML $Fe_{50}Mn_{50}$, a nearly regular 2 ML $Fe_{50}Mn_{50}$ thickness oscillatory change of the Ni magnetization is observed. Smaller domains are formed in Ni above 12 ML $Fe_{50}Mn_{50}$. Quantifying the above observations, it might be that the spin structure of $Fe_{50}Mn_{50}$ in $Ni/Fe_{50}Mn_{50}/Ni$ trilayer is different, below and above 12 ML $Fe_{50}Mn_{50}$.

The results for the $Ni/Fe_{50}Mn_{50}/Ni$ trilayer could be understood within a similar model. However, the presence of small domains in Co for a thickness above 12 ML $Fe_{50}Mn_{50}$ reflects different spin structures of the AFM spacer layer above and bellow that thickness. A collinear spin structure below 12 ML $Fe_{50}Mn_{50}$ and a non-collinear spin structure above this thickness may be present. It might be that the stronger interlayer coupling in between Ni layers induces in thinner $Fe_{50}Mn_{50}$ a collinear spin structure similar to the 1 Q spin structure discussed above. Increasing the $Fe_{50}Mn_{50}$ thickness, the anisotropy of the AFM layer increases and competes with the interlayer coupling strength imposing a change of the $Fe_{50}Mn_{50}$ spin structure to a non-collinear configuration. Fig. 5.4 (a) shows such an idealized spin-structure model proposed for the case of $Fe_{50}Mn_{50}$ sandwiched in between two Ni layers with an out-of-plane direction of magnetization. The transition line in between the two spin structures in $Fe_{50}Mn_{50}$ is marked by a thick gray vertical line in Fig. 5.4. When deposited on 15 ML Ni, the out-of-plane spin component of $Fe_{50}Mn_{50}$ is fixed in the vertical plane through the exchange coupling to the Ni layer. Above 12 ML, besides the out-of-plane spin component, $Fe_{50}Mn_{50}$ could develop an in-plane spin component, randomly oriented. The different spin structure of $Fe_{50}Mn_{50}$, a collinear and a non-collinear, are reflected in different domain structures in the upper Co layer deposited as a wedge. A thickness of the upper Co layer $t_{Co} \geq 0.5 \, ML$ induces a SRT of Ni from out-of-plane to in-plane. A periodic change of the Ni top layer is seen below 12 ML $Fe_{50}Mn_{50}$ while above small domains are formed in Ni and upper Co layer. Hence, the transition to the non-collinear spin structure of $Fe_{50}Mn_{50}$ is associated with small domains in the upper Co layer.

The presented experimental results provide evidence for the presence of a non-collinear spin structure of $Fe_{50}Mn_{50}$. While in the case of $Ni/Fe_{50}Mn_{50}/Co$ trilayer a non-collinear spin structure was more favorable, for $Ni/Fe_{50}Mn_{50}/Ni$ trilayer a transition from a collinear to a non-

collinear spin structure could explain the experimental results. Although statements about the exact spin structure and the size of the AFM spin component perpendicular to the FM pinning direction would require further experiments. It remains to be seen whether the compositional disorder, as observed in Sec 3.1, is a necessary ingredient for such a non-collinear spin structure in ultrathin films.

5.5 Coupling by domain wall stray fields

As presented in Chapter 4, if a magnetically soft layer interacts with a magnetically harder film showing a domain structure, this domain structure will influence the soft layer not only by the locally different coupling directions associated with the different domains, but in addition also by magnetostatic interaction of the domain walls. This has been studied here particularly for the case of coupling across Cu, between an FeNi alloy layer and a Co layer pinned to an antiferromagnetic FeMn layer. The magnetization of the soft layer located above the domain walls of the hard layer is locked-in by the stray field of the domain walls, and therefore higher fields are needed in order to fully saturate the soft layer. This was shown in Fig. 4.4, page 62. A closer look to these unreversed regions located above the Co domain walls reveals a spike-like shape. After an external magnetic field of 340 Oe had been applied as shown by the arrow, the Fe image, Fig. 4.2 (e), page 60, reveals the presence of small bright domains located above the Co domain walls that have not changed their magnetization direction. Morever, these are interrupted by darker regions where the FeNi layer has reversed the magnetization direction. The distance measured in Fig. 4.2 (e) between the unreversed domains is of about 5 μm while the linear diameter of these domains is about 2 μm. For an external field of –340 Oe applied in an opposite direction, the unreversed domains located above the Co domain walls appear darker but the discontinuous distribution along the walls is conserved. Such a behavior leads
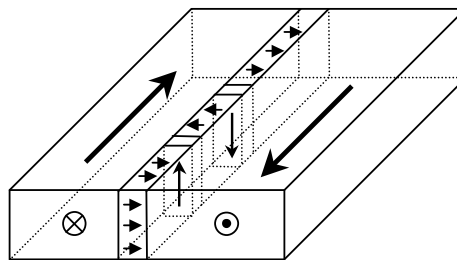
Figure 5.5: Schematic three-dimensional view of a Néel domain wall consisting of segments of opposite rotation sense of the magnetization within the wall.

to assume a hypothetical micromagnetic structure of the Co Néel walls, as shown in Fig. 5.5.

In a Néel domain wall, the magnetization rotates about an axis perpendicular to the plane of the film (cf. Fig. 1.4, page 13. Instead of an identical sense of rotation along the wall, the Néel wall of 15 ML Co/15 ML FeMn could consist of segments of opposite magnetization in the plane, perpendicular to the wall. In Fig. 5.5 three such segments are displayed. Probably, these segments have formed in an attempt to mix the north and south poles on the wall surface more intimately and thus reduce the magnetostatic energy. When following the orientation of the stray fields along the wall, Fig. 5.5, from bottom to top there are positions where the stray field is oriented from left to the right, separated by regions where the stray field is oriented into the opposite direction. The regions within the wall with opposite polarity are separated by singularities where the magnetization is normal to the film plane, the so-called Bloch lines. The stray fields of the latter are normal to the film surface. Within the above hypothesis, the "unreversable" small domains in the FeNi layer, located above the Co domains and observed in Sec. 4.1, could be understood as pinned by the stray fields of such segments following the change of the orientation of the stray field along the domain wall in the Co layer. The stray field of each domain wall segment can either increase or decrease the effective field seen by the soft layer depending on its orientation with respect to the applied field. Hence, the spike-like shape of the "unreversable" domains in the soft layer may reflect the local distribution of the domain wall stray field of Co along (or opposite) to the external applied field.

Now, let us focus on the experimental results presented in Sec. 4.2., for Co/Cu/Ni trilayers. Besides a duplication of the Ni domain pattern in the Co layer, it was observed that the Co domains are slightly shifted with respect to the Ni domains. In films with an easy axis of magnetization oriented out-of-plane, a supplementary stray field arises from the presence of magnetic surface charges.

In order to verify the stray field type origin of the observed domain wall displacement, the simple analytical calculation of the stray field in the 1–D case from Ref. [136] is used. The stray field above a domain wall of zero width in a film of thickness t, for a periodic out-of-plane stripe domain pattern of width w, for a height z above the sample surface is given by:

$$H_z(x) = 4M_s[atanh(\frac{cos(\frac{\pi x}{w})}{sin(\frac{\pi z}{w})}) - atanh(\frac{cos(\frac{\pi x}{w})}{sin(\frac{\pi(z+t)}{w})})] \tag{5.4}$$

Fig. 5.6 shows a plot of the domain wall stray field using the analytical formula (5.4) for a thin film with perpendicular magnetization, and $w = 50$ μm, at a height of $z = 1.28$ nm and $t = 10$ nm. The maximum stray field value is localized above the domain wall and is a function of the domain width. The analytically calculated value for a Ni domain wall of zero thickness, yields nearly a value of 2000 Oe in the center of the Co layer position, i.e., 1.2 nm above the Ni surface. By micromagnetic calculations using the Landau-Lifshitz-Gilbert equation, Kuch et $al.$ have calculated a maximum value of the domain wall stray field of 480 Oe at the same height above the Ni film [137]. This is distinctly higher than the experimental estimate of 250 Oe,
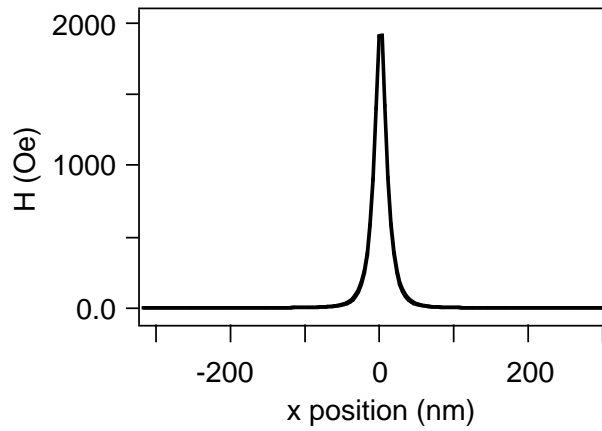
Figure 5.6: Calculated stray field value for a 1–D pattern with perpendicular magnetization. Domain width $w = 50$ μm, height above the film surface $z = 1.2$ nm.

but much lower than the analytically calculated value using eq. 5.4. The lower value has been related to the finite extension of the Ni domain wall and also to a deviation from the ideal Bloch profile induced by the interlayer exchange coupling to the Co layer. In Fig. 5.7 is schematically indicated the wall structure in a film with an out-of-plane direction of magnetization. The distribution of magnetization within the wall is strongly influenced by the x component of the domain wall stray field plus the influence of the Co layer as explained below. The interesting
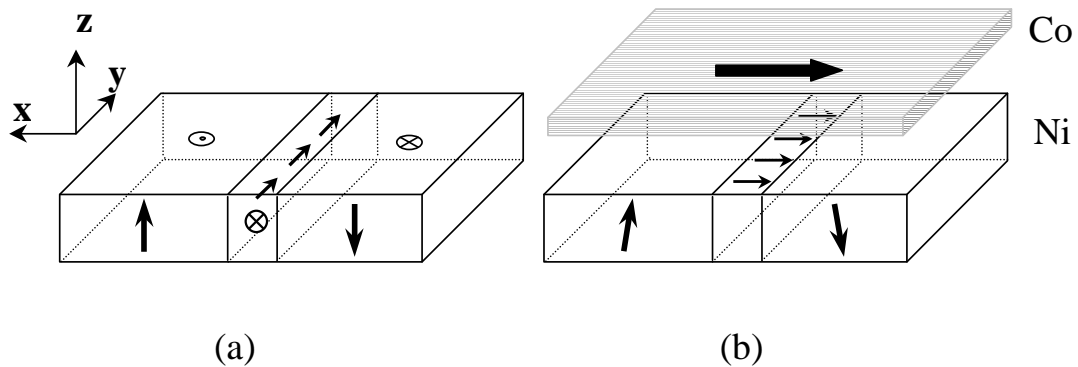
Figure 5.7: (a) Schematics of the wall structure of the single Ni layer with an out-of-plane direction of magnetization; (b) Schematics of the wall structure of the Ni layer in Co/Cu/Ni trilayer. The distribution of Ni magnetization within the wall turns from $+z$ to $-x$ to $-z$, and not, as in a Bloch wall of the single Ni layer, from $+z$ to $+y$ to $-z$.

point observed by Kuch *et al.* [137] is the reaction of the Ni layer to the coupling with the Co layer. The domain wall stray field induces an x component in the Co magnetization direction above the Ni domain walls. The presence of an x component of the Co magnetization at the

positions of the Ni domain walls distorts the Bloch wall in the Ni. The azimuthal angle of the in-plane component of the Ni magnetization follows closely the corresponding angle of the Co magnetization, even in the domain walls. This means that at –200 Oe external field the Ni magnetization turns from $+z$ to $-x$ to $-z$, and not, as in a Bloch wall, from $+z$ to $+y$ or $-y$ to $-z$. This adds additional magnetic charge to the wall, which decreases its stray field. On the other hand, if the magnetization in the wall is turning by $+x$, the stray field is increased, because the contribution due to the in-plane magnetization in the wall and the contribution due to the out-of-plane magnetization in the domains outside the wall partially cancel each other. Therefore the maximum value of the stray field for zero external field is influenced by partial charging of the Ni wall.

The experimentally observed extension of the Co domains induced by the Ni stray fields, i.e., the shift of the Co domains with respect to the Ni domains, depends on the details of the magnetization reversal mechanism in the Co layer, for example domain wall mobility and pinning, and on the energetics of all involved mechanisms, including some preferential coupling that locally links a certain Co in-plane and a Ni out-of-plane magnetization direction, as will be discussed below, and a possible local uniaxial in-plane anisotropy. The larger domain shift observed after the application of the 240 Oe field pulse compared to the as-grown state (Fig. 4.8, page 68) is an indication that the latter represents a metastable configuration. In fact the energetically most favorable remanent configuration would be a shift of the Co domains by half the stripe period of the Ni domains. At some of the narrower stripe domains in Fig. 4.7 (d), page 67, this situation seems to be indeed approximately realized.

The Ni domain wall stray field acts like a local effective field during growth of the Co layer. It will influence the critical thickness for ferromagnetic order in the Co layer, i.e., the thickness at which the ordering temperature equals room temperature. An external magnetic field suppresses magnetic fluctuations, resulting in a smaller critical thickness [128]. That means that during growth of the Co layer, ferromagnetic order will first be established at positions close to Ni domain walls due to the domain wall stray fields. At these positions the Co magnetization direction will be set by the direction of the stray field. It has been observed that very thin Co layers on top of 4 ML Cu/15 ML Ni/Cu(001) exhibit an out-of-plane magnetization with a domain pattern identical to the Ni domain pattern [138]. This out-of-plane magnetization of the Co layer has been attributed to the indirect exchange coupling between the Co and the Ni layer and to the vanishing anisotropy of the Co layer at thickness below 2 ML. The Cu thickness of the trilayers presented here is slightly higher, but it might be possible that also here an out-of-plane magnetization is present during the early stages of growth of the Co layer. The history of the Co magnetization during the layer deposition starts therefore from an out-of-plane domain pattern which is a replica of the Ni domain pattern, and later undergoes a spin reorientation transition to the in-plane domain pattern that is observed in the experiment after completion of the growth. One could imagine that during that spin-reorientation-transition the

local magnetization may turn into any of the four equivalent $\langle 110 \rangle$ in-plane crystallographic directions, thus loosing the information about the out-of-plane domain pattern. However, in the experiment a stunning similarity between the domain patterns of the in-plane Co magnetization and the out-of-plane Ni magnetization is observed, especially in Fig. 4.7, page 67. Possible mechanisms leading to this domain pattern correlation may be found in the exact mechanism of the spin reorientation transition of the Co layer from out-of-plane to in-plane. In Ref. [138] no sign of branching into small domains of the out-of-plane domains towards the spin reorientation transition is observed, as it is found sometimes in the vicinity of spin reorientation transitions [139, 140]. The spin reorientation transition may therefore proceed, domain by domain, by a continuous rotation of the magnetization from out-of-plane to in-plane. In this case it would be energetically unfavorable to create additional in-plane sub-domains. Which of the four equivalent in-plane directions are assumed in each domain may then depend on the subtle energy differences. Such energy differences could be due to structural details, for example preferential step edge orientation. In Fig. 4.6 it is in fact observed that locally the Co magnetization is rotated by the same $90°$ with respect to the Ni magnetization, leading to one of the two correlation patterns schematically shown in the figure. A breaking of the fourfold substrate symmetry by a local preferential substrate step edge and terrace orientation may be a conceivable explanation. The local stray fields present at the Ni domain walls may of course also influence the Co domain pattern formed after the Co magnetization has turned to in-plane. Further experimental effort is required to identify the exact mechanism responsible for that domain correlation.

The small Co domains seen in Fig. 4.6 (b), page 65, are absent in Fig. 4.7 (b), page 67. Magnetic domains of two different lengthscales in Co/Cu(001) at different positions on the sample have been already reported previously [141]. It is at present not clear which mechanism determines the Co domain size. Tiny differences in substrate morphology may be responsible. The absence or a reduced importance of the above discussed mechanism for domain correlation, for example a more isotropic step edge distribution, may also lead to a breaking into smaller in-plane domains of the Co magnetization.

From Fig. 4.7, page 67 one can see that the coercivity of the Co layer is not exactly uniform over the imaged area: from panels (d) and (f) it is clearly recognized that in both images stronger changes to the Co domain pattern occur in the upper left part of the image compared to the lower right part. Since the coils used for the external field are about 2 cm away from the sample, non-uniformity of the field can not be the reason for that. The coercivity is probably also influenced by details of the film and substrate morphology, which may change on a shorter lengthscale within the field of view.

Summary and conclusions

The interlayer magnetic coupling between two ferromagnetic layers (FM) across an antiferro-magnetic (AFM) or a nonmagnetic spacer layer, epitaxially grown on Cu(001), has been studied in this work. As FM layers were used Co, FeNi which show an in-plane EA magnetization direction and Ni with an out-of-plane EA magnetization direction in a certain thickness regime. As an AFM layer was chosen $Fe_{50}Mn_{50}$, and Cu as a nonmagnetic spacer layer. The layer-by-layer growth of Co, Ni, FeNi and $Fe_{50}Mn_{50}$ has been deduced from the presence of MEED/RHEED oscillation aqcuired during deposition. In particular for $Fe_{50}Mn_{50}$, the surface morphology has been studied by scanning tunnelling miscroscopy (STM). The magnetic properties have been measured by magneto-optic Kerr effect and by imaging magnetic domains, using a photoelec-tron emission microscope (PEEM) with X–ray magnetic circular dichroism (XMCD) as magnetic contrast mechanism. The following main results have been obtained:

- The presence of oscillations in the RHEED curves acquired during deposition of $Fe_{50}Mn_{50}$ on Cu(001) indicate an epitaxial layer-by-layer growth. STM images show large and flat terraces, with very small holes ($\approx$ 5 nm) of one atomic layer depth. In addition a fine structure with an apparent corrugation height of about 0.5 Å is recognized. Scanning tunnelling spectroscopy (STS) measurements prove the spectroscopic origin of this cor-rugation. The presence of this fine structure may be associated with local concentration differences of the constituents of the chemically disordered $Fe_{50}Mn_{50}$ alloy.

- The magnetic interlayer coupling in FeNi/$Fe_{50}Mn_{50}$/Co trilayers on Cu(001) shows dif-ferent behavior as a function of $Fe_{50}Mn_{50}$ thickness. Below 3 ML $Fe_{50}Mn_{50}$, the FeNi magnetization is aligned parallel with the Co magnetization direction. The ferromagnetic phase of $Fe_{50}Mn_{50}$ within this thickness range leads to a direct exchange coupling between the Co and FeNi layers. Between 3 and 6 ML $Fe_{50}Mn_{50}$ thickness, the magnetic coupling between the top FeNi layer and bottom Co layer is non-collinear. In this region $Fe_{50}Mn_{50}$ is presumably paramagnetic at room temperature. An oscillatory magnetic interlayer cou-pling between the FeNi and Co layers as a function of $Fe_{50}Mn_{50}$ thickness with a period of 2 ML has been observed for $Fe_{50}Mn_{50}$ thicknesses above 6 ML, where the $Fe_{50}Mn_{50}$ is antiferromagnetically ordered. Element selective XMCD-PEEM magnetic domain images

of the FeNi layer on top of a crossed double wedge of $Fe_{50}Mn_{50}$ and Co reveal in this thickness region a "saw-tooth" like periodic modulation of the coupling phase as a function of Co bottom layer thickness with 1 ML Co period and 0.3 ML $Fe_{50}Mn_{50}$ amplitude. MOKE measurements on $Co/Fe_{50}Mn_{50}/Co$ trilayers on Cu(001) indicate a decrease of the antiferromagnetic coupling strength by nearly 50% as the surface filling of the Co bottom layer is varied within submonolayer range, from a full to a half filled layer. The influence of interface roughness on the phase of the coupling is qualitatively explained in a "filling model" where part of the AFM deposited material does not contribute to the interlayer coupling. An interface alloying and frustration of the magnetic coupling at the step edges may be involved and play a key role.

- The interlayer magnetic coupling between Co with an in-plane magnetization and 15 ML Ni with an out-of-plane magnetization was addressed on $Ni/Fe_{50}Mn_{50}/Co$ trilayers on Cu(001). Below 3 ML $Fe_{50}Mn_{50}$ thickness the Ni magnetization is in-plane, oriented parallel with the Co magnetization. An out-of-plane oscillatory change of the Ni magnetization direction, with as a function of $Fe_{50}Mn_{50}$, was seen between 3 ML and 8 ML $Fe_{50}Mn_{50}$. Above 8 ML $Fe_{50}Mn_{50}$ faint stripes are superimposed onto small domains in the Ni layer, with magnetization pointing up or down. Deposition of 3 ML Co on top of the same sample leads in Ni to a spin-reorientation-transition to in-plane, with 2 ML $Fe_{50}Mn_{50}$ thickness oscillatory change of the magnetization direction of the top layer. A non-collinear spin structure of $Fe_{50}Mn_{50}$ may explain these observations. The out-of-plane spin component is reflected in the presence of the out-of-plane small domains in Ni top layer, while the in-plane spin component gives rise to 2 ML $Fe_{50}Mn_{50}$ thickness in plane oscillatory coupling as evidenced by the superimposed stripes.

- In $Ni/Fe_{50}Mn_{50}/Ni$ trilayers on Cu(001) small domains were seen in the top layer where the magnetization of the Ni bottom layer is in-plane oriented. The lateral dimension of these domains become smaller above 17 ML $Fe_{50}Mn_{50}$. Above 10 ML Ni bottom layer thickness, an oscillatory change of the out-of-plane magnetization direction of the top Ni layer as a function of $Fe_{50}Mn_{50}$ with two different periods was observed. Deposition of $Ni/Fe_{50}Mn_{50}$ on an annealed Ni bottom layer, leads to a periodic coupling between the Ni layers, with a period of 2 ML $Fe_{50}Mn_{50}$. Deposition of more than 0.5 ML Co on top of the same sample induces a spin-reorientation-transition of the Ni top layer magnetization to in-plane. Small domains are formed in the top layer above 12 ML $Fe_{50}Mn_{50}$. The presence of such small domains is associated with a statistically fluctuating in-plane component which can force the in-plane direction of magnetization of the top FM layer to a small domain configuration. A three-dimensional spin structure in the $Fe_{50}Mn_{50}$ layer has consequently to be considered.

- Study of ferromagnetically coupled FeNi and Co layers across Cu as a nonmagnetic spacer

layer revealed that the magnetization reversal process of the soft FeNi layer is influenced by the domain structure of the Co layer. Application of an external magnetic field of 340 Oe as a short pulse in opposite directions gives evidence of residual small domains located along the Co domain walls which do not switch their direction of magnetization. The regions in the FeNi that are either harder to switch or turn back to their original magnetization direction after the end of the field pulse are located in the vicinity of the domain walls of the Co layer. In the vicinity of the Co domain walls the stray field adds to the ferromagnetic coupling between Co and FeNi layers and the external magnetic field must not only "break" the interlayer coupling but also overcome the domain wall stray field.

The domain wall stray field mediated coupling was investigated in a second experiment for Co/Cu/Ni trilayers, where Ni layers have an EA oriented out-of-plane whereas the Co magnetization is in the film plane. Comparison of the as-grown layer-resolved magnetic domain images of the Co and Ni layers shows the influence of magnetostatic stray fields from Ni domain walls on the Co domain pattern. The effect is quantified by comparing to the effect of external magnetic fields, and is found to be equivalent to about 250 Oe.

Zusammenfassung

In der vorliegenden Arbeit wurde die magnetische Kopplung zwischen zwei epitaktisch auf Cu(001) aufgewachsenen und durch eine antiferromagnetische (AFM) oder nichtmagnetische Zwischenschicht getrennten ferromagnetischen (FM)-Schichten untersucht. Als FM Schichten dienten Co und FeNi, deren leichte Magnetisierungsachsen in der Schichtebene liegen sowie Ni mit einer leichten Magnetisierungsachse senkrecht zur Schichtebene. Als AFM Schicht wurde $Fe_{50}Mn_{50}$ und als nichtmagnetische Zwischenschicht Cu gewählt. Das lagenweise Wachstum wurde durch das Auftreten von MEED/RHEED-Oszillationen während des Schichtwachstums nachgewiesen. Insbesondere wurde mittels Rastertunnelmikroskopie (STM) die Oberflächenmorphologie von $Fe_{50}Mn_{50}$ untersucht. Die magnetischen Eigenschaften wurden mit magneto-optischem Kerr-Effekt und durch Abbildung magnetischer Domänen mit Hilfe eines Photoelektronen-Emissionsmikroskops (PEEM) unter Ausnutzung des zirkularen magnetischen Dichroismus als Kontrastmechanismus untersucht. Die folgenden Hauptergebnisse wurden erhalten:

Das Auftreten von RHEED-Oszillationen während des Aufdampfens von $Fe_{50}Mn_{50}$ auf Cu(001) deutet auf ein epitaktisches lagenweises Wachstum hin. STM-Aufnahmen zeigen große und flache Terrassen mit sehr kleinen (≈ 5 nm) Löchern von einatomarer Tiefe. Darüber hinaus konnte eine Feinstruktur mit einer scheinbaren Korrugationshöhe von etwa 0.5 Åfestgestellt werden. Rastertunnelspektroskopiemessungen (STS) belegen den spektroskopischen Ursprung dieser Korrugation. Das Auftreten dieser Feinstruktur könnte mit lokalen Konzentrationsunterschieden der Bestandteile der chemisch ungeordneten $Fe_{50}Mn_{50}$-Legierung zusammenhängen.

Die magnetische Zwischenschichtkopplung in FeNi/$Fe_{50}Mn_{50}$/Co Dreifachlagen auf Cu(001) ändert sich in Abhängigkeit von der $Fe_{50}Mn_{50}$ Schichtdicke. Unterhalb von 3 ML $Fe_{50}Mn_{50}$ ist die FeNi-Magnetisierung parallel zur Co-Magnetisierung ausgerichtet. Die in diesem Schichtdickenbereich ferromagnetische Phase von $Fe_{50}Mn_{50}$ führt zu einer direkten Austauschkopplung zwischen der Co- und der FeNi-Schicht. Im Schichdickenbereich von 3 bis 6 ML $Fe_{50}Mn_{50}$ ist die magnetische Kopplung zwischen der oberen FeNi-Schicht und der unteren Co-Schicht nichtkollinear. In diesem Bereich ist $Fe_{50}Mn_{50}$ vermutlich paramagnetisch bei Raumtemperatur. Eine oszillierende magnetische Zwischenschichtkopplung zwischen der FeNi- und der Co-Schicht als Funktion der $Fe_{50}Mn_{50}$-Schichtdicke mit einer Periode von 2 ML wurde für $Fe_{50}Mn_{50}$-

Schichtdicken oberhalb von 6 ML beobachtet, wo $Fe_{50}Mn_{50}$ antiferromagnetisch geordnet ist. Elementselektive XMCD-PEEM-Aufnahmen der magnetischen Domänen der FeNi-Schicht auf einer gekreuzten Doppelkeilstruktur aus $Fe_{50}Mn_{50}$ und Co zeigen in diesem Schichtdickenbereich eine periodische sägezahnartige Modulation der Kopplungsphase als Funktion der Co-Schicht mit einer Periode von 1 ML Co und einer Amplitude von 0.3 ML $Fe_{50}Mn_{50}$. MOKE-Messungen an $Co/Fe_{50}Mn_{50}/Co$-Dreischichtsystemen auf Cu(001) zeigen eine Abschwächung der antiferromagnetischen Kopplungstärke um fast 50%, wenn die Oberflächenfüllung der unteren Co-Schicht um weniger als eine Monolage, und zwar zwischen gefüllt und halbgefüllt variiert wird. Der Einfluss der Grenzflachenrauhigkeit auf die Phase der Kopplung wird qualitativ durch ein "Schichtauffüllungs-Model" erklärt, in dem ein Teil des deponierten AFM-Materials nicht zur Zwischenschichtkopplung beiträgt. Dies könnte mit Legierungsbildung an der Grenzschicht und Frustration der magnetischen Kopplung an Stufenkanten zusammenhängen.

Die Zwischenschichtkopplung zwischen Co mit einer leichten Magnetisierungsachse in der Ebene und 15 ML Ni mit einer leichten Magnetisierungsachse senkrecht dazu wurde am $Ni/Fe_{50}Mn_{50}/Co$-Dreischichtsystem untersucht. Unterhalb von 3 ML $Fe_{50}Mn_{50}$-Schichtdicke ist die Ni-Magnetisierung in der Ebene parallel zur Co-Magnetisierung orientiert. Eine Oszillation der senkrechten Magnetisierung von Ni mit einer Periode von 2 ML $Fe_{50}Mn_{50}$wurde zwischen 3 ML und 8 ML $Fe_{50}Mn_{50}$ beobachtet. Oberhalb von 8 ML $Fe_{50}Mn_{50}$ sind sehr kleine Domänen zu erkennen, denen ein schwacher streifenartiger Kontrast überlagert ist. Die zusätzliche Deposition von 3 ML Co auf dieselbe Probe führt in Ni zu einem Spinreorientierungsübergang der Magnetisierung in die Filmebene. Eine nicht-kollineare Spinstruktur von $Fe_{50}Mn_{50}$ könnte diese Beobachtungen erklären. Die senkrechte Spinkomponente spiegelt sich im Auftreten von kleinen senkrechten Domänen in der obersten Ni Lage wieder während die parallele Spinkomponente zu einer Oszillation der magnetischen Kopplung mit einer Periode von 2 ML $Fe_{50}Mn_{50}$ führt.

Im Falle von Dreischichtsystemen bestehend aus $Ni/Fe_{50}Mn_{50}/Ni$ auf einem Cu(001)-Substrat wurden kleine Domänen in der obersten Lage beobachtet. Die Magnetisierung der unteren Ni-Schicht ist hierbei in der Schichtebene und die Ausdehnung dieser Domänen nimmt ab wenn die Schichtdicken von $Fe_{50}Mn_{50}$ 17 ML überschreiten. Ist die Schichtdicke der unteren Ni-Lage grösser als 10 ML, ändert sich die senkrecht zur Schichtebene Magnetisierung der oberen Ni-Lage periodisch in Abhängigkeit der $Fe_{50}Mn_{50}$-Schichtdicke. Hierbei wurden grundsätzlich zwei verschiedene Perioden beobachtet. Beim Aufbringen von $Ni/Fe_{50}Mn_{50}$ auf eine angelassene Ni-Schicht findet man eine periodische Kopplung zwischen den beiden Ni-Schichten, wobei die Magnetisierung mit einer Periode von 2 ML $Fe_{50}Mn_{50}$ oszilliert. Bringt man zusätzlich mindestens 0.5 ML Co auf dieselbe Probe auf, so findet man einen Übergang der Magnetisierung der oberen Ni-Schicht hin zum in der Schichtebene Zustand. Kleine Domänen bilden sich in der oberen Schicht für $Fe_{50}Mn_{50}$ Schichtdicken gröals 12 ML. Das Auftreten von solchen kleinen Domänen ist auf statistische Fluktuationen der Komponente in der Ebene zurückzuführen, die die in der Schichtebene Magnetisierungsrichtung der oberen Schicht in eine

Konfiguration mit kleinen Domänen zwingt. Das bedeutet, dass bei der Diskussion der Daten eine drei-dimensionale Betrachtungsweise herangezogen werden muss.

Die Untersuchung von ferromagnetisch gekoppelten FeNi und Co Schichten für den Fall einer nichtmagnetischen Cu-Zwischenschicht zeigt eine Umkehr der Magnetisierung der magnetisch weichen FeNi Schicht, die durch die Struktur der Domänen der Co-Schicht beeinflusst wird. Bei Anlegen eines gepulsten externen magnetischen Felds mit einer Stärke von 340 Oe und entgegengesetzter Polarität beobachtet man kleine Domänen in der FeNi-Schicht entlang der Co-Domänenwände. Diese Domänen in der FeNi-Schicht können entweder ihre Magnetisierung nur schwer ändern oder kehren nach dem Abschalten das magnetischen Pulses in ihren ursprünglichen Zustand zurück. Diese befinden sich in der Nähe der Domänenwände der Co-Schicht. Das magnetische Streufeld an den Rändern der Co-Domänen führt zu einer zusätzlichen Kopplung zwischen den Co- und FeNi-Schichten, d.h. das externe Magnetfeld muss dann nicht nur die Kopplung zwischen den Schichten, sondern auch das Feld an den Domänen-Rändern überwinden.

Die Kopplung durch magnetostatische Streufelde von Domänenwänden wurde in einem zweiten Experiment an Co/Cu/Ni-Dreifachschichten weiter untersucht. Hier ist die Magnetisierung der Ni-Schichten senkrecht zur Schichtebene, die Orientierung beim Co liegt in der Schichtebene. Der Vergleich von lageaufgelösten "wie gewachsenen" Domänenbilder der Co- und Ni-Schicht zeigt einen magnetostatischen Einfluss der Ränder der Ni-Domänen auf die Co Domänen. Die Stärke dieses Effekts wurde durch den Vergleich mit den Resultaten bei Anlegen eines externen Magnetfeldes abgeschätzt. Hierbei erhält man bei einer Feldstärke von 250 Oe vergleichbare Ergebnisse.

Bibliography

[1] P. Grünberg, R. Schreiber, Y. Pang, M. B. Brodsky, H. Sowers, Phys. Rev. Lett. **57**, 2442 (1986).

[2] B. Heinrich, J. A. C. Bland, Ultrathin Magnetic Structures II, Springer-Verlag, Berlin 1994.

[3] S. S. P. Parkin, N. More, K. P. Roche, Phys. Rev. Lett. **64**, 2304 (1990).

[4] S. S. P. Parkin, Phys. Rev. Lett. **67**, 3598 (1991).

[5] M. N. Baibich, J. M. Broto, A. Fert, F. Nguyen Van Dau, F. Petroff, P. Eitenne, G. Creuzet, A. Friederich, J. Chazelas, Phys. Rev. Lett. **61**, 2472, (1988).

[6] H. A. Wierenga, W. de Jong, M. W. J. Prins, Th. Rasing, R. Vollmer, A. Kirilyuk, H. Schwabe, J. Kirschner, Phys. Rev. Lett. **74**, 1462 (1995).

[7] A. Schreyer, J. F. Ankner, Th. Zeidler, H. Zabel, M. Schäfer, J. A. Wolf, P. Grünberg, C. F. Majkrzak, Phys. Rev. B **52**, 16066 (1995).

[8] D. T. Pierce, J. Unguris, R. J. Celotta, M. D. Stiles, J. Magn. Magn. Mater. **200**, 290 (1999).

[9] H. Hopster, Phys. Rev. Lett. **83**, 1227 (1999).

[10] A. Berger, H. Hopster, Phys. Rev. Lett. **73**, 193 (1994).

[11] D. T. Pierce, A. D. Davies, J. A. Stroscio, D. A. Tulchinsky, J. Unguris, R. J. Celotta, J. Magn. Magn. Mater. **222**, 13 (2000).

[12] D. A. Tulchinsky, J. Unguris, R. J. Celotta, J. Magn. Magn. Mater. **212**, 91 (2000).

[13] J. C. Slonczewski, Phys. Rev. Lett. **67**, 3172 (1991).

[14] J. C. Slonczewski, J. Magn. Magn. Mater. **150**, 13 (1995).

[15] W. Kuch, F. Offi, L. I. Chelaru, M. Kotsugi, K. Fukumoto, J. Kirschner, Phys. Rev. B **65**, 140408 (R), (2002).

[16] H. Ohldag, A. Scholl, F. Nolting, S. Anders, F. U. Hillebrecht, J. Stöhr, Phys. Rev. Lett **86**, 2878 (2001).

[17] M. Freyss, D. Stoeffler, H. Dreysse, Phys. Rev. B **54**, 12667 (1996).

[18] A. Schreyer, C. F. Majkrzak, Th. Zeidler, T. Schmitte, P. Bödeker, K. Theis-Bröhl, A. Abromeit, J. A. Dura, T. Watanabe, Phys. Rev. Lett. **79**, 4914 (1997).

[19] P. Bödeker, A. Hucht, A. Schreyer, J. Borchers, F. Güthoff, H. Zabel, Phys. Rev. Lett. **81**, 914 (1998).

[20] J. Unguris, R. J. Celotta, D. T. Pierce, Phys. Rev. Lett. **69**, 1125 (1992).

[21] K. S. Moon, R. E. Fontana, Jr. , S. S. P. Parkin, Appl. Phys. Lett. **74**, 3690 (1999).

[22] L. Néel, Comp. Rend. Acad. Sci. France **255**, 1545 (1962).

[23] S. Gider, B. U. Runge, A. C. Marley, S. S. P. Parkin, Science, **281**, 797 (1998).

[24] L. Thomas, J. Lüning, A. Scholl, F. Nolting, S. Anders, J. Stöhr, S. S. P. Parkin, Phys. Rev. Lett. **84**, 3462 (2000).

[25] A. Schreyer, K. Bröhl, J. F. Ankner, C. F. Majkrzak, T. Zeidler, P. Bödeker, N. Metoki, H. Zabel, Phys. Rev. B **47**, 15334 (1993).

[26] W. Weber, C. H. Back, A. Bischof, Ch. Würsch, and R. Allenspach, Phys. Rev. Lett. **76**, 1940 (1996).

[27] C. Carbone, E. Vescovo, O. Rader, W. Gudat, W. Eberhardt, Phys. Rev. Lett. **71**, 2805, (1993).

[28] R. K. Kawakami, E. Rotenberg, Ernesto J. Escorcia–Aparicio, Hyuk J. Choi, T. R. Cummins, J. G. Tobin, N. V. Smith, Z. Q. Qiu, Phys. Rev. Lett. **80** 1754 (1998).

[29] M. Rührig, R. Schäfer, A. Hubert, R. Mosler, J. A. Wolf, S. Demokritov, P. Grünberg, Phys. Stat. Solidi A **125**, 635 (1991).

[30] D. M. Edwards, J. Mathon, R. B. Muniz, M. S. Phan, Phys. Rev. Lett. **67**, 493 (1991).

[31] Y. Wang, P. M. Levy, J. L. Fry, Phys. Rev. Lett. **65**, 2732 (1990).

[32] J. Barnas, J. Magn. Magn. Matter. **111**, L215 (1992).

[33] J. C. Slonczewski, J. Magn. Magn. Mater. **126**, 374 (1993).

[34] P. Bruno, J. Magn. Magn. Mater. **121**, 248 (1993).

[35] P. Bruno, Phys. Rev. B **52**, 411 (1995).

[36] M. D. Stiles, Phys. Rev. B **48**, 7238 (1993).

[37] P. Bruno, C. Chappert, Phys. Rev. Lett. **67**, 1602, (1991).

[38] E. E. Fullerton, K. T. Riggs, C. H. Sowers, S. D. Bader, A. Berger, Phys. Rev. Lett. **75**, 330 (1995).

[39] E. E. Fullerton, C. H. Sowers, S. D. Bader, Phys. Rev. B **56**, 5468 (1997).

[40] L. Néel, Comp. Rend. Acad. Sci. France **255**, 1676 (1962).

[41] L. Néel, Compt. Rend. Acad. Sci. France **241**, 533 (1955).

[42] J. C. Slonczewski, S. Middelhoek, Appl. Phys. Lett. **6**, 139 (1965).

[43] A. Hubert, R. Schäfer, Magnetic Domains, Springer-Verlag, Berlin, 1998.

[44] G. V. Spivak, T. N. Dombrovskaia, N. N. Sedov, Sov. Phys. Dokl. **2**, 429 (1957).

[45] P. Grütter, H. J. Mamin, D. Rugar, in Scanning Tunneling Microscopy, edited by R. Wiesendanger and H. -J. Güntherodt, Springer-Verlag, Berlin, vol. II, 1992.

[46] J. Stöhr, Y. Wu, B. D. Hermsmeier, M. G. Samant, G. R. Harp, S. Koranda, D. Dunham, B. P. Tonner, Science **259**, 658 (1993).

[47] M. Rührig, R. Schäfer, A. Hubert, R. Mosler, J. A. Wolf, S. Demokritov, P. Grünberg, Phys. Status Solidi (a) **125**, 635 (1991).

[48] G. Schütz, W. Wagner, W. Wilhelm, P. Kienle, R. Zeller, R. Frahm, G. Materlik, Phys. Rev. Lett. **58**, 737 (1987).

[49] C. T. Chen, Y. U. Idzerda, H. J. Lin, G. Meigs, A. Chaiken, G. A. Prinz, G. H. Ho, Phys. Rev. B **48**, 642 (1993).

[50] V. Chakarian, Y. U. Idzerda, G. Meigs, E. E. Chaban, J. H. Park, C. T. Chen, Appl. Phys. Lett. **66**, 3368 (1995).

[51] P. Fischer, T. Eimüller, G. Schütz, P. Guttmann, G. Schmahl, K. Pruegl, G. Bayreuther, J. Phys. D: Appl. Phys. **31**, 649 (1998).

[52] H. C. Siegmann, J. Phys. Condens. Matter. **4**, 8395 (1992).

[53] R. Nakajima, J. Stöhr, Y. U. Idzerda, Phys. Rev. B **59**, 6421 (1999).

[54] J. Stöhr, H. A. Padmore, S. Anders, T. Stammler, M. R. Scheinfein, Surf. Rev. Lett. **5**, 1297 (1998).

[55] B. T. Thole, P. Carra, F. Sette, G. van der Laan, Phys. Rev. Lett. **68**, 1943 (1992).

[56] P. Carra, B. P. Thole, M. Altarelli, X. Wang, Phys. Rev. Lett. **70**, 694 (1993).

[57] R. Wiesendanger, Scanning probe microscopy, Springer-Verlag, Berlin, 1998.

[58] W. Wulfhekel, J. Kirschner, Appl. Phys. Lett. **75**, 1944 (1999).

[59] G. F. Rempfer, O. H. Griffith, Ultramicroscopy **27**, 273 (1989).

[60] R. Imbihl, G. Ertl, Chem. Rev. **95**, 697 (1995).

[61] B. P. Tonner, G. R. Harp, Rev. Sci. Instrum. **59**, 853 (1988).

[62] C. M. Schneider, J. Magn. Magn. Mater. **175**, 160 (1997).

[63] Focus IS–PEEM, Omicron.

[64] W. Braun, Applied RHEED: Reflection–High–Energy Electron Diffraction During Crystal Growth, Springer-Verlag, Berlin, 1999.

[65] C. S. Lent, P. I. Cohen, Surf. Sci. **139**, 121 (1984).

[66] P. I. Cohen, P. R. Pukite, J. M. van Hove, C. S. Lent, J. Vac. Sci. Technol. A **4**, 176 (1986).

[67] D. Briggs, M. P. Seah, Practical surface analysis, Second Edition, vol. I, Wiley, Chichester, 1990.

[68] Z. Q. Qiu, S. D. Bader, Rev. Sci. Instrum. **71**, 1243 (2000).

[69] UHV–SPM, Omicron.

[70] W. Kuch, J. Gilles, F. Offi, S. S. Kang, S. Imada, S. Suga, J. Kirschner, J. Electron. Spectrosc. Relat. Phenom. **109**, 249 (2000).

[71] B. Heinrich, J. F. Cochran, T. Monchesky, R. Urban, Phys. Rev. B **59**, 14520 (1999).

[72] B. Dieny, V. S. Speriosu, S. S. P. Parkin, B. A. Gurney, D. R. Wilhoit, D. Mauri, Phys. Rev. B **43**, 1297 (1999).

[73] C. J. Smithells, Smithells Metals Reference Book, Seventh Edition, edited by E. A. Brandes and G. B. Brook, Butterworth, London, 1992.

[74] Y. Endoh, Y. Ishikawa, J. Phys. Soc. Jpn. **30**, 1614 (1971).

[75] Y. W. Mo, F. J. Himpsel, Phys. Rev. B **50**, 7868 (1994).

[76] A. K. Schmid, J. Kirschner, Ultramicroscopy, **42-44**, 483 (1992).

[77] O. Fruchart, M. Klaua, J. Barthel, J. Kirschner, Appl. Surf. Sci. **162–163**, 529 (2000).

[78] Francesco Offi, Dissertation, Marthin Luther–Universität Halle-Wittenberg (2002), published: http: //sundoc. bibliothek. uni-halle. de/diss-online/02/02H126/index. htm. .

[79] G. Ehrlich and F. G. Hudda, J. Chem. Phys. **44**, 1039 (1966).

[80] R. L. Schwoebel, E. J. Shipsey, J. Appl. Phys. **37**, 3682 (1966).

[81] F. Offi, W. Kuch, L. I. Chelaru, K. Fukumoto, M. Kotsugi, J. Kirschner, Phys. Rev. B **67**, 094419 (2003).

[82] F. Offi, W. Kuch, J. Kirschner, Phys. Rev. B **66**, 064419 (2002).

[83] H. D. Chopra, D. X. Yang, P. J. Chen, H. J. Brown, L. J. Swartzendruber, W. F. Egelhoff, Jr. , Phys. Rev. B **61**, 15312 (2000).

[84] G. J. Strijkers, J. T. Kohlhepp, H. J. M. Swagten, W. J. M. de Jonge, Phys. Rev. Lett. **84**, 1812 (2000).

[85] P. Krams, F. Lauks, R. L. Stamps, B. Hillebrands, G. Güntherodt, Phys. Rev. Lett. **69**, 3674 (1992).

[86] J. R. Cerda, P. L. de Andres, A. Cebollada, R. Miranda, E. Navas, P. Schuster, C. M. Schneider, J. Kirschner, J. Phys. : Condens. Matter. **5**, 2055 (1993).

[87] Z. Q. Qiu, J. Pearson, S. D. Bader, Phys. Rev. B **46**, 8659 (1992).

[88] S. T. Purcell, M. T. Johnson, N. E. McGee, R. Coehoorn, W. Hoving, Phys. Rev. B **45**, 13064 (1992).

[89] M. Kowalewski, C. M. Schneider, B. Heinrich, Phys. Rev. B **47**, 8748 (1993).

[90] M. Farle, B. Mirwald–Schulz, A. N. Anisimov, W. Platow, K. Baberschke, Phys. Rev. B **55**, 3708 (1997).

[91] R. Vollmer, Th. Gutjahr–Löser, J. Kirschner, S. van Dijken, B. Poelsema, Phys. Rev. B **60**, 6277 (1999).

[92] W. Kuch, X. Gao, J. Kirschner, Phys. Rev. B **65**, 64406 (2002).

[93] W. Kuch, J. Gilles, S. S. Kang, S. Imada, S. Suga, J. Kirschner, Phys. Rev. B **62**, 3824 (2000).

[94] J. Shen, J. Giergiel, J. Kirschner, Phys. Rev. B **52**, 8454 (1995).

[95] J. Shen, M. T. Lin, J. Giergiel, C. Schmidthals, M. Zharnikov, C. M. Schneider, J. Kirschner, J. Magn. Magn. Mater. **156**, 104 (1996).

[96] S. S. P. Parkin, K. P. Roche, M. G. Samant, P. M. Rice, R. B. Beyers, R. E. Scheuerlein, E. J. O'Sullivan, S. L. Brown, J. Bucchigano, D. W. Abraham, Yu Lu, M. Rooks, P. L. Trouilloud, R. A. Wanner, W. J. Gallagher, J. Appl. Phys. **85**, 5828 (1999).

[97] M. Klaua, D. Ullmann, J. Barthel, W. Wulfhekel, J. Kirschner, R. Urban, T. L. Monchesky, A. Enders, J. F. Cochran, B. Heinrich, Phys. Rev. B **64**, 134411 (2001).

[98] M. Hehn, O. Lenoble, D. Lacour, C. Féry, M. Piécuch, Phys. Rev. B **61**, 11643 (2000).

[99] S. Gider, B. -U. Runge, A. C. Marley, S. S. P. Parkin, Science, **281**, 797 (1999).

[100] R. Schäfer, R. Urban, D. Ullmann, H. L. Meyerheim, B. Heinrich, L. Schultz, J. Kirschner, Phys. Rev. B, **65**, 144405 (2002).

[101] W. Weber, R. Allenspach, A. Bischof, Appl. Phys. Lett. **70**, 520 (1997).

[102] J. Fassbender, U. May, B. Schirmer, R. M. Jungblut, B. Hillebrands, G. Güntherodt, Phys. Rev. Lett. **75**, 4476 (1995).

[103] B. Heinrich, J. F. Cochran, D. Venus, K. Totland, C. M. Schneider, K. Myrtle, J. Magn. Magn. Mat. **156**, 215 (1996).

[104] A. Davies, J. A. Stroscio, D. T. Pierce, R. J. Celotta, Phys. Rev. Lett. **76**, 4175 (1996).

[105] M. Freyss, D. Stoeffler, H. Dreyssé, Phys. Rev. B **56**, 6047 (1997).

[106] E. Bauer, Z. Kristallogr. **110**, 372 (1958).

[107] J. Shen, J. Giergiel, A. K. Schmid, J. Kirschner, Surf. Sci. **328**, 32 (1995).

[108] A. K. Schmid, D. Atlan, H. Itoh, B. Heinrich, T. Ichinokawa, J. Kirschner, Phys. Rev. B(R) **48**, 2855, (1993).

[109] H. Brune, K. Bromann, H. Röder, K. Kern, Phys. Rev. B(R) **52** 14380 (1995).

[110] T. K. Yamada, M. M. J. Bischoff, T. Mizoguchi, H. van Kempen, Surf. Sci. **516**, 179 (2002).

[111] Y. J. Choi, I. C. Jeong, J. -Y. Park, S. -J. Kang, J. Lee, Y. Kuk, Phys. Rev. B **59**, 10918 (1999).

[112] T. Flores, S. Junghans, M. Wuttig, Surf. Sci. **371**, 14 (1997).

[113] O. Rader, W. Gudat, D. Schmitz, C. Carbone, W. Eberhardt, Phys. Rev. B **56**, 5053 (1997).

[114] V. S. Stepanyuk, R. Zeller, P. H. Dederichs, I. Mertig, Phys. Rev. B **49**, 5157 (1994).

[115] B. Heinrich, M. From, J. F. Cochran, L. X. Liao, Z. Celinski, C. M. Schneider, K. Myrtle, Mat. Res. Soc. Symp. Proc. **313**, 119, 1993.

[116] S. S. Yan, R. Schreiber, F. Voges, C. Osthöver, P. Grünberg, Phys. Rev. B **59**, 11641, 1999.

[117] J. Unguris, R. J. Celotta, D. T. Pierce, Phys. Lett. **67**, 140 (1991).

[118] J. Unguris, R. J. Celotta, D. T. Pierce, Phys. Lett. **79**, 2734 (1997).

[119] G. A. T. Allan, Phys. Rev. B **1**, 352 (1970).

[120] C. M. Schneider, P. Bressler, P. Schuster, J. Kirschner, J. J. de Miguel, R. Miranda, Phys. Rev. Lett. **64**, 1059 (1990).

[121] Y. Li, K. Baberschke, Phys. Rev. Lett. **68**, 1208 (1992).

[122] R. Vollmer, S. van Dijken, M. Schleberger, J. Kirschner, Phys. Rev. B **61**, 1303 (2000).

[123] F. Wilhelm, U. Bovensiepen, A. Scherz, P. Poulopoulos, A. Ney, H. Wende, G. Ceballos, K. Baberscke, J. Magn. Magn. Mat. **222**, 163 (2000).

[124] O. Rader, E. Vescovo, J. Redinger, S. Blügel, C. Carbone, W. Eberhardt, W. Gudat, Phys. Rev. Lett. **72**, 2247 (1994).

[125] A. Scherz, H. Wende, P. Poulopoulos, J. Lindner, K. Baberschke, P. Blomquist, R. Wäppling, F. Wilhelm, N. B. Brookes, Phys. Rev. B **64**, R 180407 (2001).

[126] F. Wilhelm, P. Srivastava, A. Ney, N. Haack, G. Ceballos, M. Farle, K. Baberschke, J. Magn. Magn. Mat. **198–199**, 458 (1999).

[127] F. Wilhelm, Dissertation, Freie Universität Berlin (2000).

[128] P. J. Jensen, K. H. Bennemann, P. Polopoulos, M. Farle, F. Wilhelm, K. Baberschke, Phys. Rev. B **60**, 14994 (1999).

[129] S. S. P. Parkin, V. S. Speriosu, in Magnetic Properties Of Low-Dimensional Systems II, Springer-Verlag, Berlin 1990.

[130] P. J. van der Zaag, Y. Ijiri, J. A. Borchers, L. F. Feiner, R. M. Wolf, J. M. Gaines, R. W. Erwin, M. A. Verheijen, Phys. Rev. Lett. **84**, 6102 (2000).

[131] T. Schmitte, A. Schreyer, V. Leiner, R. Siebrecht, K. Theis–Bröhl, H. Zabel, Europhys. Lett. **48**, 692 (1999).

[132] J. S. Kouvel, J. S. Kasper, J. Phys. Chem. Solids **24**, 529 (1963).

[133] H. Umebayashi, Y. Ishikawa, J. Phys. Soc. Jpn. **21**, 1281 (1966).

[134] D. Spišák , J. Hafner, Phys. Rev. B **61**, 11569 (2000).

[135] T. C. Schulthess, W. H. Butler, G. M. Stocks, S. Maat, G. J. Mankey, J. Appl. Phys. **85**, 4842 (1999).

[136] A. Thiaville, J. Miltat, J. -M. Garca, in : Magnetic Microscopy of Nanostructures, edited by H. Hopster and H. P. Oepen, Springer, Berlin, to appear.

[137] W. Kuch, L. I. Chelaru, K. Fukumoto, F. Porrati, F. Offi, M. Kotsugi, J. Kirschner, to be published.

[138] W. Kuch, Xingyu Gao, J. Gilles, J. Kirschner, J. Magn. Magn. Mater. **242–245**, 1246 (2002).

[139] M. Speckmann, H. P. Oepen, H. Ibach, Phys. Rev. Lett. **75**, 2035 (1995).

[140] K. Fukumoto, H. Daimon, L. I. Chelaru, F. Offi, W. Kuch, J. Kirschner, Surf. Sci. **514**, 151 (2002).

[141] H. P. Oepen, J. Magn. Magn. Mater. **93**, 116 (1991).

Appendix A

Curriculum vitae

Personal data:

Name:	Liviu Ionut Chelaru
Date of birth:	May 15, 1974
Place of birth:	Iasi, Romania
Marital status:	unmarried

Education:

Sept. 1980 – June 1984	Primary school "M. Kogalniceanu", Iasi, Romania.
Sept. 1984 – June 1988	Secondary school at "C. Negruzzi", Iasi, Romania.
Sept. 1988 – July 1992	High school at "C. Negruzzi", Iasi, Romania.
Oct. 1992 – July 1997	Faculty of Physics, "Al. I. Cuza" University, Iasi, Romania. Diploma Physics: "Magnetometer study of the magnetic properties of thin films"
Oct. 1997 – March 1999	Master of Science, Faculty of Physics, "Al. I. Cuza" University, Iasi, Romania. Specialization field: Phyiscs of thin solid films. Master thesis: "Study of the magnetic properties of amorphous FeSm alloys thin films"
Since April 2000	Ph.D. candidate at Max–Planck–Institut für Mikrostrukturphysik, Halle, Germany. Supervisor: Prof. Dr. Jürgen Kirschner

Halle, April 22, 2003   Liviu Ionut Chelaru

Appendix B

Erklärung

Ich versichere hiermit, die vorliegende Dissertation

Microscopic studies of interlayer magnetic coupling across nonmagnetic and antiferromagnetic spacer layers

selbständig verfasst und keine anderen als die von mir angegebenen Quellen und Hilfsmittel verwendet zu haben. Die den benutzten Werken wörtlich oder inhaltlich entnommennen Stellen sind als solche kenntlich gemacht.

Halle, April 22, 2003   Liviu Ionut Chelaru

Appendix C

Acknowledgments

I will always be deeply indebted to Professor Gheorghe Singurel for offering me the possibility and opportunity of coming into contact with German scientific community.

Finally, I express my thanks to my parents and my brother, for their continuous love and support throughout all the years of my Ph.D. studies.